



University
of Glasgow

Skuce, Rebecca L. (2015) *Bacteria - mineral - nanoparticle interactions in water and wastewater*. PhD thesis.

<http://theses.gla.ac.uk/6153/>

Copyright and moral rights for this thesis are retained by the author

A copy can be downloaded for personal non-commercial research or study, without prior permission or charge

This thesis cannot be reproduced or quoted extensively from without first obtaining permission in writing from the Author

The content must not be changed in any way or sold commercially in any format or medium without the formal permission of the Author

When referring to this work, full bibliographic details including the author, title, awarding institution and date of the thesis must be given

Bacteria – mineral – nanoparticle interactions in water and wastewater

Rebecca L. Skuce

BSc (Hons) University of Glasgow

Submitted in fulfilment of the requirements for the Degree of Doctor of Philosophy

School of Geographical and Earth Sciences

College of Science and Engineering

University of Glasgow

February 2015

© Rebecca L. Skuce, 2015

Dedication

I dedicate this thesis to the loving memory of my Grandfather George Donaldson Crooke.

Abstract

With a rising demand for nanomaterials and their continual increase in production, the release of nanoparticles (NPs) into the environment is inevitable (Petosa et al., 2010). Problematically, NPs can have a wide range of toxic effects, which are exacerbated by their size (at least one dimension smaller than 100 nm)(Engineering., 2004). Detrimental effects include brain, intestinal and respiratory injury, delayed embryonic development, DNA damage which ultimately lead to increased mortality (Trouiller et al., 2009), (Handy et al., 2008). Natural and manufactured NPs also have the ability to bind and transport chemical pollutants, thus enhancing their toxicity (Moore, 2006).

While an array of techniques are available for *in situ* remediation of numerous groundwater contaminants, there are currently none for *in situ* remediation of nanoparticles. This fundamental technology gap means we are poorly prepared to deal with nanoparticle pollution events. The aim of this PhD was to develop mechanisms to immobilise and remove nanoparticles from water and waste water in order to prevent the transport of nanoparticles to sites where they have the potential to cause harm.

Experiments conducted demonstrate the potential of microbially mediated mineral formation to immobilise nanoparticles from water. The ureolytic bacteria *Sporosarcina pasteurii* was used to induce calcium carbonate precipitation in batch and column experiments. Nanoparticle immobilisation was tested as a function of nanoparticle size and surface charge. The results demonstrate the successful immobilisation of negatively charged nanoparticles (both large and small, 150 and 35 nm respectively), while failing to remove positively charged nanoparticles from solution. In order to capture positively charged nanoparticles a second mineral, struvite, was tested. The precipitation of struvite successfully immobilised positively charged nanoparticles. However, in comparison to the calcite precipitation experiments the removal of positively charged nanoparticles was found to be pH and ionic strength dependant. Finally, the ability of *Bacillus subtilis*, a common groundwater bacterium and wastewater treatment biofilm to adsorb and remove nanoparticles from solution was examined. Here both biosorbent materials were highly efficient at removing positively charged nanoparticles from solution whilst negatively charged nanoparticles remained in suspension.

The research presented here demonstrates that microbially induced mineral precipitation may be used as a tool to immobilise nanoparticles from contaminated groundwater. In addition, bacteria and wastewater treatment biofilm were found to be highly efficient biosorbents of positively charged nanoparticles. These findings hold implications for the fate and transport of nanoparticles through environmental systems and wastewater treatment plants.

Table of Contents

List of tables	8
List of Figures	9
Acknowledgement	11
Author's declaration	12
List of parameters	13
Acronyms	15
1 Introduction.....	16
1.1 Nanoparticles	16
1.1.1 Natural and anthropogenic nanoparticle toxicity.....	17
1.1.2 Manufactured nanoparticles	18
1.1.3 Manufactured nanoparticle toxicology	21
1.1.4 Physiochemical properties of Nanoparticles.....	23
1.1.5 Nanoparticles used in remediation.....	27
1.1.6 Environmental exposure to nanoparticles	28
1.2 Bacteria	30
1.2.1 Biofilm.....	31
1.2.2 Biofilm - nanoparticle interactions	31
1.3 Microbially mediated mineral formation	32
1.3.1 General microbial mineral formation.....	32
1.3.2 Ureolytically-driven calcium carbonate precipitation	33
1.3.3 Ureolytically-driven calcium carbonate precipitation technologies	33
1.4 Research objectives	34
2 Immobilisation of nanoparticles by microbially mediated calcite precipitation	36
2.1 Summary	36
2.2 Introduction	36
2.3 Materials and methods.....	39
2.3.1 Nanoparticles.....	39
2.3.2 Experimental design.....	40
2.3.3 Chemical analysis.....	40
2.3.4 Transmission Electron Microscopy (TEM)	41
2.3.5 Kinetic analysis and calcite precipitation.....	42
2.4 Results	43
2.4.1 Immobilisation of small negatively charged nanoparticles(s-negNP)	43
2.4.2 Immobilisation of small positively charged nanoparticles (s-posNP)	48
2.4.3 Immobilisation of large negatively charged nanoparticles	49

2.5	Mineral analysis by Transmission Electron Microscopy (TEM)	50
2.6	Discussion	54
2.7	Conclusion	65
3	Immobilisation of nanoparticles through porous media by calcium carbonate precipitation	66
3.1	Summary	66
3.2	Introduction	66
3.3	Materials and methods.....	67
3.3.1	and porous media.....	67
3.3.2	Nanoparticle transport experiments	68
3.3.3	Nanoparticle immobilisation experiments	69
3.4	Results	70
3.4.1	Nanoparticle transport experiments.....	70
3.5	Discussion	79
3.6	Conclusion	86
4	Immobilisation of nanoparticles by bacterially precipitated struvite	88
4.1	Introduction	88
4.2	Materials and methods.....	90
4.2.1	Nanoparticles.....	90
4.2.2	Struvite precipitation experiments	90
4.2.3	Nanoparticle capture by struvite precipitation	91
4.2.4	Nanoparticle removal by pre-formed struvite.....	92
4.2.5	Chemical analysis.....	93
4.2.6	Zeta potential analysis.....	93
4.2.7	Scanning Electron and Raman Microscopy	93
4.3	Results	94
4.3.1	Struvite precipitation experiments	94
4.3.2	Nanoparticle capture by struvite.....	97
4.3.3	Nanoparticle removal by pre-formed struvite crystals.....	105
4.3.4	Zeta potential of struvite	106
4.4	Discussion	107
4.5	Conclusion	117
5	Bacterial biosorption of nanoparticles	118
5.1	Summary	118
5.2	Introduction	118
5.3	Materials and Methods	120
5.3.1	Nanoparticles.....	120
5.3.2	<i>Bacillus subtilis</i> adsorption experiments.....	120
5.3.3	Wastewater biofilm adsorption experiments	121

5.3.4	Chemical analysis.....	123
5.3.5	Transmission Electron Microscopy (TEM)	123
5.4	Results	124
5.4.1	<i>Bacillus subtilis</i> adsorption experiments.....	124
5.4.2	Wastewater biofilm sorption experiments	127
5.4.3	Transmission Electron Microscopy (TEM)	129
5.4.4	Discussion	132
5.4.5	Conclusion	138
6	Conclusion.....	139
6.1	Summary	139
6.2	Immobilisation of nanoparticles by mineral precipitating systems	139
6.3	Immobilisation of nanoparticles through porous media by calcium carbonate precipitation.....	142
6.4	Bacterial biosorption of nanoparticles	142
6.5	Future work	143
	Appendix A	146
	Appendix B	147
	List of references.....	148

List of tables

Table 2.1: Characteristics of NPs used in this study.	39
Table 2.2: Summary of kinetic parameters.	55
Table 2.3: Summary of the parameters for used in DLVO equations	58
Table 3.1: Total recovery of NH_4^+ , Ca^{2+} and NPs as calculated from the area under the recovery curve.	79
Table 4.1: Summary of tested experimental conditions.	92
Table 4.2 Summary of the experimental parameters for each $\text{Mg}^{2+}/\text{PO}_4^{3-}$ addition	114
Table 5.1: Summary of tested experimental conditions.	124

List of Figures

Figure 1.1: Diagram of a single-wall carbon nanotube (Allotropes, 2013).	19
Figure 1.2: Silver - gold core - shell NPs (Yee, 2007).	19
Figure 1.3: A selection of current nano-containing products currently on the market (Chatterjee, 2008).	20
Figure 1.4: This graph displays the inverse relationship between particle size and the percent of surface molecules (Nel et al., 2006).	22
Figure 1.5: Schematic representation of the electronic double layer.	25
Figure 1.6: Total (net) interaction energy curve produced combination of the van der Waals attraction from the electrostatic repulsion curve.	26
Figure 1.7: A typical zeta potential vs pH plot (Silver-Colloids, 2012).	27
Figure 1.8: Routes of exposure and transformations of NPs in the environment (Simonet and Valcárcel, 2009).	30
Figure 2.1: Time series showing changes in NH_4^+	45
Figure 2.2: Time series showing changes in pH for the for the (a) s-negNP, (b) s-posNP and (c) l-negNP. Each data point represents the average of triplicate experiments with associated standard deviation ($\sigma = 1$, shown as error bars)... ..	46
Figure 2.3: Time series showing changes in dissolved Ca^{2+} and NP concentration for nanoparticle immobilization (NP-I) experiments:	47
Figure 2.4: Time series showing changes in Fe (NP) concentration for the (a) biotic and (b) abiotic control for all NP types tested.	48
Figure 2.5: Percentage of precipitated Ca^{2+} compared to % NP captured from solution for s-neg and s-posNPs.	49
Figure 2.6: Time series showing Fe (NP) concentration during the double dose experiment for the l-negNP.	50
Figure 2.7: Photographs of glass slides placed at the bottom of the microcosms	52
Figure 2.8: SEM and TEM images of captured NPs.	53
Figure 2.9: (a) STEM image of an area of calcite crystal containing a cluster of NPs (black dots).	54
Figure 2.10: Interaction energy profile which displays the attractive force which exists between the s-negNP and the positive calcite surface.....	60
Figure 2.11: Interaction energy profiles for the attachment of s-posNPs to positively charged calcite surfaces.	61
Figure 2.12: Interaction energy profiles for the attachment of l-negNPs to positively charged calcite surfaces.	62
Figure 3.1: Schematic drawing of the experimental set-up for column experiments.	69
Figure 3.2: Transport of NPs suspended in SDW (diamonds) and 50 mM CaCl_2 (squares) through:.....	71
Figure 3.3: Breakthrough curves for the transport of NH_4^+ through the (a) fine, (b) medium and (c) coarse grained glass beads.	74
Figure 3.4: Breakthrough curves for the transport of Ca^{2+} through the (a) fine, (b) medium and (c) coarse grained glass beads.	75
Figure 3.5: Breakthrough curves for the transport of (NPs) through the (a) fine, (b) medium and (c) coarse grained glass beads.	76
Figure 3.6: Breakthrough curves for the transport of (a) NH_4^+ , (b) Ca^{2+} and (c) NPs sand packed columns.	78
Figure 3.7: Scanning electron microscope images of porous media.	82
Figure 3.8: Simplified sketch detailing the immobilisation of NPs within porous media.....	84

4.1: Time series showing changes in pH, NH_4^+ , Mg^{2+} , PO_4^{3-} concentration for the S1 experiment.....	95
Figure 4.2: Time series showing changes in pH, NH_4^+ , PO_4^{3-} and Mg^{2+} concentration for experiment S2.....	96
4.3: Photo graph of struvite precipitated in the absence of NPs (experiment S2).	97
Figure: 4.4: Time series showing changes in pH, NH_4^+ , Mg^{2+} , PO_4^{3-} and Fe (NP) concentration (%) for experiment N1.....	98
4.5: Photographs of struvite and magnesium phosphate precipitates.	102
Figure 4.6: Time series showing changes in pH, NH_4^+ , Mg^{2+} , PO_4^{3-} and Fe (NP) concentration.	103
Figure 4.7: Scanning Electron Microscope (SEM) image illustrating.....	104
Figure 4.8: Raman spectra of struvite and magnesium phosphate minerals.	105
Figure 4.9: Percentage of Fe (NPs) electrostatically attached to struvite mineral surfaces when suspended in increasing concentrations of KCl.	106
Figure 4.10: Zeta potential of struvite crystals measured as a function of pH and KCl concentration.	107
Figure 4.11: Saturation index values for $\text{Mg}_3(\text{PO}_4)_2$, $\text{MgHPO}_4 \cdot 3\text{H}_2\text{O}$ and struvite.	109
Figure 4.12 Interaction energy profiles calculated for the positively charged NPs and the negatively charged struvite surfaces (using a Hamaker constant for struvite of 1.54×10^{-20}). Note (b) is an enlargement of graph (a).	115
Figure 4.13: Total interaction energy profile for positively charged NPs interacting with struvite surfaces as a function of increasing KCl concentrations from 87.5 to 200 M/m^3	116
Figure 5.1: Image of wastewater biofilm flocs.....	122
Figure 5.2: Percent NPs adsorbed by <i>B. subtilis</i> as a function of time in 10 mM NaCl. Concentrations of 0.25 OD (blue diamond's) and 0.5 OD (purple crosses) were chosen for concentration dependant analysis of the sorption of S-pos NP suspended in 10 mM NaCl. The sorption of S-ned NPs was also tested (red squares) for a concentration of 0.5 OD <i>B. subtilis</i> . A blank experiment (green triangles) containing S-pos NPs without bacteria was also run. Each data point represents the average of triplicate experiments with associated standard deviation ($\sigma = 1$, shown as error bars).	125
Figure 5.3: NP sorption as a function of pH and ionic strength.....	126
Figure 5.4: NP desorption vs. adsorption experiments.	127
Figure 5.5: Percent Fe (NPs) adsorbed by wastewater biofilm as a function of time in 10 mM NaCl.	128
Figure 5.6: NP sorption onto 2 g wastewater biofilm as a function of pH in 1 mM (blue triangles), 10 mM (red squares) and 100 mM (green triangles) NaCl electrolyte concentration. Each data point represents the average of triplicate experiments with associated standard deviation ($\sigma = 1$, shown as error bars)..	129
Figure 5.7: TEM micrographs of <i>B. subtilis</i> cells reacted with s-posNPs. (a) pre- and post-stained sample, (b) post stained sample, (c) and (d) unstained sample. NPs = nanoparticles, CP = cytoplasm, CW = cell wall.	130
Figure 5.8: TEM images of biofilm reacted with s-posNPs. All images are post-stained. Arrows indicate possible NPs.	131

Acknowledgement

The completion of this thesis would not have been possible without the help and support from a number of people to whom I would like to express my gratitude.

Firstly I would like to thank my supervisors Vernon Phoenix and Martin Lee. Your enthusiasm and limitless knowledge have been invaluable to me over the past four years and have made this journey an unforgettable one. I am also indebted to Dominique Tobler for the many hours spent in the lab, discussing ideas and planning experiments. You have been essential to the success of this PhD. Thanks are also due to Ian MacLaren with whom I spent many hours hunting for nanoparticles in calcite grains with. I could not have completed this work without the help of many academics, support staff and undergraduate students, these include (in no particular order): Margret Mullin, Peter Chung, Robert McDonald, Les Hill, John Gilleece, Margret Jackson, Jacqueline Mckie, Garry Tate and Holly Clark. I would also like to thank the Biogeo group for their helpful feedback on my papers and presentations in addition to providing fascinating discussions on biominerals, biogeochemistry and climate change.

A big thank you to all my office mates, past and present for filling the past four years with lots of laughs, cups of tea and numerous bottles of wine! A special thank you goes to Jill, Heather and Eric you guys have been such a support to me through the many highs and lows over this time. And to Callum for providing some much needed stress relief on the squash court! Thanks also go to my home girls - Amy, Lyndsey, Jenny and Lydia who have provided me with invaluable advice and encouragement over the past 10 or so years. And to Catriona, thank you for believing that I could do it even when I thought I couldn't.

Above all I would like to thank every member of my family (too numerous to mention individually) for your unconditional love and support. In particular thank you to my Mum, you have guided me throughout my life and supported me in every decision (good and bad) that I have made. I could never have realised my potential without you. Thank you.

Author's declaration

I declare that the material presented in this thesis is the result of my own work carried out in the School of Geographical and Earth Sciences, University of Glasgow. This research was supervised by Dr. Vernon Phoenix, Dominique Tobler and Martin Lee. Any published or unpublished work by other authors has been given full acknowledgement in the text.

A handwritten signature in black ink, appearing to read 'Rebecca Skuce', written in a cursive style.

Rebecca Skuce

List of parameters

A_{11}	Hamaker constant of nanoparticles
A_{22}	Hamaker constant of calcite
A_{33}	Hamaker constant of water
A_{132}	Combined Hamaker constant
C	Molar concentration
C_T	Dissolved inorganic carbon
$C_{Tcalcite}$	Dissolved carbon removed by calcite precipitation
$C_{Tinitial}$	Initial dissolved inorganic carbon
C_{Turea}	Dissolved carbon produced by ureolysis
e	Electric charge
I	Ionic strength
k^{-1}	Debye length
k_B	Boltzmann constant
k_s	First order rate constant
K_{SO}	Equilibrium calcite solubility product
k_p	Calcite precipitation rate constant
n	Reaction order
N_A	Avogadro's number
R	Bacterial membrane
r_p	Nanoparticle radius
S	Saturation state
S_0	Saturation state at time zero
S_{crit}	Critical saturation state
S_t	Saturation state at time
t	Time
V_{elec}	Electrostatic energy

V_{total}	Total interaction energy
V_{vdW}	Van der Waals energy
z	Ion charge
ε	Dielectric constant
ε_0	Permittivity of free space
φ_p	Nanoparticle zeta potential
φ_c	Calcite zeta potential
λ	Characteristic wavelength

Acronyms

AAS	Atomic Adsorption Spectroscopy
Bs1	First <i>Bacillus subtilis</i> adsorption experiment
Bs2	Second <i>Bacillus subtilis</i> adsorption experiment
Bs3	Third <i>Bacillus subtilis</i> adsorption experiment
DLVO	Derjaguin-Landau-Verwey-Overbeek (theory)
DLS	Dynamic Light Scattering
EELS	Electron Energy Loss Spectroscopy
FIB	Focuses Ion Beam
l-negNP	Large negatively charged nanoparticle
NP	Nanoparticle
NP-I	Nanoparticle Immobilisation
OD	Optical Density
SAED	Selected Area Electron Diffraction
SDW	Sterile Deionised Water
SEM	Scanning Electron Microscopy
s-negNP	Small negatively charged nanoparticle
s-posNP	Small positively charged nanoparticle
STEM	Scanning Transmission Electron Microscopy
TEM	Transmission Electron Microscopy
WB1	First wastewater treatment biofilm adsorption experiment
WB2	Second wastewater treatment biofilm adsorption experiment

1 Introduction

1.1 Nanoparticles

Nanoparticles (NPs) are defined as particles with at least 2 dimensions less than 100 nm (Peralta-Videa et al., 2011). NPs can either occur naturally, or they can be manufactured for specific tasks. Natural NPs have existed on Earth since the beginning of time, being formed by both geogenic and biogenic mechanisms (Handy et al., 2008b, Nowack and Bucheli, 2007).

Geologic processes include physiochemical weathering, where by abrasion and dissolution weather rock fragments which naturally contain particles within the nano size range (Handy et al., 2008b, Hochella et al., 2008). In addition mechanical grinding within earthquake fault zones can create ultrafine grained rock fragments down to 10 to 20 nm in size (Hochella et al., 2008, Wilson et al., 2005). Furthermore, volcanic processes, including geothermal/hydrothermal activity produce a vast array of nanoparticles. For example Esquivel and Murr (2004) found aggregates of carbon nanotubes and silica NPs (thought to be volcanic in origin) trapped within a Greenland ice core dating back to 10,000 years ago. Whilst Rietmeijer (1997) examined upper stratospheric dust which contained bismuth oxide NPs formed from fumarolic volcanic gases. Rietmeijer (1997) linked these NPs to volcanic eruptions which occurred in the 1980's such as Mount St. Helens and El Chicon. Other natural atmospheric NPs include sea salt aerosols formed from the mechanical disruption of the ocean surface (Hochella et al., 2008, O'Dowd et al., 1997). Whilst interplanetary dust particles and meteorites also contain small concentrations of diamond nanoparticles, thought to be produced by supernova sources (Hochella et al., 2008, Verchovsky et al., 2006).

Biological processes often function at a nano-level. For example proteins, peptides and viruses all exist within the nano size range (Handy et al., 2008b). Furthermore, humic and fulvic acids (50-200 nm in size) may also be released into the natural environment by the degradation of biological matter (Handy et al., 2008b). In addition the process of biomineralisation produces minerals on a nano-scale. This includes biogenic iron and manganese (oxyhydr)oxide NPs (Nowack and Bucheli, 2007, Handy et al., 2008b, Hochella et al., 2008). For more information on biogenic mineral formation see section 1.3.1.

NPs have also been unintentionally produced via anthropogenic processes for thousands of years, primarily as a consequence of combustion (Nowack and Bucheli, 2007). For example nano-sized black carbon forms due to the incomplete combustion of fossil fuels whilst carbon black NPs can be found in industrial soot formed from the manufacturing of automobile tires (Nowack and Bucheli, 2007). In addition, platinum and rhodium NPs are produced as a by product of automotive catalytic converters (Zereini et al., 2001, Nowack and Bucheli, 2007).

1.1.1 Natural and anthropogenic nanoparticle toxicity

Life on Earth has been exposed to natural NPs throughout evolution and so organisms are assumed to have adapted to living with these materials (Handy et al., 2008b). However toxicity occurs as a function of exposure and dose (Handy et al., 2008b). For example the lungs have adapted mechanisms to clear small amounts of airborne particles (Handy et al., 2008b). They have not evolved to operate under more extreme environmental conditions such as a volcanic eruption. Prolonged exposure to NPs in volcanic ash can cause respiratory problems such as asthma, bronchitis, silicosis and chronic obstructive pulmonary disease (Horwell and Baxter, 2006).

Anthropogenic NP toxicity has generated much attention over recent years. Atmospheric NPs produced via the combustion of fossil fuels have shown enhanced toxicity due to their enhanced residence time (Kumar et al., 2010). This means that atmospheric particles which fall within the nano-size range are more likely to persist within the atmosphere, increasing the likelihood of penetration in respiratory and cardiovascular systems (Kumar et al., 2010). When inhaled nano-carbon (formed from vehicle emissions) can cause oxidation stress, pulmonary inflammation and cardiovascular events (Kumar et al., 2010, Nel et al., 2006). Whilst with regards to the natural environment, platinum NPs produced from catalytic converters have found to cause increased toxicity to kiwifruit pollen (Speranza et al., 2010). Speranza et al. (2010) discovered that platinum NPs of 5-10 nm altered kiwifruit pollen morphology and penetrated the grains rapidly and to a greater extent than compared to soluble platinum. In addition the grains underwent plasma membrane damage, resulting in the cessation of pollen tube emergence (Speranza et al., 2010). These findings hold

implications for in vivo pollen function with the potential for ecosystem level impacts (Speranza et al., 2010).

1.1.2 Manufactured nanoparticles

The nanotechnology industry is now a multibillion dollar industry, estimated to be worth 3.1 trillion by 2015 (Network, 2010). With large investment into this sector, a diverse array of NPs are now being produced on an industrial scale with consumers using nano-containing products daily (Shi et al., 2011). As we look to the future, nanomaterials are becoming increasingly complex as we push to discover novel products to meet our consumer and energy demands (Maynard et al., 2011).

A diverse array of nanomaterials currently exist, based on their chemical form Li et al. (2006) classified them into 4 categories: 1) carbon based materials such as carbon nanotubes and fullerenes (see Figure 1.1), 2) metal based particles such as nano gold, silver and metal oxides, 3) dendrimers which encompass many forms of nano-scale polymers and 4) composites which involve the production of NPs with more than 1 material (such as gold-silver composite nanoparticles, Figure 1.2). The applications of NPs are endless and are found in almost every aspect of society. A selection of nano-containing products currently on the market today can be seen in Figure 1.3. In the UK existing nano-containing products include:

- Sunscreens - contain zinc and titanium dioxide NPs due to their high UV light sorbing capacity (Weir et al., 2012).
- Antimicrobial wound dressings - contain silver NPs due to their enhanced antimicrobial, antifungal and antiviral properties (Rai et al., 2009). In addition wounds treated with silver NPs exhibit scarless healing (Rai et al., 2009).
- Self-cleaning windows - hydrophobic surfaces act to clean the window through the action of water whilst the hydrophobic layer carries away dirt by a process called sheeting (Parkin and Palgrave, 2005).

- stain resistant clothing - hydrophobic surfaces allow contaminants to adhere to the water droplets which repels the textile surface (Coyle et al., 2007).
- paints - contain titanium and zinc oxide NPs which enhance the light scattering properties of paint (Pilotek and Tabellion, 2005).

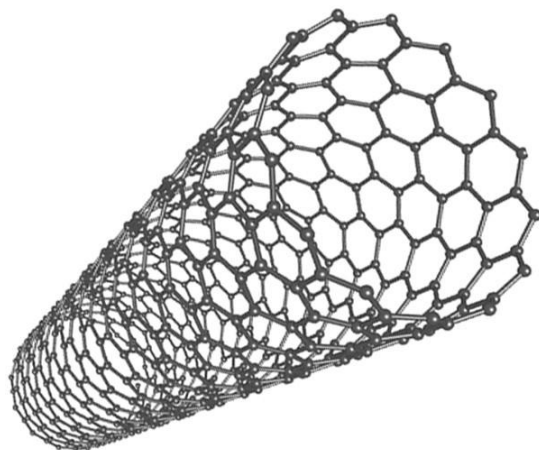


Figure 1.1: Diagram of a single-wall carbon nanotube (Allotropes, 2013).

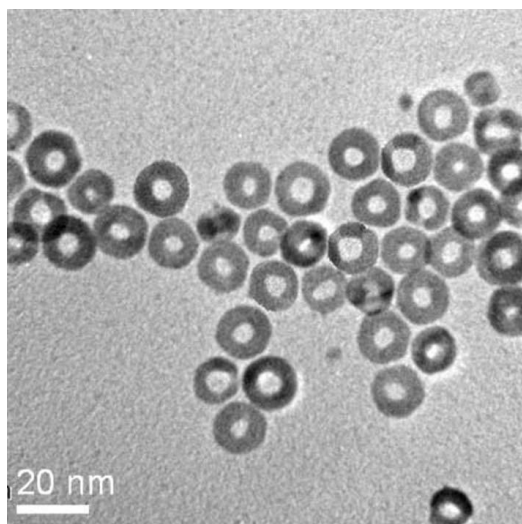


Figure 1.2: Silver - gold core – shell NPs (Yee, 2007).



Figure 1.3: A selection of current nano-containing products currently on the market (Chatterjee, 2008).

In addition to commercial manufacturing, nanotechnology research and development has seen continual global growth over recent years (Chen et al., 2013). Emerging research and development areas include:

- Human health - NPs may be used in targeted drug delivery reduces patient side effects (Pautler and Brenner, 2010). Advances are also being made in the design of medical instruments; for example lysozyme-silver NP coatings on medical instruments offer sustained antimicrobial activity over a wide range of microorganisms (Eby et al., 2009).
- Defence - carbon nanotubes spun into fibres in a polymer matrix have the potential to create electrically conductive fibres, sensors, electromagnetic shielding, microwave absorption and electrical energy storage (Kurahatti et al., 2010). Nanocomposites in body armour allow for more flexible armour with reduced weight and an enhanced capacity to absorb energy (Kurahatti et al., 2010).
- Energy - magnetic NPs and nanofluids have the potential enhance the performance of an array of solar engineering systems (Mahian et al., 2013, Frey et al., 2009) whilst nanogenerators have the capability of harvesting large scale mechanical energy such as footsteps, rolling wheels, wind power and ocean eaves (Zhu et al., 2013).

- Agriculture - nano-fertilisers have the potential to minimise nutrient loss in fertilisation, protect against photodegradation and increase production rates through enhanced reactivity (Gogos et al., 2012). Nano-pesticides offer effective, targeted control of pests and reduce the environmental footprint compared conventional pesticides (Gopal et al., 2012). NPs also offer advances in contaminant remediation. This is discussed further in section 1.1.5.

Nanotechnology has the potential to greatly improve communication, increase data storage, advances in medicine and make an array of technological applications faster and cheaper (Wang et al., 2013).

1.1.3 Manufactured nanoparticle toxicology

The continual increase in the production of NPs and nano-containing products has sparked debate between the public, scientific and regulatory bodies as to the fate and toxicity of nanoparticles in environmental systems. Elevated concentrations of NPs in the environment are extremely likely due to the unintentional release of NPs via production, use and disposal of NPs and nano-containing products (Board, 2009, Petosa et al., 2012). Additionally, NPs are also intentionally released into the environment for the *in-situ* remediation of many ground water contaminants. This is discussed further in section 1.1.5.

Many problems are faced when assessing NP toxicology due to the diverse array of NPs which are currently produced. This makes it extremely difficult for toxicologists to adequately assess the ecotoxicity of nanoparticles. Indeed, relatively inert materials may exhibit toxic effects when produced at the nanoscale due to the unique physiochemical properties exhibited by nanoparticles, in particular their large surface area to volume ratio (Ju-Nam and Lead, 2008). As particle size decreases, surface area increases (Figure 1.4), this means that more atoms exist on the surface relative to the inside of the NP (Nel et al., 2006). Hence, NPs regardless of their composition, are biologically more reactive (Dhawan and Sharma, 2010). In addition to this NPs have access to biological regions where larger particles would be inhibited (Dhawan and Sharma, 2010). For example NPs may attach to cellular membranes and enter

cells, causing the disruption of cellular functions (Bystrzejewska-Piotrowska et al., 2009).

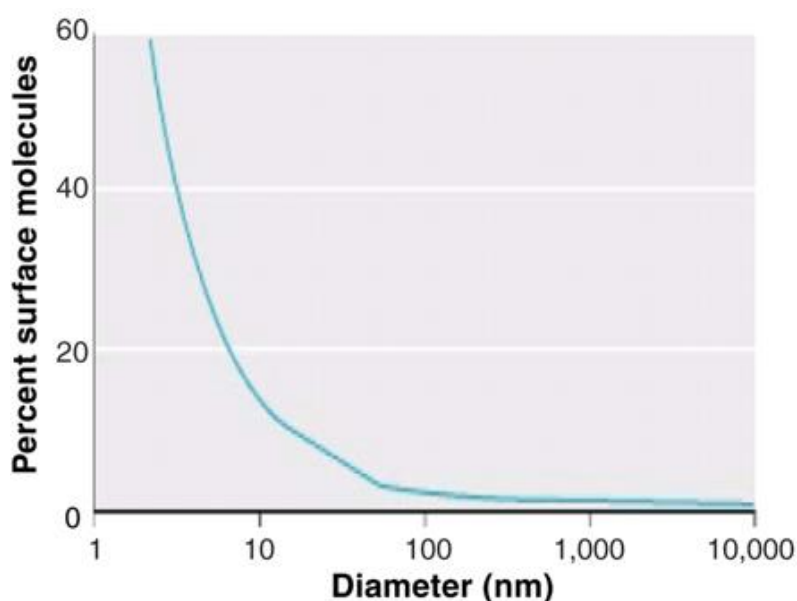


Figure 1.4: This graph displays the inverse relationship between particle size and the percent of surface molecules (Nel et al., 2006).

In addition manufactured NPs are chemically complex in nature, being composed of a vast array of materials. They can be carbon based, metal based, composite layered NPs and/or coated with an external stabilising agent (Handy et al., 2008b). This will affect NP size, shape, stability and ultimately their potential toxicity to human health and the environment (Dhawan and Sharma, 2010). For example NPs composed of cadmium selenide exhibit toxicity due to the release of Cd^{2+} ions from the particle surface (Bystrzejewska-Piotrowska et al., 2009).

NPs may be transported via air and water, and as such this will impact their toxicological effects. For the purpose of this study only waterborne NPs are discussed. The toxicological affects of some widely used waterborne NPs are discussed below:

- Carbon nanotubes - freshwater trout exposed to single walled carbon nanotubes experienced gill injuries, respiratory distress and an increased risk of mortality with prolonged exposure (Smith et al., 2007).
- Gold NPs - Bar-Ilan et al. (2009) discovered that gold NPs are taken up by the embryos of exposed zebrafish. However the presence of gold NPs

caused minimal toxic effects, producing less than 3 % mortality at 12 hours post-fertilisation.

- Silver NPs - Bar-Ilan et al. (2009) found that silver NPs were also taken up by the embryos of exposed zebra fish. In contrast silver NP exposure produces almost 100 % mortality at 12 hours post fertilisation due to a variety of embryonic morphological malformations. Silver NPs have also shown ecosystem level impacts in field experiments. Colman et al. (2013) applied environmentally relevant concentrations of silver NPs via sewage biosolids to terrestrial mesocosms. Long-term analysis showed an increase in nitrous oxide fluxes, changes in microbial community composition, a reduction in microbial biomass by 35 % as well as bioaccumulation of silver NPs in the tissue of above ground plants such as *Microstegium vimineum* and *Lobelia cardinalis*.
- Quantum dots - Kim et al. (2010a) found that quantum dots become unstable when exposed to UV light, releasing toxic metals from the core and generating reactive oxygen species resulting in lethal toxicity to *Daphnia magna*.
- Metal oxide NPs - waterborne zinc oxide NPs exhibited significant effects on the survival, growth and reproduction in the marine amphipod *Corophium volutator* at concentrations as low as 1 mg/l (Fabrega et al., 2011). Jiang et al. (2009) tested the toxicity of aluminium, silicon, titanium and zinc oxide NPs to 3 bacteria strains (*Bacillus subtilis*, *Escherichia* and *Pseudomonas fluorescents*). Zinc oxide NP exhibited superior toxicity, causing 100% mortality to all tested bacteria. Whilst aluminium oxide NPs were lethal to 57% *Bacillus subtilis*, 36% *Escherichia* and 70% *Pseudomonas fluorescents* and silicon oxide NPs to 40% *Bacillus subtilis*, 58% *Escherichia* and 70% *Pseudomonas fluorescents*.

1.1.4 Physiochemical properties of Nanoparticles

Manufactured NPs exhibit a wide range of physiochemical properties due to their diverse and complex nature. The physiochemical properties of NPs are dependant and influenced by NP size, shape and surface properties. Of these, NP size is critical. It has long been known that material properties change as a

function of size, however, within the nano range (1-100 nm) an unfamiliar transition zone is approached between the bulk and quantum laws of material science (Hochella Jr, 2002). Here, the atomic and electronic structures of particles are altered resulting in enhanced catalytic, optical and magnetic properties which are not exhibited by that same material at the macroscale (Guczi et al., 2012, Maillard et al., 2007, Hochella Jr, 2002). For example, gold is an inert material at the macroscale, however in NP form it is far more reactive, being utilised for its enhanced catalytic properties, allowing for the oxidation of CO and methane and the reduction of O₂ (Yang et al., 2003, Della Pina et al., 2008, El-Deab and Ohsaka, 2003). Such phenomena occur as particles approach the nanometre range as a higher percentage of atoms are exposed on the surface relative to the particle interior (Figure 1.4), (Roduner, 2006). For instance, a NP with a diameter of 1 nm exhibits 100% of its atoms on the surface whilst a NP of 10 nm displays only 15 % of its atoms on the surface (Rao et al., 2002).

At first, size seems a simple parameter to determine. However in reality this is complicated as size can change throughout the lifetime of a nanoparticle. Many are prone to aggregation, thus increasing NP size (Levard et al., 2012). Equally some are stabilised and so are inhibited from aggregation (Illés and Tombácz, 2003, Kvitek et al., 2008, Stankus et al., 2010). This is where NP surface properties come into play. NPs are thought to follow the laws of colloidal science demonstrated by the classical Derjaguin, Landau, Verwey and Overbeek (DLVO theory). DLVO theory attempts to describe and explain the stability of charged surfaces in solution. DLVO combines the electrostatic repulsion and the van der Waals attraction to create a total interaction energy which explains why some charged surfaces agglomerate while other remains stable.

To understand electrostatic repulsion an understanding of the electronic double layer (EDL) model is required. Figure 1.5 shows a highly negatively charged NP or colloid. Surrounding this is a layer of strongly bound immobile positively charged ions (counter-ions), termed the stern layer. Beyond this is the diffuse layer, here positive ions exist being attracted by the negative charge of the nanoparticle. The magnitude of positive ions decreases with distance from the colloid until an equilibrium with the bulk solution is reached. Ions in the diffuse layer are mobile but are under the influence of the negative charge of

the colloid and so move as one with the colloid. It is the attached stern layer and charged diffuse layer that creates the double layer surrounding the charged surface.

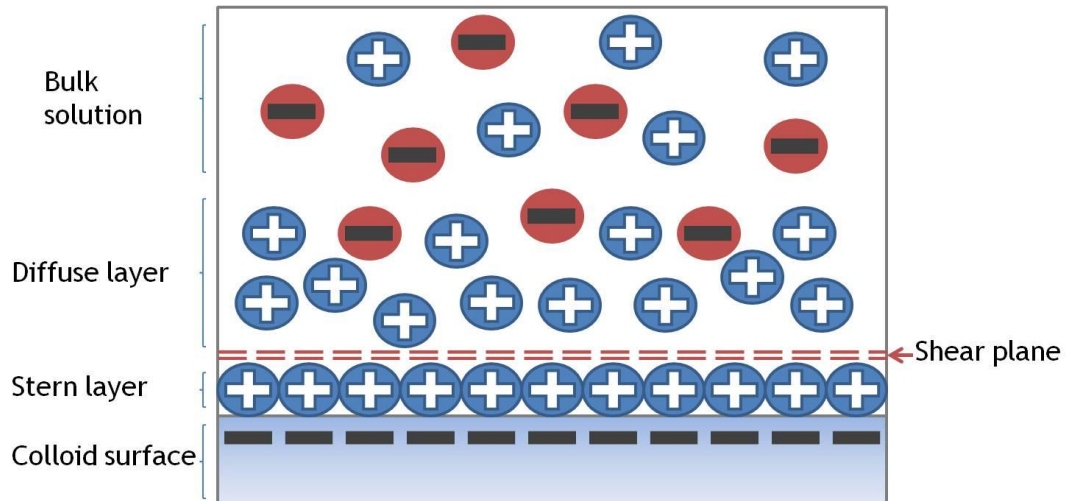


Figure 1.5: Schematic representation of the electronic double layer.

In DLVO theory electrostatic effects come into play when two charged surfaces approach each other and their double layers begin to overlap. If the two surfaces are similarly charged an energy barrier is required to overcome the electrostatic repulsion for attachment to occur, this is demonstrated by an electrostatic repulsion curve. A maximum energy exists as the charged surfaces are almost touching, reducing to zero beyond the EDL. The magnitude of the energy barrier is related to the zeta potential of the charged surface. Indeed, two surfaces of opposite charge will exhibit no electrostatic repulsion and therefore no energy barrier (assuming attractive Van der Waals forces).

Van der Waals attraction results from the force between two permanent dipoles (Keesom force), the force between a permanent dipole and an induced dipole (Debye force) and instantaneously induced dipoles (London dispersion forces). The Keesom force occurs when two polar molecules approach each other. The partially negative side of one molecule is attracted to the partially positive side of the other. This is often referred to as the dipole-dipole interaction. Debye or induced dipole interactions occur when a polar molecule induces a dipole moment in a nonpolar molecule by creating an uneven electronic configuration in the nonpolar molecule. Whilst the London dispersion forces arise

from the orbit of electrons around atoms and molecules, creating an uneven distribution of electrons. This uneven distribution of electrons induces weak dipole moments between atoms and molecules. The combination of these two opposing forces (van der Waals attraction and the electrostatic repulsion) creates a total interaction energy curve (Figure 1.6). In order for attraction to occur the charged surfaces must have sufficient energy to overcome the energy barrier. The energy barrier may be altered by changing the zeta potential of the charged surface.

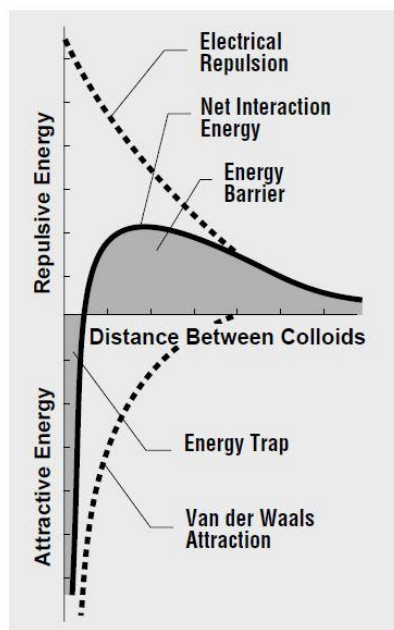


Figure 1.6: Total (net) interaction energy curve produced combination of the van der Waals attraction from the electrostatic repulsion curve.

Zeta potential is a measure of the electric potential at the share plane which separates the stern and diffuse layer (Vidojkovic et al., 2011). At this point the electric potential begins to decrease exponentially away from the NP surface, controlling particle mobility and thus influence zeta potential of the particle. Generally NPs with a zeta potential of either +30 or -30 mV exhibit extremely stable suspensions, above this range particles will strongly repel one another, offering a stable suspension (Instruments, 2011). However, below this range NPs are prone to aggregation. Particle charge is strongly influenced by solution pH and ionic strength (Fang et al., 2009). As pH increases, the NPs surface deprotonates (i.e. releases H^+ ions) generating an increase in negative

surface charge (Figure 1.7). Solution ionic strength also affects particle zeta potential due to the compression of the EDL at high ionic strengths. In addition the valency of the ions also has to be taken into consideration. For example a trivalent ion such as Fe^{3+} will compress the EDL to a greater extent compared to a monovalent ion such as K^+ .

Aggregation may be avoided by modifying the surface of the NP by the addition of surface coatings. This offers a long range steric repulsion even in conditions of high ionic strength (Tiraferrri and Sethi, 2009). Recent studies have shown success with surface coatings of guar gum, humic acid, tween, potato starch to name but a few (Tiraferrri and Sethi, 2009, Kanel et al., 2007, He and Zhao, 2005).

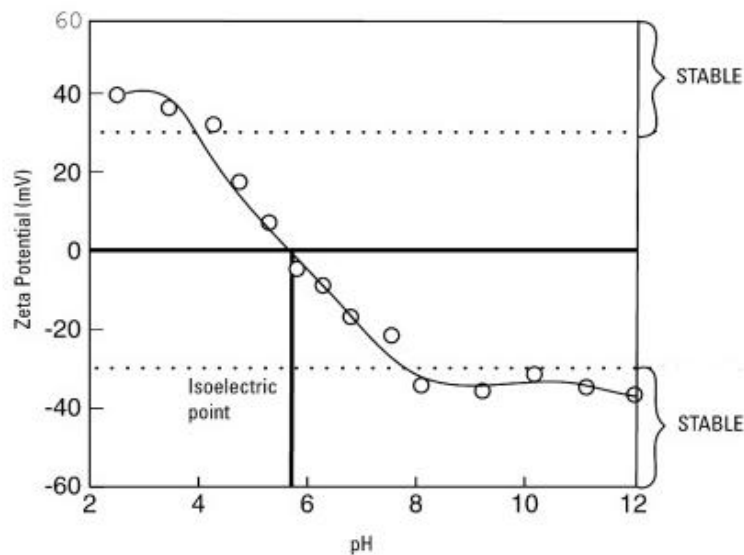


Figure 1.7: A typical zeta potential vs pH plot (Silver-Colloids, 2012).

1.1.5 Nanoparticles used in remediation

The physiochemical properties of NPs make them excellent candidates for use in environmental clean up strategies. They offer key advantages to traditional methods, such as pump and treat. Due to their nanometer size and unique surface coatings, NPs may be transported to both the pollutant source and plume, thus enabling the in-situ remediation of large contaminated areas (Kanel et al., 2007). NPs are also excellent catalysts, greatly reducing the clean up time of contaminated systems (Handy et al., 2008b). Nanotechnology has the

potential to provide faster, cost effective environmental clean-up strategies whilst reducing many common groundwater contaminants to near zero, all *in-situ* (Wong et al., 2009).

NPs proposed for use in contaminant remediation include various metal oxides, carbon nanotubes and titanium dioxide and nano zero valent iron (nZVI, Karn et al., 2011). Of these nZVI is the most commonly used. nZVI has shown high success rates for the remediation of various organic and inorganic soil and groundwater contaminants ranging from chlorinated solvents to a wide range of heavy metal ions (Misra et al., 2011, Fein et al., 2005, Mueller et al., 2012). The versatility of nZVI to treat a wide range of environmental contaminants is a result of oxidation of the zero valent iron core, forming an oxide shell (Wong et al., 2009). This core shell structure allows enhanced chemical removal via two mechanisms. The zero valent iron core provides a reducing agent due to its electron donating properties whilst the oxide shell exhibits a strong sorptive character via electrostatic interactions and surface complexation mechanisms (Kanel et al., 2007). Presently nZVI is being used extensively in the US for contaminant remediation whilst a few cases exist in Europe, namely Czech Republic, Italy and Germany (Wong et al., 2009). The results of nZVI treated sites look promising, for example a contaminated site in Bornheim, Germany saw a 90% reduction of total chlorinated compounds (Wong et al., 2009). No adverse environmental problems have been reported thus far, however the long term effects of nanoremediation are poorly understood. As a result continual environmental monitoring of nZVI-remediated sites is essential in order to prevent any adverse environmental impacts (Karn et al., 2011, Wong et al., 2009).

1.1.6 Environmental exposure to nanoparticles

Evidence suggests that the uncontrolled release of nanomaterials through the use and disposal of nano-containing products has led to the emergence of NPs within the natural environment (Museum, 2011). As the volume of nano-containing products increases this will inevitably lead to their accumulation in the environment (Simonet and Valcárcel, 2009). To this point, no published data exist for nano-waste volume, however, reasonable estimates can be inferred by the production volumes of NPs and nano-containing products (EEA, 2002). In

2004 1000 tonnes of nanomaterials were produced globally. This figure is estimated to increase to 58,000 tonnes annually between the years 2011 and 2020 (Musee, 2011, Engineering, 2004). A significant source of nano-waste to the natural environment may occur via point sources such as landfill, wastewater treatment works and industrial waste streams, whilst nonpoint sources include wear and tear of nano-containing products (Musee, 2011, Powell et al., 2008). Figure 1.8 highlights the potential routes of exposure and transformations of NPs in environmental systems. In addition, NPs may be intentionally released into the environment for contaminant remediation purposes, (see section 1.1.5). Once released into the environment, NPs may undergo a variety of transformations such as redox reactions, aggregation and dissolution (Figure 8, Lowry et al., 2012b). For example when exposed to a large scale microcosm, replicating a freshwater wetland, silver NPs underwent almost complete sulfidation over a period of 18 months (Lowry et al., 2012a). This altered the particles aggregation state, surface chemistry and charge (Lowry et al., 2012b). However under the experimental conditions tested here Lowry et al. (2012a) found that Ag ions remained bioavailable to the plants and biota living within the microcosm. In addition NPs may be intentionally stabilised with a variety of surface coatings such as guar gum and humic acid (Simonet and Valcárcel, 2009, Tiraferri and Sethi, 2009) which will inhibit particle aggregation (see section 1.1.4). NP surface properties will ultimately determine the fate, transport and toxicity of NPs in environmental systems.

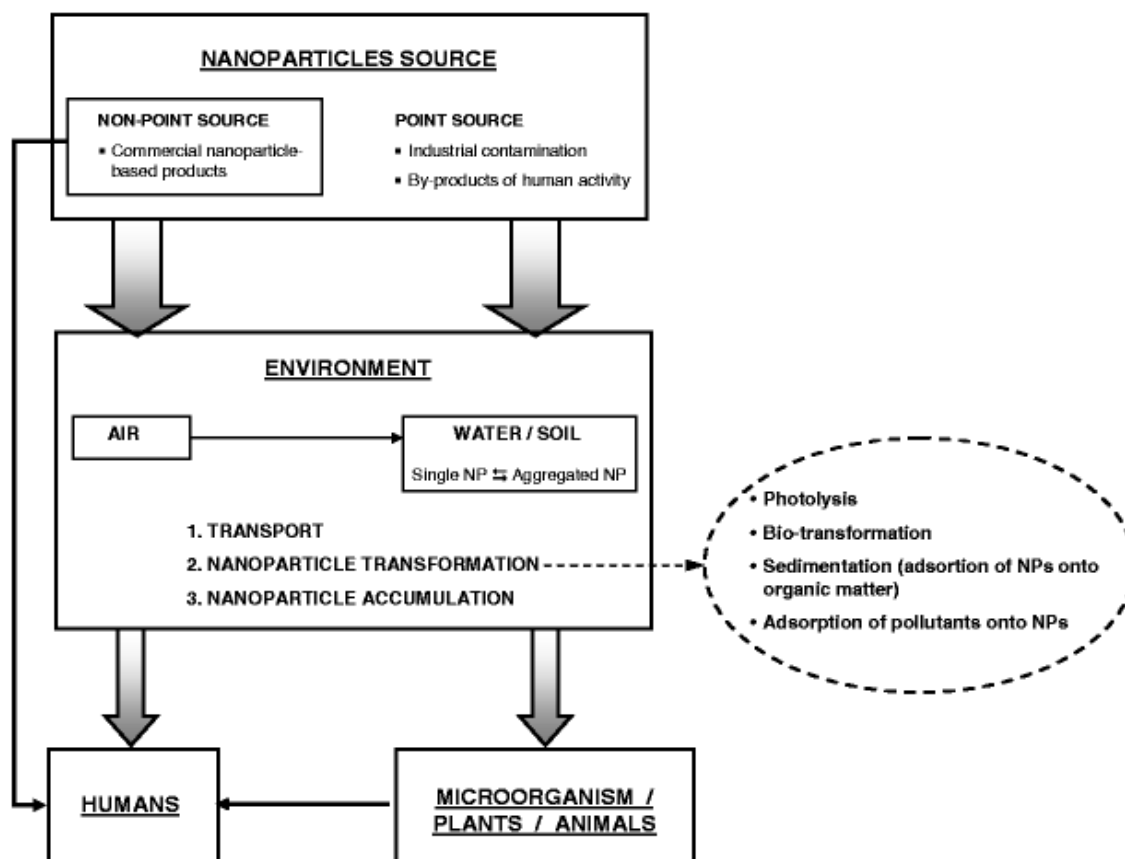


Figure 1.8: Routes of exposure and transformations of NPs in the environment (Simonet and Valcárcel, 2009).

1.2 Bacteria

Bacteria consist of a large group of prokaryotic microorganisms that are ubiquitous to every environment on Earth. They are an extraordinarily diverse group of microorganisms that differ in size, shape, habitat and metabolism (Britannica, 2014). Bacteria have the ability to metabolise an array of organic and inorganic compounds and in doing so they have a crucial role to play in the biogeochemical cycling of elements in all our ecosystems (Banfield and Nealson, 1997). For example nitrogen fixing bacteria convert atmospheric nitrogen into useable fixed nitrogen compounds (such as ammonia, nitrates or nitrites). Without them, soils would no longer be fertile. Bacteria are also found in Earth's most extreme environments. Their adaptability means they can withstand extreme temperatures, pressures and aqueous chemistry allowing them to colonise mid ocean ridges (Kelley et al., 2001), polar ice caps (Price, 2000) and acid mine drainage streams to name but a few (Baker and Banfield, 2003).

1.2.1 Biofilm

Biofilms can be described as aggregated communities of microorganisms (O'Toole et al., 2000, Stoodley et al., 2002). Biofilms differ greatly to their individual planktonic counterparts, having key advantages of antimicrobial resistance, better availability to nutrients and are capable of withstanding greater environmental stress (Donlan, 2002, Palmer et al., 2007, Stanley and Lazazzera, 2004). They can form on solids, liquids and on living tissue (such as animal and plant tissues), (Britannica, 2014). Biofilm formations may be composed of a single bacterial species or a multiple community including eukaryotic organisms such as algae and fungi (O'Toole et al., 2000, Palmer Jr and White, 1997). However mixed communities are more common in environmental systems whilst single species more likely to occur as an infection or on the surface of medical implants (O'Toole et al., 2000). Biofilm growth is initiated by attachment to a surface; however the attachment mechanism is of much contention. Many factors may affect bacterial attachment to surfaces, such as mass transport, surface charge, surface roughness and surface micro-topography (Palmer et al., 2007). Once attachment has been made biofilm growth and cell division may occur. During growth, extracellular polymeric substances (EPS) are secreted, this is crucial to the structure of the biofilm, comprising 50 to 90% of the total organic carbon of the biofilm (Donlan, 2002). In addition EPS prevents biofilm desiccation and contributes to the antimicrobial resistance of biofilm (Donlan, 2002).

1.2.2 Biofilm – nanoparticle interactions

Bacteria - NP interactions hold implications for the transport of NPs within environmental systems. Their presence may facilitate the degradation, sorption and/or generation of NPs (Peulen and Wilkinson, 2011). Ultimately, the mobility and bioavailability of NPs will depend on diffusion coefficients as this is the dominant transport mechanism of NPs into biofilm communities (Peulen and Wilkinson, 2011). Hence, the structure and composition of the biofilm hold important implications for biofilm - NP interactions. Peulen et al. (2011) found that the pore size within the biofilm is crucial to determine whether NP diffusion into the biofilm occurs. Here, NPs larger than 50 nm were excluded from biofilm

formations, suggesting their presence in environmental systems would not affect the transport of larger NPs. In addition, the physiochemical characteristics of NPs are crucial. For example, Li et al. (2013) found that biofilm coated sand grains retained bare NPs through sand column experiments, whilst polymer coated NPs showed high mobility with little retention within the column due to steric repulsion. The physiochemical interactions of NPs are discussed in detail in section 1.1.4.

Biofilms are formed by a variety of microorganisms, under differing growth conditions which produce communities that vary widely in physiology and biochemistry. Coupled with the diverse array of NPs produced bacteria - NP interactions within the natural environment is a complex process which is currently not well understood.

1.3 Microbially mediated mineral formation

1.3.1 General microbial mineral formation

Microorganisms are key players in the precipitation and dissolution of numerous minerals. Mineral formation may be induced or controlled by the microorganism. Biologically induced mineralisation occurs as a by product of the organisms metabolic processes where as biologically controlled mineralisation occurs to serve a physiological purpose to the microorganism (Konhauser, 2009). For example ferrihydrite is a common biologically induced mineral forming in an array of environments ranging from aquifers to mine waters (Konhauser, 2009). This mineral can be precipitated by microbial oxidation of Fe(II) to Fe(III). Mineralisation can be assisted by the adsorption of iron by the cell surface, followed by nucleation and consequently growth until the cell becomes completely encrusted in the mineral precipitate (Konhauser, 2009). Warren and Ferris (1998) demonstrated that ferrihydrite precipitation was enhanced by the presence of bacteria, with precipitation occurring at a lower pH and in greater quantities compared to the abiotic (no bacteria) controls. Here the bacterial cells acted as heterogeneous nucleation templates for ferrihydrite precipitation (Warren and Ferris, 1998). In contrast biologically controlled mineralisation occurs as the microorganism exerts control over the nucleation and growth of the mineral (Bazylinski and Frankel, 2003). For example, magnetotactic bacteria

control the formation of magnetite. The mineral may form on or within the organism or within vesicles inside the cell (Devouard et al., 1998). This allows the organism to exert a high degree of control over biomineralization, forming well ordered crystals which have a narrow size distribution and well defined morphologies (Devouard et al., 1998).

1.3.2 Ureolytically-driven calcium carbonate precipitation

Urea hydrolysis occurs via the urease enzyme (urea amidohydrolase). This enzyme is possessed by numerous bacteria, enabling the enzymatic precipitation of calcium carbonate minerals (calcite, aragonite and vaterite) in a variety of soil and groundwater communities (Tobler et al., 2011, Lesley A. Warren et al., 2001, Martin et al., 2012). As demonstrated by the series of reactions below, this process is initiated by the hydrolysis of urea to ammonia and carbonic acid (Eqn. 1), equilibrating in water to form bicarbonate, ammonium and hydroxide ions (Eqn. 2 and 3). This causes a rise in pH, which combined with the production of bicarbonate, increases the saturation state with regards to calcium carbonate if soluble calcium exists, thus precipitating calcite out of solution (Eqn. 4, Tobler et al., 2011, Warren et al., 2001, Mitchell and Ferris, 2005).



1.3.3 Ureolytically-driven calcium carbonate precipitation technologies

Ureolytically-driven calcium carbonate precipitation has been extensively studied due to its potential in a diverse array of applications including the remediation of heavy metals and radionuclides (Lesley A. Warren et al., 2001, Fujita et al., 2004, Mitchell and Ferris, 2005), soil stabilisation (Whiffin et al., 2007), wastewater treatment (Hammes et al., 2003) and carbon capture and storage (Mitchell et al., 2010) Martin et al., 2012.

1.4 Research objectives

This PhD research examines microbially mediated processes which reduce NP mobility and ultimately immobilise NPs within water and waste water.

Nanotechnology is a rapidly growing field which shows no signs of slowing in the future. Concern arises due to the toxicological effects displayed by some nanoparticles. As NP production increases, so too will human and environmental exposure to nanoparticles, resulting in detrimental effects to human health and the natural environment. However, in order for NP toxicity to present a real threat, a route of exposure must exist. Some NPs which are electrostatically and electrosterically stabilised are highly mobile within environmental systems and so it is these NPs which present the greatest risk with regards to toxicity. This thesis looks to explore microbially mediated processes which can prevent the transport of NPs to sites where they have the potential to cause harm.

Much of this thesis explores the ability of microbial precipitated minerals to immobilize nanoparticles. While, microbially driven mineral precipitation has already been shown to have potential for immobilization of dissolved heavy metals, the capture of NPs has yet to be examined. In addition to this, NP sorption onto planktonic bacteria and granular biofilms is also assessed. This was done to assess the capacity for current municipal wastewater treatment works to remove NPs conventionally through biological treatment.

The key research chapters in this thesis are as follows:

- Chapter 2 - utilizes batch reactions to test the ability of ureolytic calcite precipitation to capture highly stable nanoparticles. This is tested as a function of NP surface charge and size.
- Chapter 3 - builds upon chapter 2, but here the capture of NPs is undertaken inside packed sand columns to explore how this process works inside porous media. This understanding is key if this process were to be scaled up to natural aquifers and soils.
- Chapter 4 - tests the ability of struvite to remove positively charged NPs from water as these were poorly captured by the process of ureolytic calcite precipitation (Chapter 3). The ability of struvite mineral formation to remove ammonia (an undesirable by product of ureolysis) was also tested.

- Chapter 5 - determines the ability of bacteria (*Bacillus subtilis*) and wastewater treatment biofilms to adsorb and remove NPs from solution. The ability of both biosorbent materials to remove (adsorb) NPs is examined as a function of bacterial concentration, pH and ionic strength.

2 Immobilisation of nanoparticles by microbially mediated calcite precipitation

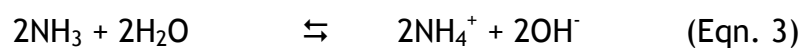
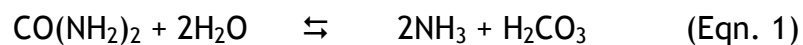
2.1 Summary

Microbial driven mineral precipitation has the potential to capture dissolved heavy metals, impacting the transport and fate of metals in the natural environment. However, the capture of NPs by microbial mineral precipitation has yet to be examined. In this study, the ureolytic bacteria *Sporosarcina pasteurii* was used to induce calcium carbonate precipitation in the presence of organo-metallic manufactured NPs. As calcium carbonate crystals grew the NPs in the solution became trapped within these crystals. Critically, further growth caused the NPs-crystal composite to settle out of suspension. NPs with a negative surface charge were captured with greater efficiency than those with a positive surface charge, likely resulting from stronger attachment of negative NPs to the positively charged calcite surfaces. Thermodynamic and kinetic analysis, however, did not reveal a significant difference in k_p (calcite precipitation rate constant) or the critical saturation at which precipitation initiates (S_{crit}), indicating the presence of different charged NPs did not influence calcite precipitation at the concentrations used here. Overall, these findings demonstrate that bacterially driven solid-phase capture has potential to immobilize NPs, and thus may potentially be utilized to immobilize NPs in contaminated groundwater systems.

2.2 Introduction

Microorganisms have the ability to drive the precipitation of a wide range of minerals (Chapter 1.3). This process can lead to the immobilisation of dissolved metals, either within the crystalline structure of the mineral or bound to the mineral surface. For example, oxidation of Fe(II) and Mn(II) generates metal (hydr)oxides which can absorb a diverse array of dissolved heavy metals and metalloids (Martinez et al., 2004, Martinez and Ferris, 2005, Villalobos et al., 2014, Pei et al., 2013) while enzymatic precipitation of phosphate produces hydroxyapatites which bind significant quantities of dissolved heavy metals and have potential in engineered permeable reactive barriers (Handley-Sidhu *et al.*,

2011). Ureolysis-driven calcium carbonate precipitation has been extensively studied due to its potential in a diverse array of applications including soil stabilisation (Whiffin et al., 2007), concrete crack remediation (De Muynck et al., 2010), fracture and porosity sealing to inhibit pollutant flow (Tobler et al., 2012), wastewater treatment (Hammes et al., 2003), and carbon capture and storage (Mitchell et al., 2010). This process also has potential for solid phase capture of heavy metals and radionuclides, which are incorporated into the calcium carbonate mineral as it crystallizes, thus preventing their mobility in the subsurface. In particular, this approach has been investigated for the solid phase capture of ^{90}Sr ions from contaminated groundwaters; the strontium replacing Ca^{2+} in the crystal lattice (Warren et al., 2001). In this process, ureolysis occurs via the hydrolysis of urea by the urease enzyme generating ammonia and carbonic acid (Eqn. 1). This then equilibrates in water to form bicarbonate, ammonium and hydroxide ions (Eqn. 2&3), causing a rise in pH and an increase in the saturation state with regards to calcium carbonate if soluble calcium is available. Once saturation is reached the precipitation of calcium carbonate minerals such as calcite occurs (Eqn. 4, Tobler et al., 2011).



Calcium carbonate precipitation may also be driven via chemical (abiogenic) precipitation; however biologically driven precipitation of calcium carbonate offers a key advantage of slower precipitation rates. This enables the treatment of a larger target area of the subsurface, as reagents can be injected throughout the target zone before significant precipitation occurs (Tobler et al., 2011). Conversely, rapid abiogenic precipitation is likely to cause blocking of the injection well.

While a diverse array of microbial mineral precipitation pathways have potential to immobilize heavy metals, their ability to capture NPs has yet to be examined. With a rising demand for nanomaterials and continual growth in

production, increased environmental exposure to NPs (NPs) is inevitable (Petosa et al., 2010, Musee, 2011, Luo et al., 2006, Moore, 2006, Nowack and Bucheli, 2007). This has brought NP toxicity to the forefront of research and governmental concern, with the UK government alone spending £10 million during 2005-08 to identify and manage the risks posed by the nanotechnology industry (DEFRA, 2011). Problematically, NPs can have a wide range of toxic effects, exacerbated by their size (at least one dimension smaller than 100 nm, Engineering., 2004). Detrimental effects include brain, intestinal and respiratory injury, delayed embryonic development, DNA damage and increased mortality (Trouiller et al., 2009, Handy et al., 2008a). See Chapter 1.1.3 for further discussion on NP toxicity.

Such findings raise concern with regards to the fate and transport of NPs within the environment. Owing to their small size NPs are highly reactive, making them excellent catalysts (Luo et al., 2006). Increasingly, applications of NPs require them to be highly dispersed, stable suspensions and so NP systems are increasingly being designed to exhibit enhanced stability via modifications of NP surfaces with capping agents and surfactants (Lecoanet et al., 2004, Kanel et al., 2007, Petosa et al., 2012). Such NPs have the ability to be transported more readily within the natural environment (Kanel et al., 2007, Lecoanet et al., 2004). Aside from enhancing NP mobility, stable NP dispersions also exhibit increased toxicity compared to agglomerated NPs due to their large surface area to volume ratio (Levard et al., 2012). For example, Kvitek et al. (2008) demonstrated that increasing the stability of silver NPs enhanced their antibacterial activity. Aside from this highly stable, mobile surface modified NPs also have the ability to bind and transport chemical pollutants, thus enhancing the dispersal of pre-existing contaminants within the environment (Moore, 2006).

It is clear that some NPs are highly stable and therefore mobile under environmental conditions, presenting a route of exposure of NPs to humans and the natural environment (Lecoanet et al., 2004, Ben-Moshe et al., 2010, Petosa et al., 2012). The ability of microbial driven mineral precipitation to immobilise NPs should therefore be examined.

In this study, ureolysis driven calcium carbonate precipitation by the urease positive bacterium *Sporosarcina pasteurii* (*S. pasteurii*) was investigated

as a means of immobilising NPs through solid-phase capture in aqueous systems. Experiments were performed as a function of NP surface charge and size to determine if these factors impacted capture efficiency. Thermodynamic and kinetic interpretation of results were undertaken to determine whether these NP properties had a significant impact on precipitation kinetics and the saturation state required for precipitation.

2.3 Materials and methods

2.3.1 Nanoparticles

The NPs used in this study were chosen as they exhibit exceptionally high stability, even under high ionic strength, and thus do not aggregate. This is important here as this study aims to demonstrate that NPs can be removed from suspension by solid-phase capture as opposed to aggregation processes. Three different types of NPs were used, large and small negatively charged NP and small positively charged NPs (l-negNP, s-negNP and s-posNP respectively, all purchased from BioPAL, USA). They all have a 10nm nano-magnetite core surrounded by dextran. Different size and surface charge result from differing thickness of dextran and differing functional groups upon the dextran (Table 2.1). This allowed testing the effect of surface charge and particle size on the NP removal efficiency of the proposed method.

Because all NPs types contained identical iron-oxide (nanomagnetite) cores, Fe was used as a proxy for NP concentration. This enabled NP concentrations to be determined by acid digestion followed by analysis of Fe concentration by atomic adsorption spectroscopy (AAS). The NP concentration for each experiment was 10 mg L^{-1} Fe. This corresponded to approximately 10^{16} NPs per litre.

Table 2.1: Characteristics of NPs used in this study.

Nanoparticle	Diameter (nm)	Zeta potential (mV)
l-negNP (FeREX)	150	-30.8
s-negNP (Molday ION carboxyl terminated)	35	-38
s-posNP (Molday ION C6Amine)	35	+48

2.3.2 Experimental design

Batch experiments were performed using the gram positive ureolytic bacterium *S. pasteurii* (strain ATCC 11859). Cultures were grown at 25 °C in brain heart infusion broth supplemented with filter-sterilised urea (20g L⁻¹). Cells in exponential phase growth were harvested by vacuum filtration (using sterile 0.2µm membrane filters) and rinsed twice with sterile deionised water (SDW). The bacterial pellet was re-suspended in SDW to a cell count (OD) of 0.14 as determined spectrophotometrically at 600nm (this equates to 2.3 x 10⁶ cells ml⁻¹, based on the *S. pasteurii* OD to cell conversion in (Levard et al., 2012)) and then pH adjusted to 6.5 using HCl to ensure that the system was undersaturated with respect to calcium carbonate precipitation (Analar grade). For each nanoparticle immobilisation (NP-I) experiment, a solution containing 100 mM CaCl₂ and 100 mM urea was prepared and then mixed at a ratio of 1:1 with the bacterial suspension before the addition of nanoparticles. The final concentrations were 50mM CaCl₂, 50mM urea, 10 mg/L NPs (Fe concentration) and 0.07 OD *S. pasteurii*. Biotic controls (*S. pasteurii* + urea + NP) and abiotic controls (CaCl₂ + urea + NP) were also run. Double dosing experiments were undertaken with l-negNPs to determine if any non-captured NPs could be trapped by a second phase of calcium carbonate precipitation. For the double dosing experiment, reactions were set up as described above (using l-negNPs), but once ureolysis and calcite precipitation were completed, urea and CaCl₂ were added once again (to yield final concentrations of 50 mM each), which then induced a second phase of calcium carbonate precipitation.

All nanoparticle immobilisation experiments were carried out in triplicate in glass beakers that were covered with parafilm[®] to prevent evaporation.

2.3.3 Chemical analysis

Analyses of solution pH, NH₄⁺, Ca²⁺ and Fe were determined at time zero and at regular intervals thereafter. At each sampling time, 10 ml aliquots were removed from the experiment; 5ml were used for pH measurement using a Mettler Toledo MA 235 pH/ion analyser, 0.5 ml to determine NH₄⁺ by the Nessler assay (analysis was performed using a Hach Lange DR 5000 spectrophotometer) and 4.5 ml were mixed with 0.5 ml of concentrated HCl for Ca²⁺ and Fe

concentration measurements using AAS. For Fe analysis calibration standards (0.1, 1, 5 and 10 mg/l) were prepared prior to each analysis by dilution of a single element standard for AAS which contained 1000 ppm Fe in nitric acid (purchased from Fisher Scientific). An air-acetylene flame was used for all Fe determinations at a flow rate of 0.8 - 1 l/min. The spectrometer was operated at a wavelength of 248.3 nm and a spectral band pass of 0.2 nm with the lamp current running at 75%. The analytical limit detected under these conditions is 0.06 mg/l. For Ca²⁺ analysis standards of 0.1, 1, 2, 3 mg/l were prepared prior to each analysis using CaCl₂. A nitrous oxide - acetylene flame was used at a fuel flow rate of 4 - 4.4 l/min for all Ca²⁺ analysis. The spectrometer was operated at a wavelength of 422.7 nm and a spectral band pass of 0.5 nm with the lamp current running at 100%. The analytical limit detected under these conditions is 0.015 mg/l.

2.3.4 Transmission Electron Microscopy (TEM)

TEM imaging, selected area electron diffraction (SAED) and chemical analysis was undertaken on thin foils that were extracted from calcite grains using the Focused Ion Beam (FIB) lift-out technique using a FEI Nova 200 Dualbeam. Calcite crystal surfaces were first sputter coated with gold to prevent charging of the mineral surface and ion-implantation into the calcite, followed by further deposition of platinum from an organometallic precursor within the FIB. Foils were thinned using a 30 kV Ga⁺ ion beam to a thickness of ~1 µm prior to being removed from their parent grain using an *in-situ* micromanipulator, and were then welded to the tines of an Omniprobe copper support using electron and ion beam deposited platinum. Final thinning was then performed using lower accelerating voltages and beam currents on these supported thin foils to reduce the total thickness to less than ~60 nm in the thinnest areas in order to facilitate EELS (Electron Energy Loss Spectroscopy), without compromising the crystallinity. Initial characterisation of these foils by diffraction-contrast imaging and SAED was performed using a FEI T20 TEM operated at 200 kV. EELS analysis was performed using a JEOL ARM200F equipped with a Gatan GIF Quantum Electron Energy Loss Spectrometer; the EELS work was undertaken at an accelerating voltage of 80 kV in scanning TEM (STEM) mode using line scans with a nominal step size of about 1 nm.

2.3.5 Kinetic analysis and calcite precipitation

A kinetic and thermodynamic analysis to determine calcite precipitation rate constants and the critical saturation state at which calcite precipitation initiates was performed as detailed by Tobler et al. (2011). This work was done to determine if these parameters were affected by NP properties (size and surface charge), either through NPs acting as nucleation sites for CaCO₃ precipitation, or by interacting with crystal growth during NP occlusion. Details of these calculations are described below.

The precipitation of calcite can be fitted to the following saturation-dependent kinetic expression (Lasaga, Teng et al., 2000):

$$\frac{d[Ca^{2+}]}{dt} = -k_p (S - 1)^n \quad (1)$$

where k_p represents the rate constant for calcite precipitation, S the saturation state and n the reaction order. Based on the findings from Tobler et al. (2011), the data presented here was fitted to first-order ($n=1$, (Dupraz et al., 2009) rate laws.

The saturation state, S , with respect to calcite is defined by:

$$S = \frac{\{Ca^{2+}\}\{CO_3^{2-}\}}{K_{SO}} \quad (2)$$

where $\{Ca^{2+}\}$ and $\{CO_3^{2-}\}$ are the activities of dissolved Ca²⁺ and CO₃²⁻, respectively, and K_{SO} is the equilibrium calcite solubility product. The geochemical code PHREEQC (version 2.13.3; (Parkhurst and Appelo, 1999) and the wateq4 database (Ball and Nordstrom, 1992) were utilised to calculate S values for each step. Here, dissolved inorganic carbon (C_T), i.e., total dissolved carbonate species (as produced by urea hydrolysis), increased over time according to the following mass balance relationship:

$$C_T = C_{Tinitial} + C_{Turea} - C_{Tcalcite} \quad (3)$$

where $C_{Tinitial}$ corresponds to the initial dissolved inorganic carbon concentrations, C_{Turea} is the amount of dissolved carbon produced by ureolysis ($C_{Turea} = [NH_4^+]_t / 2$) and $C_{Tcalcite}$ equals the dissolved carbon removed from solution by calcite precipitation ($C_{Tcalcite} = [Ca^{2+}]_{initial} - [Ca^{2+}]_t$).

The change in saturation state with respect to time (dS / dt) can be described using following first-order mass action:

$$\frac{dS}{dt} = -k_s \left(\frac{\{Ca^{2+}\} \{CO_3^{2-}\}}{K_{SO}} \right) = -k_s S \quad (4)$$

From integration of equation 4, the change in calcite saturation state over time can be described using:

$$S_t = S_0 e^{-k_s t} \quad (5)$$

where S_t is the saturation state at time t , S_0 is the apparent saturation state if precipitation is expected at time zero, and k_s is a first order rate constant for the change in saturation state. S values were calculated for each time step using PHREEQC and the wateq4 database (W. and K., 1992)(W. and K., 1992)(W. and K., 1992). S_0 and k_s were then determined from a plot of $\ln S(t)$ vs. $\ln S_0 - k_s t$.

The rate constant for calcite precipitation (k_p) and S_{crit} , the critical saturation at which precipitation initiates, can be determined from the following first order reaction (Tobler et al., 2011).

$$[Ca^{2+}] = \left(\frac{k_p}{k_s} \right) \left[S - S_{crit} - \ln \left(\frac{S}{S_{crit}} \right) \right] + [Ca^{2+}]_{crit} \quad (6)$$

where S_{crit} is the critical saturation state at which precipitation starts, k_p is the calcite precipitation rate constant, and $[Ca^{2+}]_{crit}$ is the dissolved Ca concentration at S_{crit} (i.e., initial dissolved Ca^{2+} concentration).

To estimate S_{crit} and k_p , Equation 2 was fitted to the experimental data (i.e., S and $[Ca^{2+}]$ over time) using unconstrained nonlinear regression and a quasi-Newton optimization routine for parameter estimation in the STATISTICA v.6.0 software package (Ferris et al., 2004).

2.4 Results

2.4.1 Immobilisation of small negatively charged nanoparticles (s-negNP)

Solid-phase capture was first tested on the s-negNPs (zeta potential -38 mv). In all experiments apart for the abiotic control, urea hydrolysis was

complete within 10 hours (Figure 2.1a). This was accompanied by a sharp rise in pH for the NP-I (nanoparticle immobilisation) and biotic control experiment (Figure 2.2a). As a result, the solution in the NP-I experiment became highly saturated with respect to calcium carbonate, resulting immediately in the precipitation of calcite, as indicated by the rapid decrease in dissolved Ca^{2+} (Figure 2.3a). As calcium carbonate precipitated, the Fe concentration in solution decreased asymptotically indicating the removal of suspended NPs (Figure 2.4a). Importantly, once Ca^{2+} removal ceased after 10 hours, no further decrease in Fe concentration, i.e., NP removal, was observed. Over 80% of the s-negNPs were removed within 1 day, with the majority of this occurring within only 6 hours. By contrast no NP removal was observed in the biotic (*S. pasteurii* + NP + urea) or abiotic (NP + CaCl_2 + urea) control for the s-negNP experiments (Figure 2.4a and b), confirming that NP removal occurred only due to calcium carbonate precipitation (as opposed to, for example, aggregation or attachment to bacteria or the reaction vessel walls).

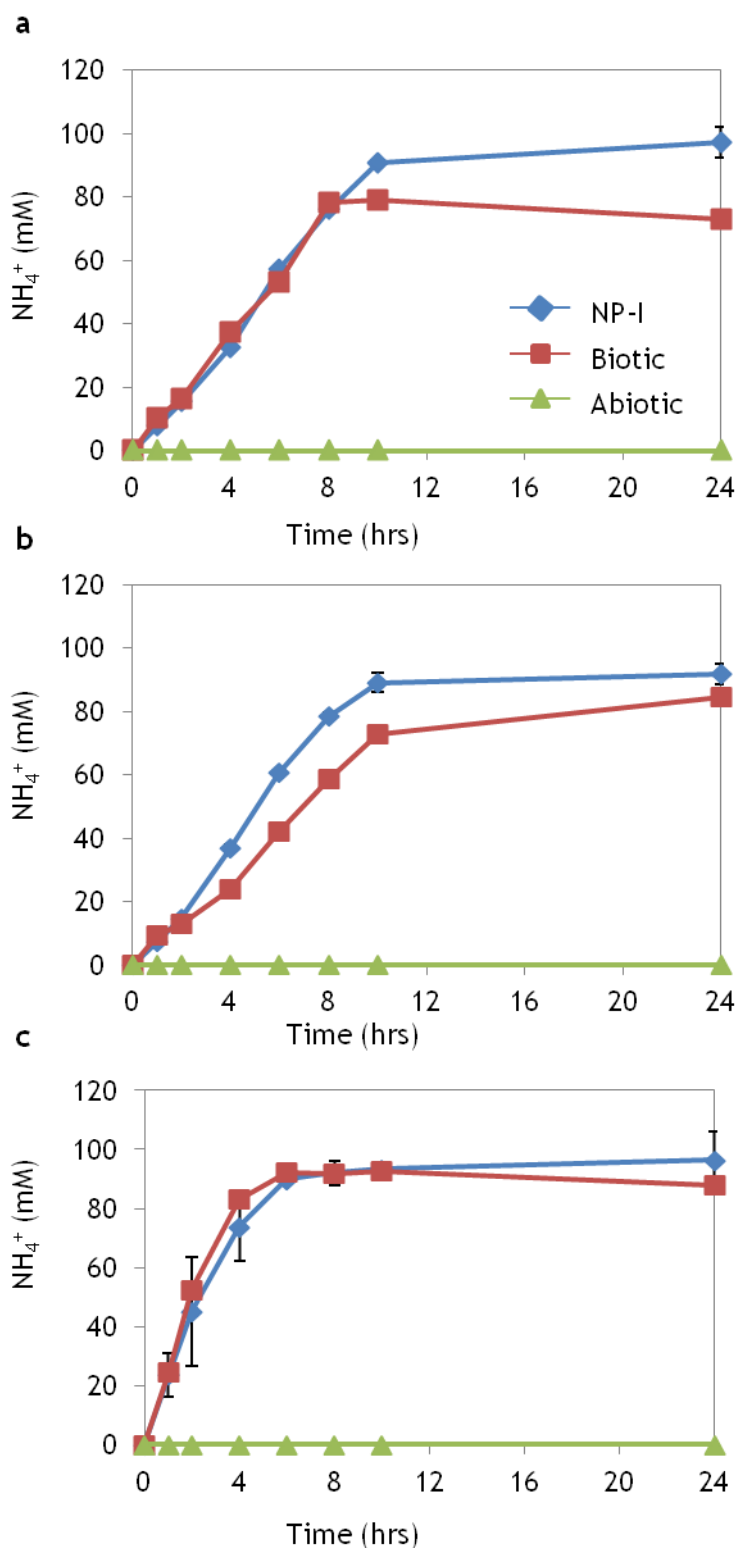


Figure 2.1: Time series showing changes in NH_4^+ . Graph (a) shows changes for the for the s-negNP, (b) s-posNP and (c) I-negNP. “NP-I”, “biotic” and “Abiotic” refer to the nanoparticle immobilization experiment and the biotic and abiotic control respectively. Each data point represents the average of triplicate experiments with associated standard deviation ($\sigma = 1$, shown as error bars).

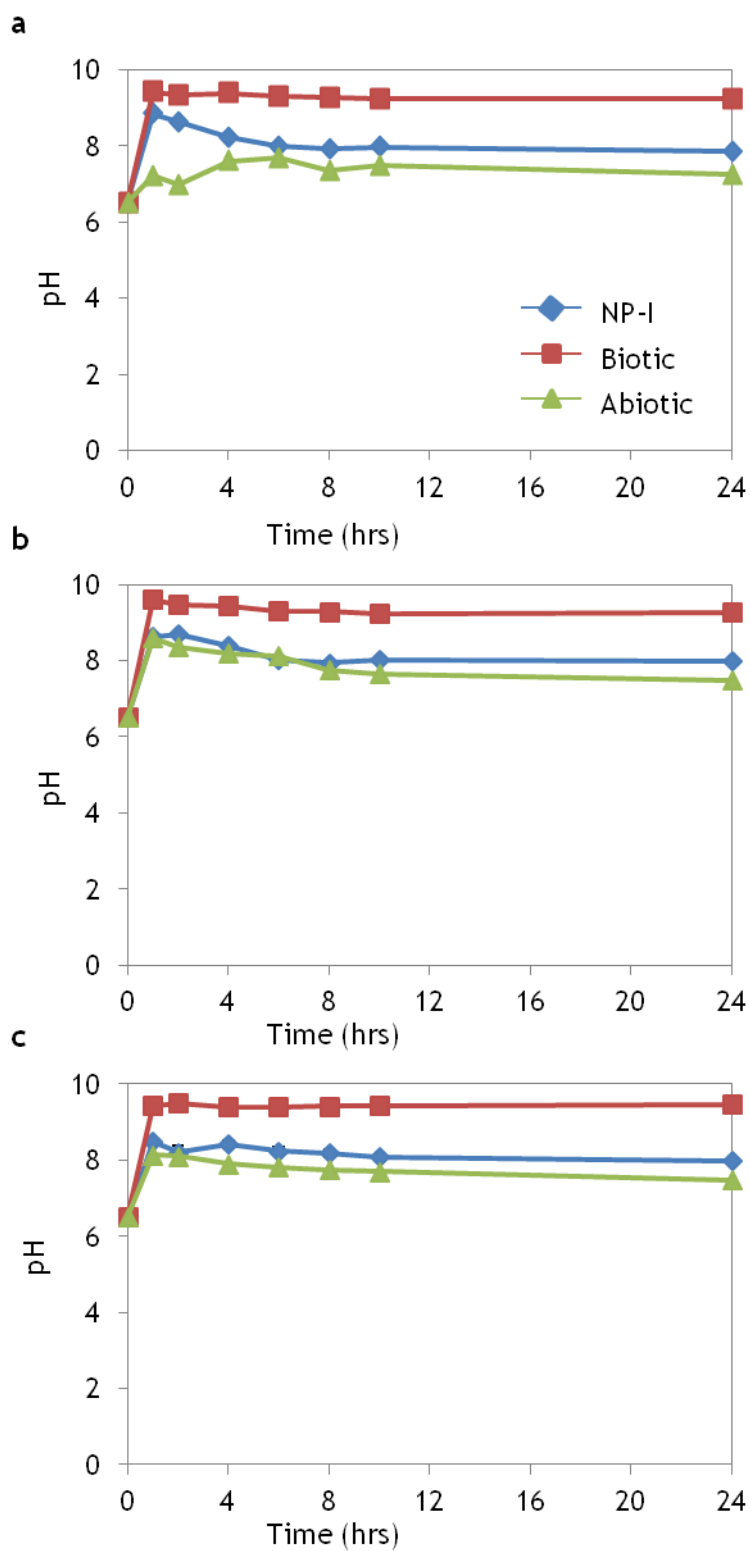


Figure 2.2: Time series showing changes in pH for the for the (a) s-negNP, (b) s-posNP and (c) l-negNP. Each data point represents the average of triplicate experiments with associated standard deviation ($\sigma = 1$, shown as error bars).

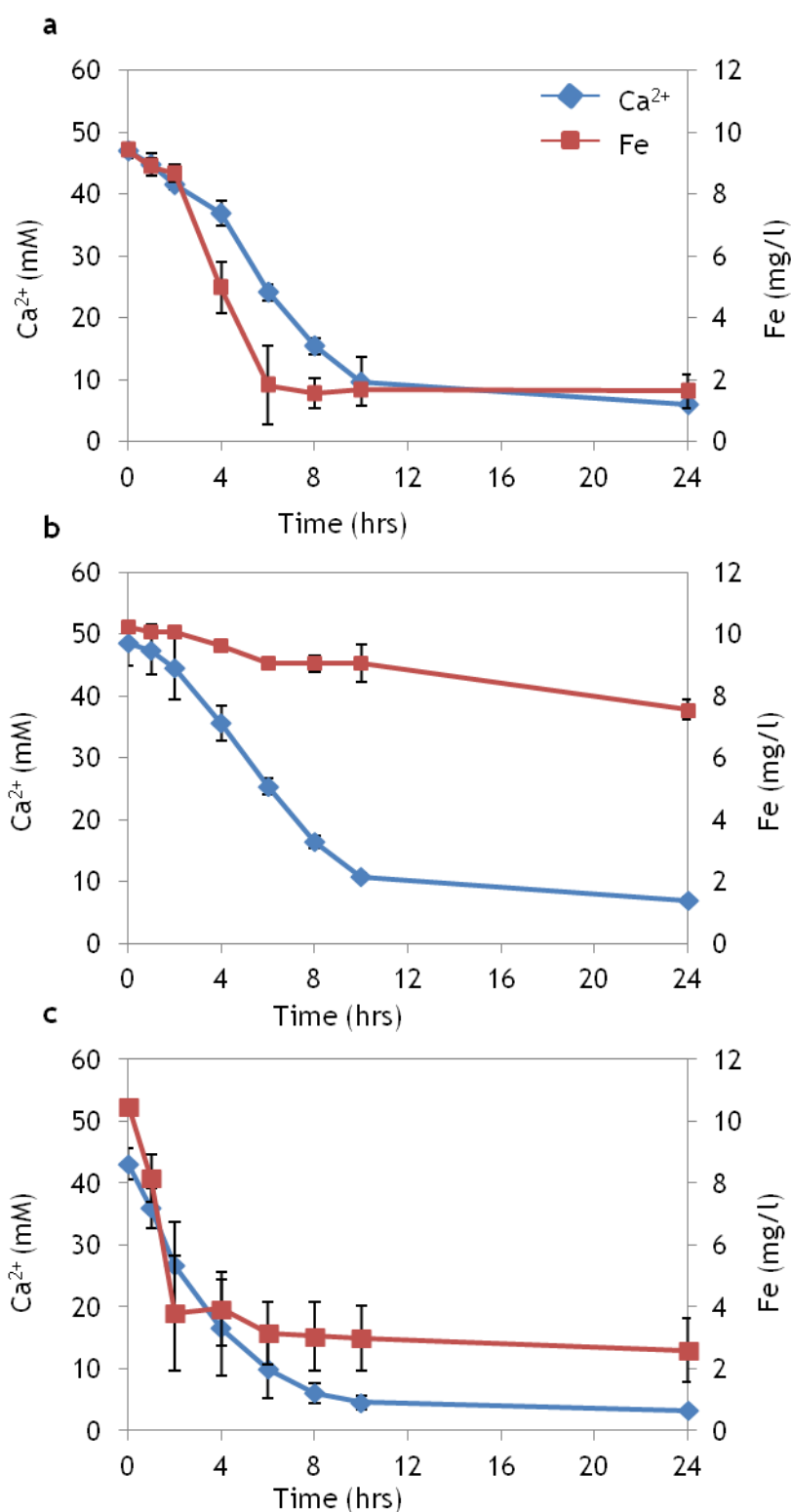


Figure 2.3: Time series showing changes in dissolved Ca²⁺ and NP concentration for nanoparticle immobilization (NP-I) experiments: (a) small, highly negative NP (s-negNP), (b) small, highly positive NP (s-posNP) and (c) large negative NP (l-negNP). Fe is used as a proxy for NP concentration in all figures. Each data point represents the average of triplicate experiments with associated standard deviation ($\sigma = 1$, shown as error bars).

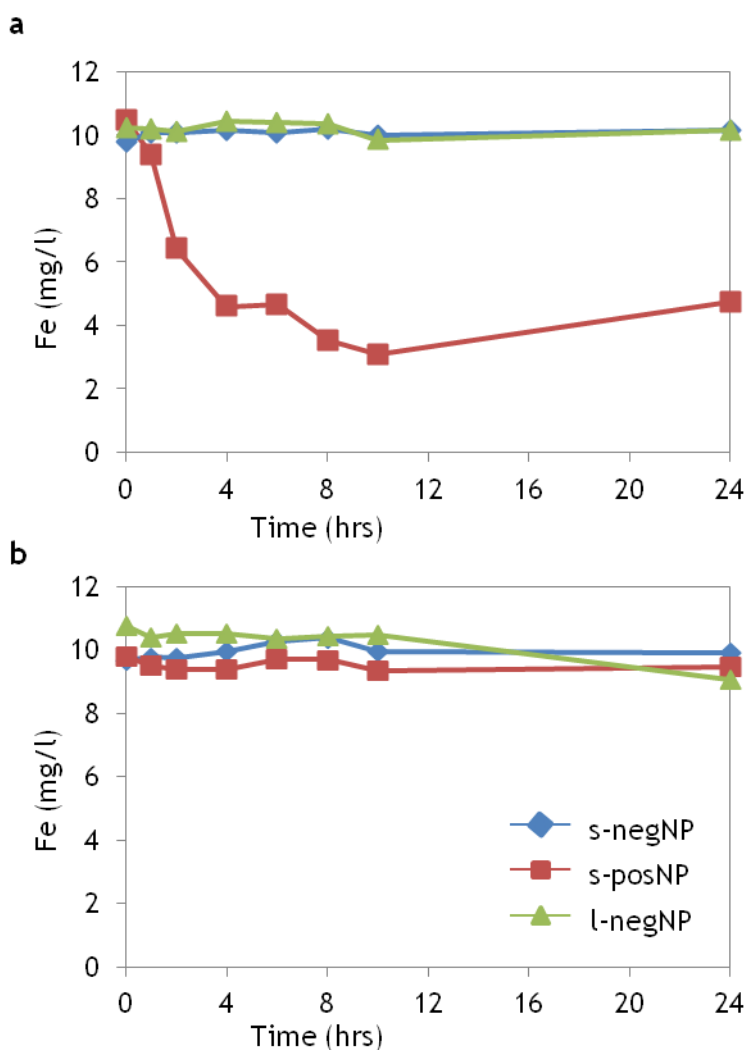


Figure 2.4: Time series showing changes in Fe (NP) concentration for the (a) biotic and (b) abiotic control for all NP types tested.

2.4.2 Immobilisation of small positively charged nanoparticles (s-posNP)

In order to compare the capture efficiency of NPs with different surface charges, s-posNPs were also tested (zeta potential: +48 mV). Apart from surface charge, these NPs were identical to the s-negNPs discussed above. In these experiments, rates of urea hydrolysis, pH increase and removal of dissolved Ca^{2+} (as a result of calcite precipitation) were almost identical to those observed for the s-negNP experiment (Figure 2.1 - 3). However, the Fe trajectory for the s-posNP remediation experiment exhibited intriguingly different results (Figure 2.4b). Poor NP capture was observed with only 26% of the s-posNPs removed compared to the removal of 83% of the s-negNPs (Figure 2.4a - b). The contrasting results of s-neg and s-pos NPs capture are further illustrated in Figure 2.5, where the % NP capture is compared against % precipitated calcium

carbonate. Here, almost 50% of the s-neg NPs were removed by the first 15% of calcium carbonate precipitation, while in the s-posNP experiment at the same time point only 5% of s-posNPs were removed within 25% of the calcium carbonate precipitate. This highlights that a higher percentage of s-negNPs are incorporated into a lower percentage of calcium carbonate. Moreover, examination of Figure 2.5 shows that s-neg NP removal appears to be more efficient during the early stages of precipitation (i.e. the first 50% of s-negNPs are captured by just 15% calcite precipitation, whilst the next 33% of NPs to be captured require ~35% calcite precipitation).

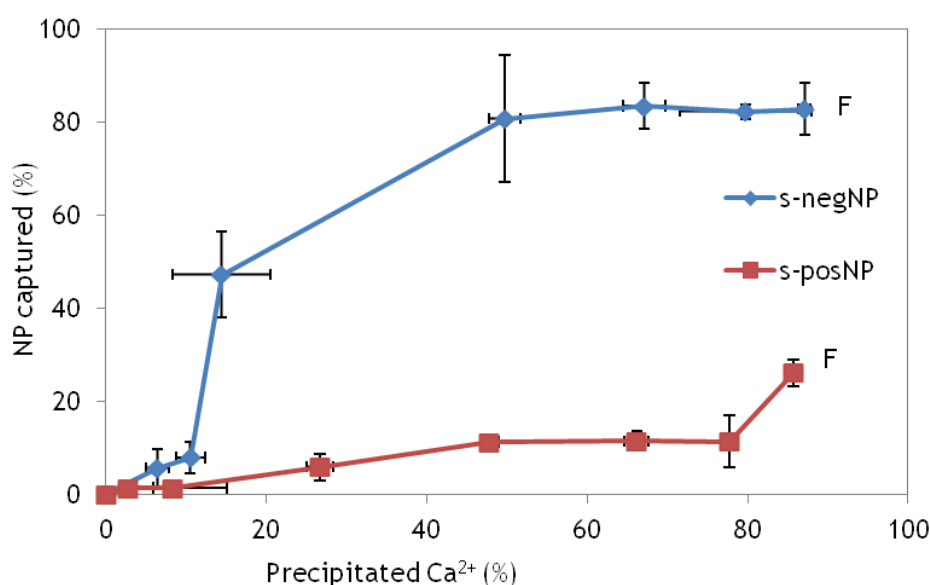


Figure 2.5: Percentage of precipitated Ca²⁺ compared to % NP captured from solution for s-neg and s-posNPs. In terms of chronological order of data points, the origin of the graph corresponds to time zero, and the finish of each experiment is labelled F. Each data point represents the average of triplicate experiments with associated standard deviation ($\sigma = 1$, shown as error bars).

2.4.3 Immobilisation of large negatively charged nanoparticles

This approach was then tested on a third NP type, again with an organic capped nanomagnetite core (also 10 nm), but with a larger total diameter (50-150 nm, just above the nano range of 1-100nm) and slightly less negative surface charge (zeta potential -30.8 mV). This large negative nanoparticle is referred to as l-negNP. Again, ureolysis, pH and Ca²⁺ removal rates were very similar to trends observed for the small, highly positive and negative NP remediation experiments (Figure 2.1 - 3). Over 90% of dissolved Ca²⁺ was removed within 10

hours capturing 75% of the l-negNPs (Figure 2.3c), which was 8% less than for the s-negNP experiment. As shown in Figure 2.4a and c, a large percentage of negative NPs were captured with a small percentage remaining in solution. Following this, another experiment was devised to determine whether the remaining l-neg NPs in solution could be captured if the system was re-doped with CaCl_2 and urea to stimulate further calcium carbonate precipitation. Figure 2.6 shows that with a second injection of CaCl_2 and urea (yielding final concentrations of 50 mM each), further calcium carbonate precipitation occurred thereby capturing the remaining suspended NPs by solid phase capture. Notably, this suggests that 100% NP removal may be achieved with repeated injections of CaCl_2 and urea.

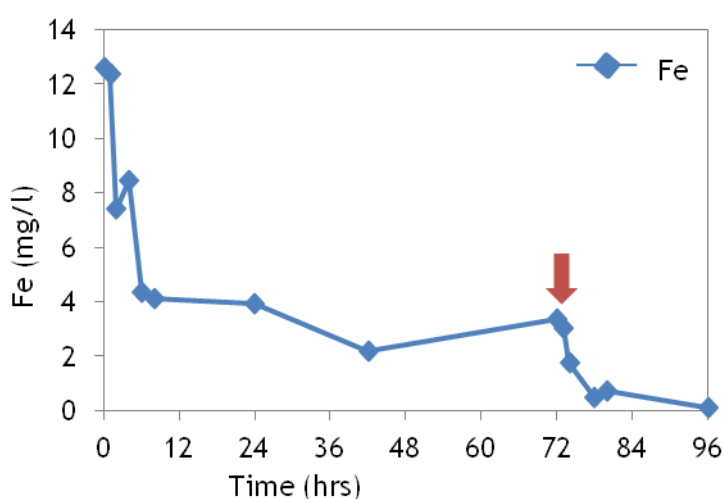


Figure 2.6: Time series showing Fe (NP) concentration during the double dose experiment for the l-negNP. The red arrow highlights when the second dose of CaCl_2 and urea was injected.

2.5 Mineral analysis by Transmission Electron Microscopy (TEM)

Calcium carbonate precipitated in the NP-I experiments adhered to the walls of the glass beakers and any surfaces within them (such as glass slides to capture precipitates for SEM and TEM analysis). With negative NPs precipitates formed were brown-orange in colour due to the incorporation of the red coloured NPs (Figure 2.7a). In contrast, calcite precipitated by the same method but in the absence of NPs produced a near-white precipitate (Figure

2.7b). SEM analyses showed that calcite was the dominant mineral phase in all experiments as indicated by the rhombohedral morphology of the crystals (Figure 2.8). Figure 2.8a shows bacterial cells part embedded within the calcite; the bacteria becoming embedded within the calcite as they drive the reaction forward. Despite the presence of bacteria within the crystal, they have not altered the crystal's shape. TEM images of thin foils cut from single crystals of calcite confirmed that the NPs occurred as inclusions (Figure 2.8b); the crystal lattice is distorted around them producing strain contrast in bright-field images (Figure 2.8c). Figure 2.9a shows the area used for the analysis and indicates the line scan taken across this area. Figure 2.9b shows spectra from the calcite and from the NPs: the calcite spectra, unsurprisingly, show edges for carbon, calcium and oxygen; the NP spectra, on the other hand, show reduced levels of carbon and calcium, but a clear extra signal of iron, which is consistent with them being an iron oxide. No quantitative evaluation of the chemistry was attempted, since, even under very fast acquisition (0.02 s per spectrum) and low accelerating voltage, the sample was damaged during the acquisition and the calcite was partially decomposed under the irradiation. Nevertheless, the results shown in Figure 2.9 are a representative sample of the results shown in about 10 EELS line scans across different nanoparticle clusters. This demonstrates unambiguously that the magnetite NPs are being effectively encapsulated in the growth of calcite crystals.

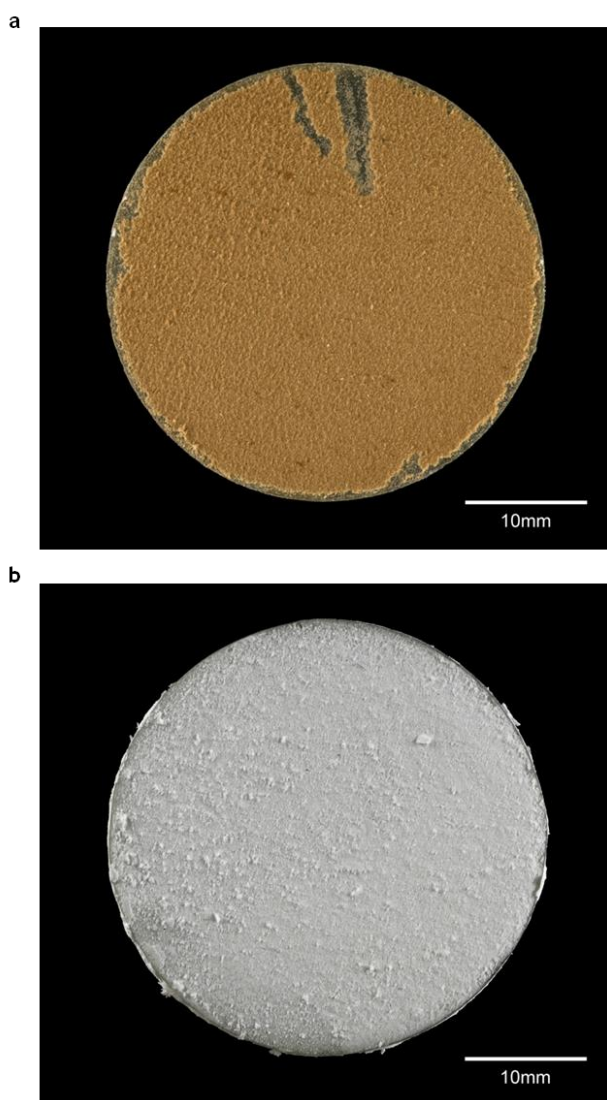


Figure 2.7: Photographs of glass slides placed at the bottom of the microcosms showing (a) brown – orange coloured calcium carbonate precipitates in the presence of negatively charged NPs (I-negNPs in this example), and (b) white calcium carbonate precipitated in the absence of NPs and. Scale bars both 10 mm.

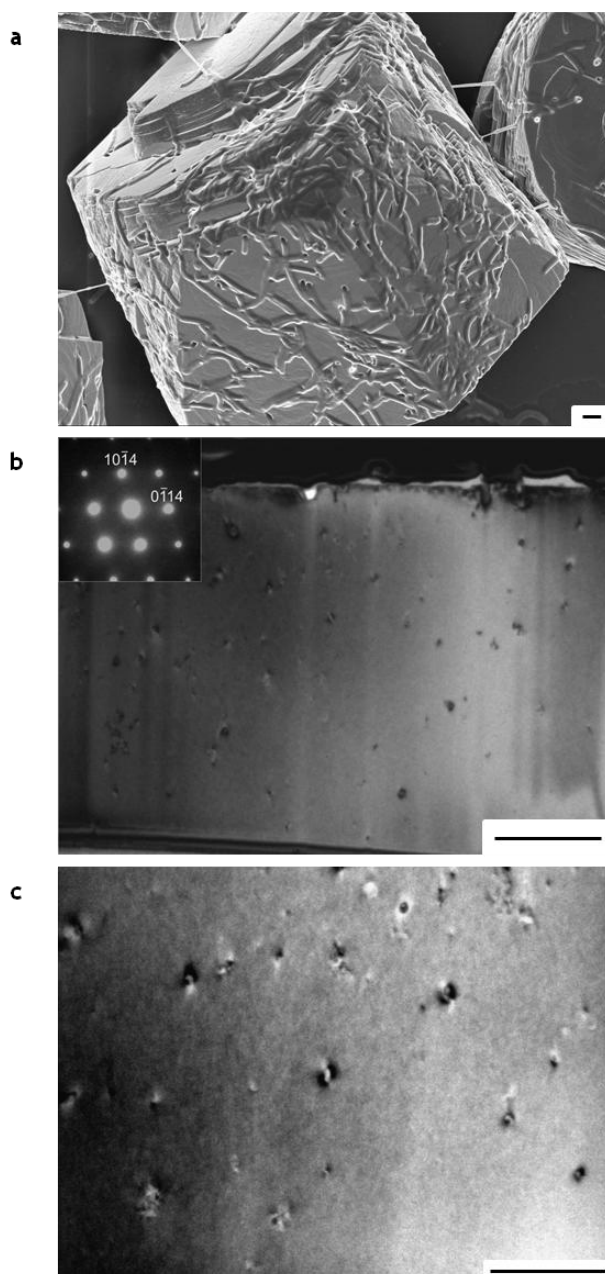


Figure 2.8: SEM and TEM images of captured NPs. (a) SEM image illustrating a typical rhombohedral calcium carbonate grain precipitated in the presence of NPs with *S. pasteurii* attached to its surface. Scale bar 2 μm (b, c) Bright-field TEM images of foils milled from a bacterially precipitated calcium carbonate crystal using the focused ion beam FIB technique. Sample is from the I-negNP experiment. Image b was obtained with the crystal oriented close to its $[\bar{4}401]$ zone axis and the indexed selected area electron diffraction pattern is inset. Under these imaging conditions the local elastic strain induced in the calcite crystal structure by the NP inclusions is highlighted by small areas of high contrast, giving the crystal a ‘speckled’ appearance. The black band along the top edge of the image is the platinum strap that was deposited on the $\{10\bar{1}4\}$ parallel crystal surface prior to FIB milling, and the vertical streaks are ion milling artifacts. Scale bar 1 μm. (c) Higher magnification of the interior of a calcite crystal in the same crystallographic orientation as in b highlighting the ‘butterfly’-like areas of strain contrast surrounding the NPs. Scale bar 500 nm. Analysis of these inclusions by Electron Energy Loss Spectroscopy (EELS) has confirmed that Fe is present in the NP inclusions but is absent from their calcite matrix (Figure 2.9).

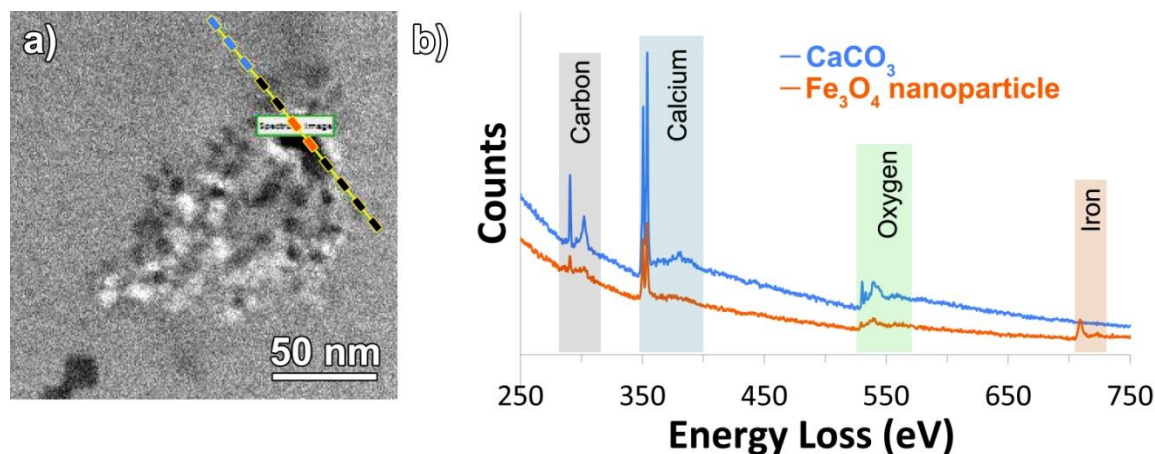


Figure 2.9: (a) STEM image of an area of calcite crystal containing a cluster of NPs (black dots).

An EELS line scan was taken along the line indicated; (b) two EELS spectra calculated from the data in the line scan, the blue spectrum comes from summing the spectra for the blue part of the line scan indicated in (a) in the calcite, the orange spectrum comes from summing the spectra in the orange part of the line scan indicated in (a) in the NP region.

2.6 Discussion

In this study, NPs with a negative surface charge (s-neg NPs and l-neg) were successfully captured, whilst the immobilisation of positively charged NPs (s-posNP) was less effective. Unlike solid-phase capture of dissolved ions such as Sr^{90} , NPs will not be incorporated into the crystal lattice by isomorphic replacement of calcium. Instead, NPs must be smothered and trapped within the mineral as it precipitates, immobilising the NP within the precipitate.

The large variations in capture efficiency between the positive and negative NPs may be attributed to electrostatic interactions controlling either nucleation, nanoparticle occlusion, or indeed both. The immobilisation of negative NPs is extremely efficient. This could, for example, be due to Ca^{2+} ions binding to their charged surfaces. The bound Ca^{2+} could then react with carbonate anions, facilitating calcium carbonate nucleation upon the NP. The negative NPs would therefore facilitate nucleation of mineral phases by providing preferential nucleation sites which act to lower the activation energy for nucleation. However, the calculated critical saturation (S_{crit}) required for calcite nucleation yielded similar values for all NP types tested (Table 2.2). If NPs were acting as nucleation sites it would be expected that S_{crit} values for the s-neg and l-negNPs would be lower than for the s-posNPs. This, however, was not observed. Certainly, where fits (R^2 values) are better than 0.9, S_{crit} values are similar and considering the spread of values (note that some of the spread of S_{crit}

values is due to poorer fits), no significant evidence of NP type impacting S_{crit} is evident using this approach. Instead, it is suggested here that due to the oversaturation of calcium carbonate under these experimental conditions (high pH and excess of Ca^{2+} and CO_3^{2-} ions), it is likely that homogenous nucleation (i.e., nucleation without a surface catalyst) was the predominant route for calcium carbonate nucleation to occur.

Table 2.2: Summary of kinetic parameters.
For calcite precipitation rate constant (k_p , in $mM\ d^{-1}$) and critical saturation state at which calcite precipitates (S_{crit})

NP	Exp	k_p (R^2 values)	S_{crit} (R^2 values)
s-negNP	1	0.11 (0.93)	2.02 (0.93)
s-negNP	2	0.02 (0.66)	2.17 (0.66)
s-negNP	3	0.09 (0.73)	2.21 (0.73)
s-posNP	1	- ^a	- ^a
s-posNP	2	0.09 (0.96)	2.12 (0.96)
s-posNP	3	0.04 (0.81)	2.25 (0.81)
l-negNP	1	0.12 (0.92)	2.11 (0.92)
l-negNP	2	0.02 (0.55)	2.45 (0.55)
l-negNP	3	- ^a	- ^a

^a Parameter estimation failed

As nucleation of calcium carbonate upon NPs does not appear to be key to the capture process, then NP capture is likely dominated by NP attachment onto growing calcite surfaces; the NP eventually becoming overtaken by the growing solidification front and thus occluded. This process has been explored in non-biologically driven encapsulation of foreign particles, motivated by the desire to develop novel composite materials and control mineral growth (Kim et al., 2010b, Lu et al., 2005). The successful incorporation of a foreign particle is determined by the interactions which occur between a particle and the

advancing solidification front (Asthana and Tewari, 1993, Rempel and Worster, 1999). These interactions determine whether a particle becomes occluded by the solid or whether it is pushed ahead of the solid-liquid interface and thus remains untrapped. At the pH range in this study, calcite exhibits a positive surface charge (Eriksson et al., 2007). Here, electrostatic attraction between the negative nanoparticle and positive calcite surface would facilitate occlusion, while electrostatic repulsion between positive NP and positive calcite surface would inhibit occlusion. The finding here that negative NPs were captured with greater efficiency is consistent with previous studies that have examined occlusion of functionalised latex colloids (220 - 250 nm in diameter) into non-biogenically precipitated calcite (Kim et al., 2010b). Their work reported greater incorporation of particles with higher abundances of anionic surface groups. In addition to electrostatic interactions, viscous drag (generated by the particle being pushed ahead of the solidification front) and van der Waals forces play an important role in mediating occlusion. Viscous drag on the particle and attractive van der Waals forces facilitate particle entrapment, while repulsive van der Waals forces inhibit entrapment (Kim et al., 2010b). In the case of the negatively charged NPs in this study, electrostatic attraction combined with viscous drag must have dominated over repulsive forces to facilitate occlusion of negatively charged NPs. Conversely, the dominance of electrostatic repulsion ensured the positive NPs were incorporated less effectively. Any removal of positively charged NPs must be attributed to viscous drag and attractive van der Waals forces.

The potential for NP attachment to calcite precipitates can be evaluated using the classical Derjaguin-Landau-Verwey-Overbeek (DLVO) model. The total interaction (V_{total}) between two charged surfaces can be described as the sum of the van der Waals (V_{vdW}) and electrostatic energy (V_{elec}):

$$V_{total} = V_{vdW} + V_{elec}$$

The equations presented here assume that the NP is a sphere of dextran as opposed to magnetite because the 10 nm magnetite core is surrounded by a 25 nm thick layer of dextran, thus surface interactions will be between calcite and dextran. Moreover, the carboxyl and amine functional groups which impart the nanoparticle charge are on the dextran, not the magnetite. The system modelled here is represented by the Lifshitz-van der Waals attraction energy for

a sphere - plate interaction with the NP assigned as a sphere and calcite precipitate the flat plate as the NP is infinitely smaller than the calcite precipitate. The Debye length (k^{-1}) is inversely related to the thickness of the diffuse double layer and was calculated using the equation adapted from (Bradford and Torkzaban, 2008):

$$k^{-1} = \sqrt{\frac{\varepsilon\varepsilon_0 k_B T}{2N_A e^2 I}}$$

here ε_0 is the permittivity of free space (8.854×10^{-12} F/m), ε is the dielectric constant of water (78.5), k_B is the Boltzmann constant, T is the temperature (298 K), N_A is the Avogadro's number, e is the electronic charge (1.6×10^{-23} C), and I is the ionic strength of the medium (as the ionic strength of the medium changed throughout the duration of the experiment, only the starting ionic strength was calculated as 150 M/m^3).

The sum of the interaction energies is described below as documented by (Hong et al., 2009):

$$\phi_{el} = \pi\varepsilon_0\varepsilon r_p \left\{ 2\varphi_p\varphi_c \ln \left[\frac{1+\exp(-kh)}{1-\exp(-kh)} \right] + (\varphi_p^2 + \varphi_c^2) \ln[1 - \exp(-2kh)] \right\}$$

$$\phi_{vdv} = -\frac{A_{132}r_p}{6h} \left[1 + \frac{14h}{\lambda} \right]^{-1}$$

where r_p is the NP radius, φ_p and φ_c are the zeta potentials of the NP and calcite precipitates respectively and λ is the characteristic wavelength of the medium (100 nm). A_{132} denotes the Hamaker constant for the system described as follows:

$$A_{132} = (\sqrt{A_{11}} - \sqrt{A_{33}}) \times (\sqrt{A_{22}} - \sqrt{A_{33}})$$

where A_{11} is the Hamaker constant of NPs, A_{22} is the Hamaker constant for calcite and A_{33} is the Hamaker constant for water. All tested parameters can be seen in

Table 2.3.

Table 2.3: Summary of the parameters for used in DLVO equations

Parameter	Unit	Value	Reference
S-neg/pos NP radius (r_p)	m	1.75×10^{-8}	Manufacturers guidelines (Biopal, Inc.™)
L-negNP radius (r_p)	m	5.25×10^{-8}	Manufacturers guidelines (Biopal, Inc.™)
S-negNP zeta potential	V	-0.038	Manufacturers guidelines (Biopal, Inc.™)
S-posNP zeta potential	V	0.048	Manufacturers guidelines (Biopal, Inc.™)
S-negNP zeta potential	V	-0.030	Manufacturers guidelines (Biopal, Inc.™)
Calcite zeta potential	V	0.04	(Eriksson et al., 2007)
Ionic strength	M/m ³	150	Calculated
Debye length (k)	m ⁻¹	7.93×10^{-10}	Calculated
Hamaker constant of NPs (A_{11})	J	1.8×10^{-19}	(Hu et al., 2010)
Hamaker constant of calcite (A_{22})	J	8.02×10^{-20}	(Tufenkji and Elimelech, 2003)
Hamaker constant of water	J	3.07×10^{-20}	(Tufenkji and Elimelech, 2003)

(A_{33})			
Combined Hamaker constant for NPs, calcite and water	J	2.11×10^{-20}	Calculated
(A_{132})			

Figure 2.10 displays attractive interaction energies between s-negNPs and positively charged calcite surfaces. Electric double layer, Van der Waals and total interactions are attractive. Here no energy barrier exists implying that NPs are strongly and irreversibly attached to the calcite mineral, being deposited in the primary energy well (no secondary energy well exists). DLVO theory confirms that electrostatic attraction and Van de Waals attraction irreversibly attaches negatively charged NPs onto growing calcite surfaces where by they become engulfed by the advancing solidification front, embedding negatively charged NPs within the mineral matrix. In contrast, Figure 2.11 displays interaction energies between s-posNPs and calcite. Here, van der Waals interactions are again attractive but electrical double layer interactions are repulsive. The combination of double layer and Van der Waals interactions serves to generate a weak attractive secondary energy minima centred at approximately 4 nm with a repulsive energy barrier centred around 2 nm. The primary energy minima then occurs below 1 nm. Strong irreversible deposition of s-posNPs to calcite surfaces may be less likely here as an energy barrier has to be overcome in order for deposition to take place in the primary energy well (Figure 2.11). Despite this some s-posNP removal did occur (Figure 2.4b). Figure 2.11 suggests that attractive van der Waals forces may be responsible for the removal of positively charged NPs. Here attractive van der Waals forces briefly dominate over electrostatic repulsion, allowing for the reversible deposition of NPs within the secondary energy minima. Once deposited in the secondary energy well the s-posNPs may become engulfed within the mineral precipitate, permanently immobilising positively charged NPs within the mineral, resulting in the removal of 26% positively charged NPs compared to 83% when the total interaction energy is attractive (Figure 2.4, Figure 2.10 and Figure 2.11).

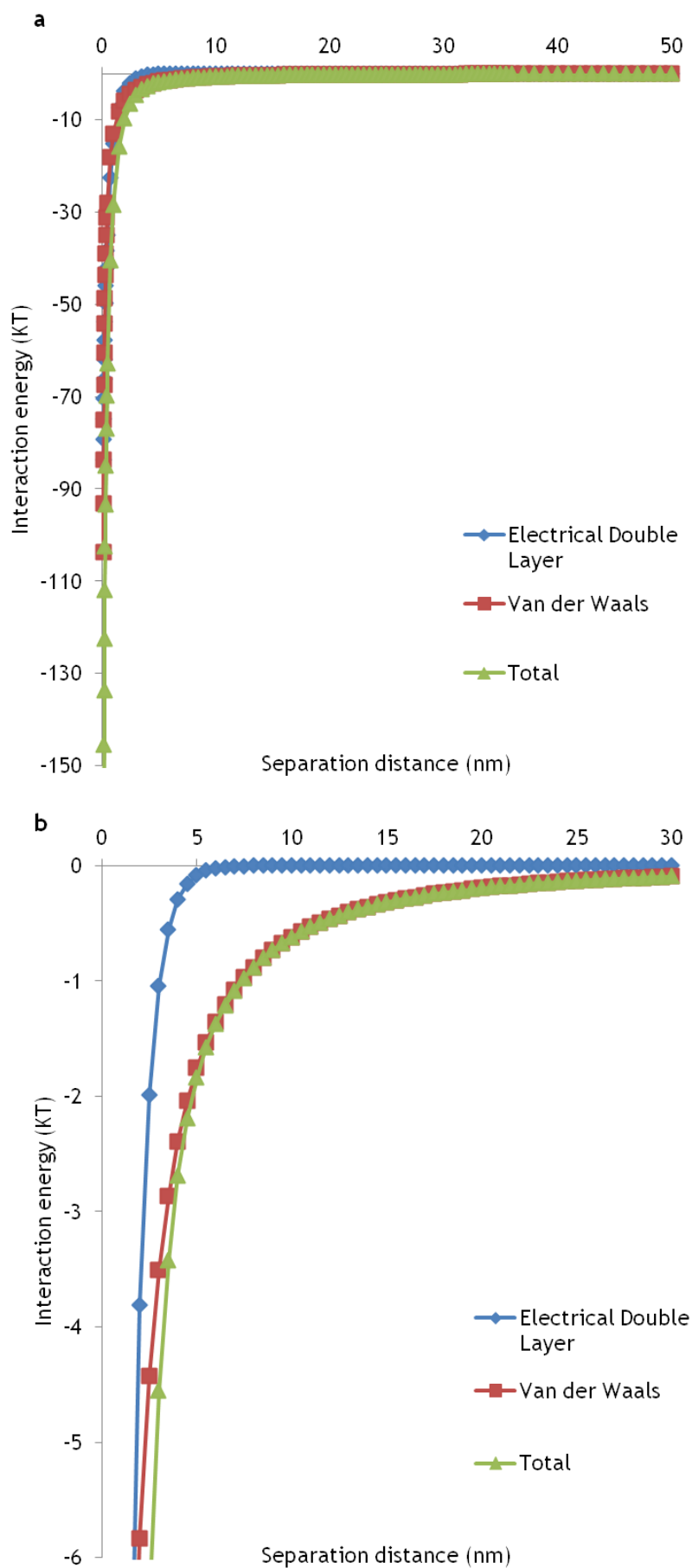


Figure 2.10: Interaction energy profile which displays the attractive force which exists between the s-negNP and the positive calcite surface. Note (b) is an enlargement of graph (a).

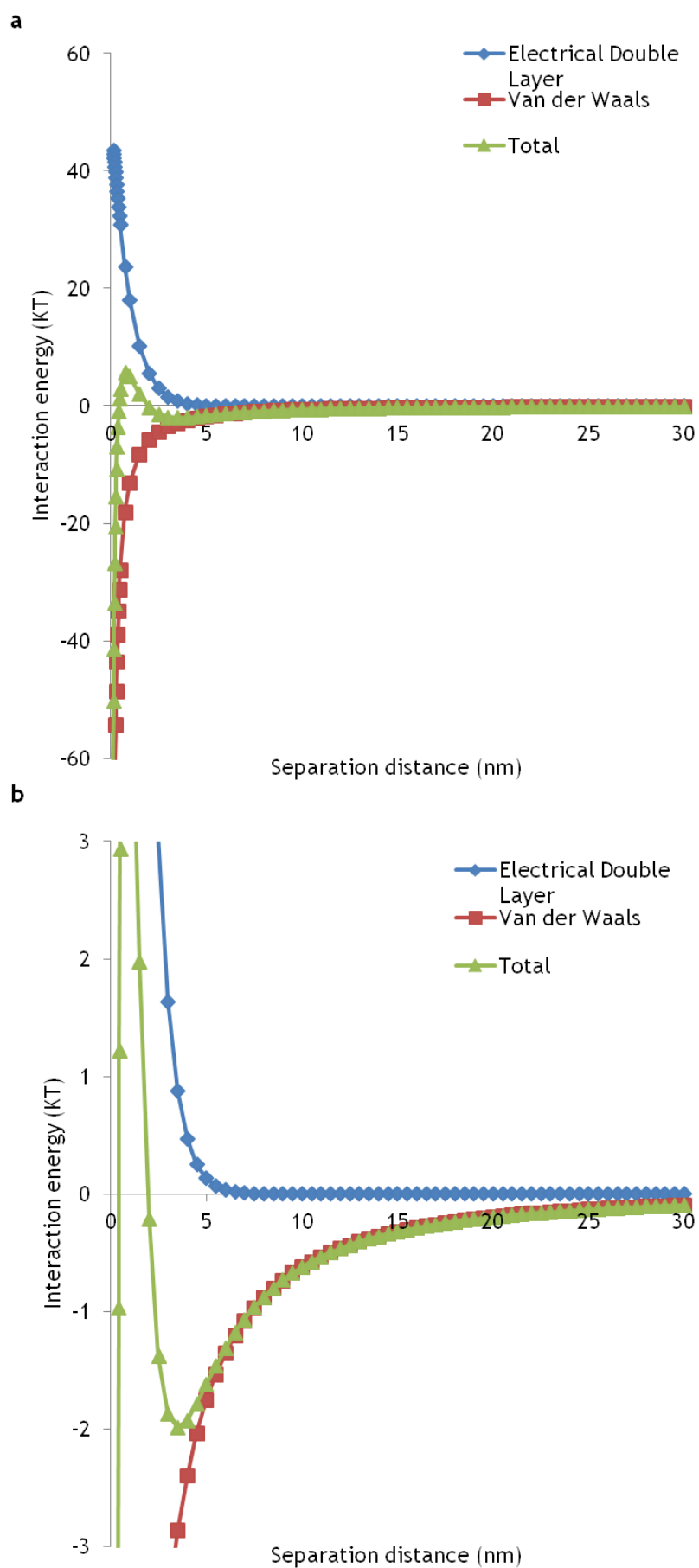


Figure 2.11: Interaction energy profiles for the attachment of s-posNPs to positively charged calcite surfaces.
Note (b) is an enlargement of graph (a).

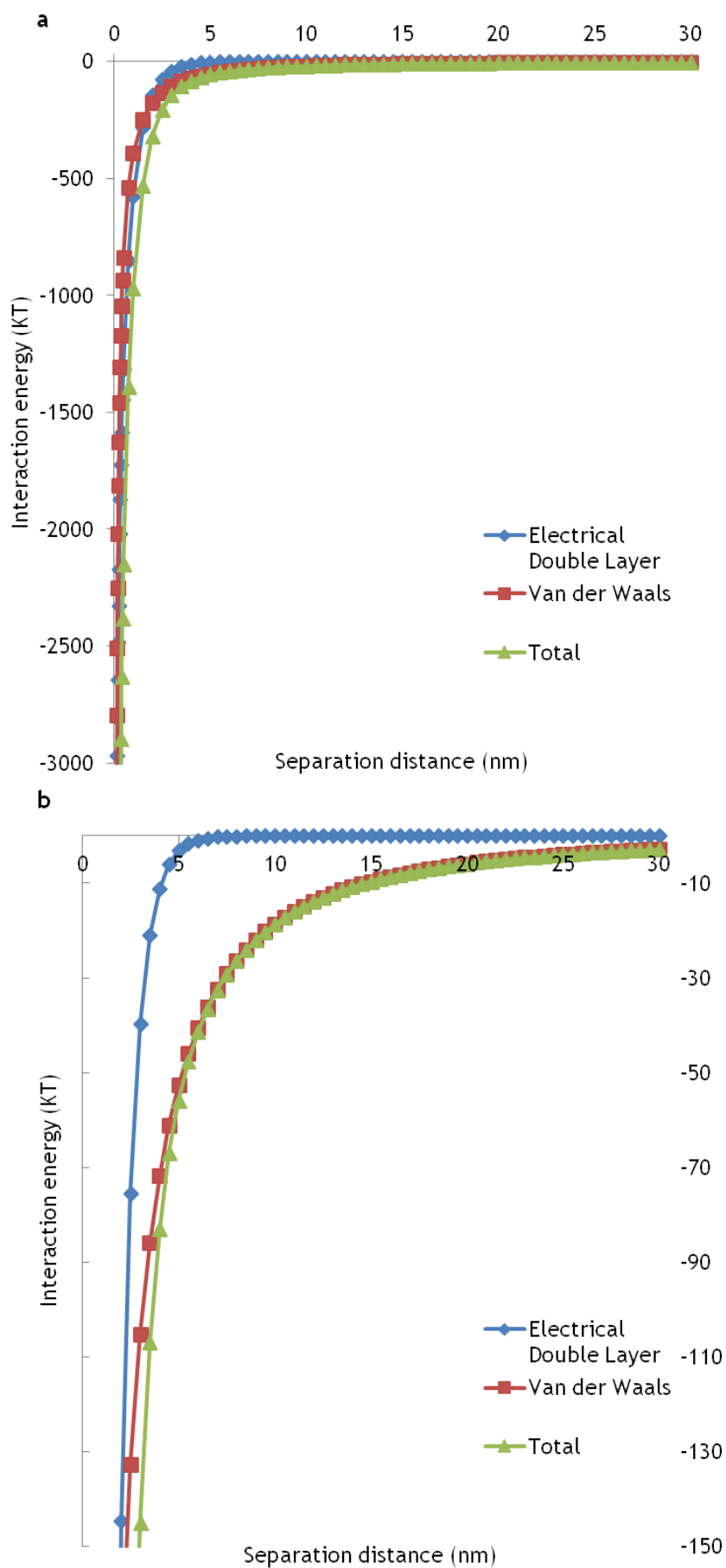


Figure 2.12: Interaction energy profiles for the attachment of I-negNPs to positively charged calcite surfaces.

Note (b) is an enlargement of graph (a).

In this study, the l-negNP was incorporated marginally less effectively than the s-negNP. 75% of the l-negNPs were removed through solid phase capture versus 83% for the s-negNP (Figure 2.4a and c). This difference may be due to the smaller negative charge on the l-negNP (-30.8 mV) compared to the s-negNP (-38 mV). However, according to the DLVO model presented here, (Figure 2.12) does not agree with the observed findings. Instead, attraction between the l-negNPs and the positive calcite surface is stronger under these conditions, with attraction occurring from as far as 25-30 nm separation distance compared to 5-10 nm for the s-negNP. This combined with greater viscous drag acting on the larger NP which acts to facilitate occlusion fails to account for why fewer l-negNPs were incorporated compared to s-negNPs. Some other unknown mechanism must be operating here.

Despite the greater occlusion of negative NPs into calcite compared to positive NPs, this did not appear to have a notable impact on k_p , the calcite precipitation rate constant. Considering only those with fits (R^2 values) better than 0.9, the k_p values are broadly similar between NP types (Table 2.2). This is consistent with the lack of notable difference in S_{crit} . Again, it would appear calcite supersaturation is sufficiently high enough to drive precipitation uninfluenced by NP presence.

In this study, k_p and S_{crit} which describe CaCO_3 precipitation show little or no dependence on NP type. While this must be explored at higher NP concentrations and for other NP types, the relative invariability between systems could make implementation in the field simpler. Calcite precipitation would be independent of NP type and therefore easier to predict.

The observation that s-negNPs are removed at a faster rate during the early stages of calcium carbonate precipitation (Figure 2.5) may be explained by invoking a shift from homogeneous to heterogeneous nucleation during the experiment. During the early stages, calcite nuclei are forming homogeneously and consequently growing in suspension. It is during this early stage of crystallisation that most NPs are being removed. However, during the later stages of the experiment, the saturation state with respect to calcite is greatly reduced (due to calcite precipitation) and thus precipitation may occur preferentially on pre-formed precipitates, i.e. those crystals that have already settled to the bottom of the reaction flask or adhered to its walls. Thus

homogenous nucleation and growth in suspension is greatly reduced, leaving uncaptured NPs in solution. At this point a reinjection of calcium carbonate and urea is required allowing for further calcite precipitation to occur homogeneously in suspension. Figure 2.6 shows that stimulating another homogeneous nucleation event results in 100% removal of l-negNPs through solid phase capture. If this hypothesis is correct, it has implications for possible in-field application of this method, i.e. NP immobilisation would be improved by multiple injections.

Ureolytic bacteria such as *S. pasteurii* have been proposed as being suitable for a number of subsurface applications. The urease enzyme (urea amidohydrolase) can be produced by many groundwater bacteria and as a consequence the natural indigenous community may be manipulated for such applications (Tobler et al., 2011). However, where bacterial communities are not sufficiently active to produce the rates of ureolysis required to precipitate sufficient volumes of calcite, the indigenous ureolytic community may be stimulated by a carbon source to increase biomass and encourage ureolysis. Such an option has been explored for the solid-phase capture of ^{90}Sr from contaminated aquifers (Fujita et al., 2008). Alternatively, an ex-situ cultured ureolytic bacterium such as *S. pasteurii* may be injected into the site of interest (Cuthbert et al., 2012, Tobler et al., 2011).

Notably, biotic and abiotic controls all remained stable, with regards to NP removal, except for the biotic control of the s-posNP (Figure 2.4). In those control experiments where no NP removal occurs, NPs are free from aggregation and do not adhere to the bacterial surface. Whilst in the biotic control of the s-posNP, despite the lack of calcite precipitation (due to the absence of Ca^{2+}), rapid loss of NPs occurred with over 60% being removed within 12 hours. The cell surface of *S. pasteurii* and almost all bacteria is negatively charged over the pH range of these experiments (Yee et al., 2004), which evidently led to a strong electrostatic attraction for positive nanoparticles. As the bacteria settled from solution they concomitantly removed s-posNPs. This process highlights the potential of bacterial surfaces to immobilize NPs in the natural environment and engineered wastewater treatment systems (Limbach et al., 2008, Brar et al., 2010). We speculate similar attachment of positive NPs did not occur in the reaction where calcite precipitation occurred due to masking of the bacterial surface, either by bound Ca^{2+} or precipitated calcite.

While this study has focused upon bacterially driven calcite precipitation, there are numerous other microbially driven mineral precipitation systems which have the potential for solid phase capture of NPs, such as the oxidation of Mn(II) (Sujith and Bharathi, 2011) and Fe(II) (Glasauer et al., 2002), or enzymatic precipitation of phosphate minerals (Schulz and Schulz, 2005). Critically, the variety of minerals that can be precipitated by bacteria display a range of surface charges at typical groundwater pHs (Harding et al., 2005, Gray et al., 1978, Glasauer et al., 2001) enabling them to interact with a wide variety of NP surface charges. Thus it may be possible to choose a remediation system to specifically target the NPs surface character.

2.7 Conclusion

The results presented here demonstrate that microbially mediated calcite precipitation successfully captured negatively charged NPs whilst positively charged NPs were captured much less successfully. DLVO theory indicated this was due to electrostatic attraction generating a strong primary energy minima between calcite and negative NPs, while electrostatic repulsion generated a weak secondary energy minima and repulsive energy barrier between calcite and positive nanoparticles. k_p and S_{crit} values were broadly similar for all NP types tested suggesting NPs were not acting as nucleation sites for calcium carbonate and that NP type did not impact precipitation rate. S.posNPs were removed from solution due to the sorption of NPs to the negative charge of the bacterial surface. Microbially mediated calcite precipitation has the potential to immobilise NPs, impacting their transport and fate in environmental systems.

3 Immobilisation of nanoparticles through porous media by calcium carbonate precipitation

3.1 Summary

Experiments presented in Chapter 2 demonstrated that microbially mediated calcium carbonate precipitation successfully removed negatively charged nanoparticles (NPs) through solid phase capture in batch reactors. Here we demonstrate the potential for microbially mediated calcium carbonate precipitation to remove negatively charged NPs in porous media. Negatively charged NPs were shown to be highly mobile through sand and glass packed columns when suspended in sterile deionised water. Inducing calcite precipitation within the columns resulted in reduced NP mobility in all porous media types tested. It is hypothesised that as ureolysis commenced, calcium carbonate precipitation occurred around the NPs, on grain boundaries and also possibly heterogeneously in solution. Continual calcite growth occluded NPs. Gravitational settling from suspension of NP-mineral composites resulted in the cementation of NPs within the column. These findings demonstrate that microbially mediated calcium carbonate precipitation may be used as a tool to reduce NP mobility in environmental systems.

3.2 Introduction

The mobility of NPs through porous media has been intensely studied due to the possibility of NP pollution in the subsurface. Research has shown that particle specific properties (e.g. size, shape, surface charge and the presence of capping agents) as well as solution chemistry (e.g. pH, ionic strength, ionic strength and natural organic content) strongly influence NP mobility through environmental systems, see Chapter 1.1.4 for further details (El Badawy et al., 2013, Petosa et al., 2010, Franchi and O'Melia, 2003). Other factors influencing NP mobility include Brownian diffusion (Dunphy Guzman et al., 2006), gravitational sedimentation and straining effects (Bradford et al., 2002). Under favourable, i.e. non-repulsive conditions, NP-NP and NP-surface interactions result in the deposition of NPs onto collector surfaces, thus significantly reducing NP mobility. Despite this, long-range transport within the subsurface is possible

(Wiesner et al., 2006). NPs are increasingly designed to exhibit enhanced stability through surface modifications such as capping agents (see chapter 1.1.4 for more details on stabilising NPs, Kvittek et al., 2008, Lecoanet et al., 2004). NPs with enhanced stability have greater potential for exposure to aquatic organisms and humans (Wiesner et al., 2006). Furthermore, NPs have the ability to bind and transport pre-existing contaminants within the subsurface, dispersing contaminants over a large area (Moore, 2006).

Much work is being done to determine the fate and transport of NPs within the environment. However, none have looked at the possibility of reducing NP mobility or indeed immobilising NPs within the subsurface. This knowledge gap requires attention as technologies which can prevent pollutant NPs from migrating through groundwater and contaminating natural and drinking water resources is required. In this study we investigate the potential for biologically induced calcite precipitation to immobilise NPs within porous media. Chapter 2 demonstrated that ureolysis driven calcite precipitation was extremely effective in immobilising negatively charged NPs in batch reactors. Here, we wish to examine the potential of ureolysis driven calcite precipitation to immobilise NPs in porous matrices thereby inhibiting further transport.

3.3 Materials and methods

3.3.1 and porous media

Here, the transport and immobilisation of negatively charged NPs (these are the s-negNPs referred to in Chapter 2) in porous matrices as a function of grain size and type was tested. Note that the positively charged NPs (as used in chapter 2) were not tested here as they are poorly captured by ureolysis driven calcite precipitation.

Four different porous media were investigated which included 3 different size fractions of glass beads (fine: 0.1-0.25 mm, medium: 0.6-1.8 mm, and coarse: 2 mm) and a quartz sand (0.1-0.4 mm). SiO₂ - based porous matrices were chosen as they exhibit negatively charged surfaces (Behrens and Grier, 2001), thus the electrostatic repulsion between the SiO₂ grains and the negatively charged NPs would enhance NP mobility through the columns, and reduce attachment to grains. The relatively high mobility of NPs in these systems

would thus enable us to detect any immobilisation by solid-phase capture. Moreover, the SiO₂ based porous matrices used here are analogous to the sands and sandstones of many aquifer systems.

Spherical glass beads (Retsch, Germany) with different grain sizes were utilised. The grain size was measured using a light-scattering particle size analyzer (Coulter LS 2300). The glass beads ranged from fine with a size range of 0.1-0.25 mm with a mean size of 0.17 mm, medium range from 0.6-1.8 mm with a mean of 1 mm and coarse beads 2 mm (too large to be measured by the particle size analyser, these were instead sieved to determine grain size). The beads were cleaned with 50 % hydrochloric acid, washed repeatedly with sterile deionised water (SDW) and oven dried at 40°C overnight. Quartz sand was obtained from Fisher Scientific with a grain size ranging from 0.1-0.4 mm, with a mean of 0.26 mm. The sand was washed thoroughly with SDW and oven dried overnight at 40°C. All porous media types exhibited a porosity of approximately 34% as determined by comparing water saturated versus dry mass.

3.3.2 Nanoparticle transport experiments

Experiments were first performed to determine the mobility of NPs within the different porous media types. 10 mg/l NPs (Fe concentration) were suspended in 10 ml of either sterile deionised water (SDW) or 50 mM CaCl₂ solution. As ionic strength impacts NP mobility, experimentally relevant ionic strength values were chosen, that is 50 mM CaCl₂ at the start of the experiment reducing to 0 mM with the completion of urea hydrolysis in the NP immobilisation (NP-I) experiments. Column experiments for each porous media type were set up vertically in 15 ml plastic tubes (diameter 2 cm, length 7.5 cm) with a sintered glass disk (100-160 µm pore size) placed at the bottom of the tube to prevent porous media from falling out. First, one pore volume (8 ml) of the NP solution was added to the empty column (with closed off inlet), followed by about 15 ml of either glass beads or quartz sand. This was left in a vertical position for 24 hours. Sterile deionised water (SDW) was then pumped through the columns for approximately half an hour at 1 ml min⁻¹, with bottom to top flow (Figure 3.1). Samples were collected from the outlet every 4 minutes for later NP analysis with atomic absorption spectroscopy (AAS). Note that in these transport experiments, the NPs were mixed in with the porous media, rather

than injected in the inlet, to more closely mimic the nanoparticle immobilisation experiments presented in Chapter 2.

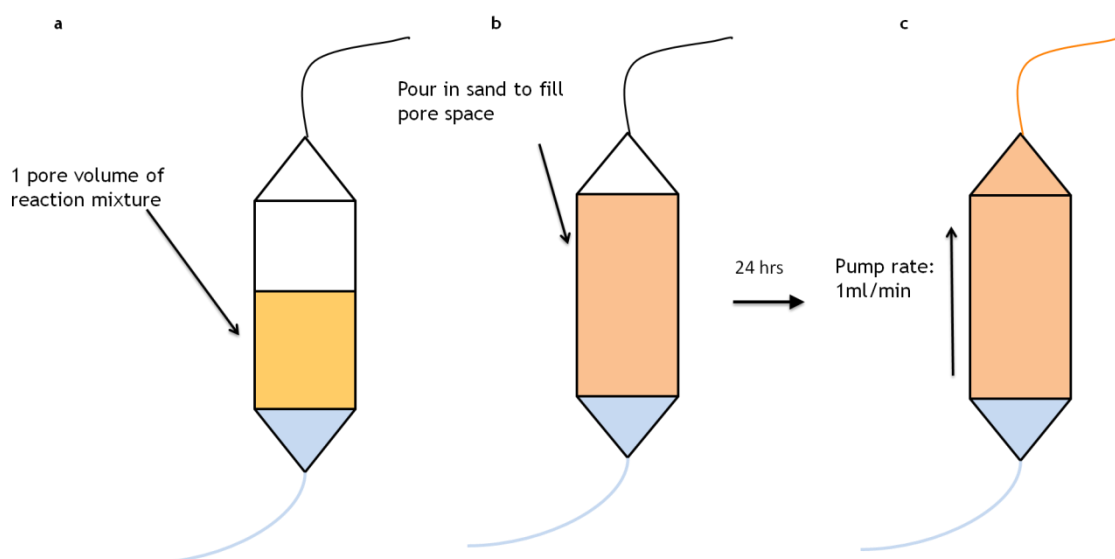


Figure 3.1: Schematic drawing of the experimental set-up for column experiments. (a) 1 pore volume (8 ml) of reaction mixture is poured into the column (diameter 2 cm, length 7.5 cm) (b) before the addition of either glass beads or quartz sand to fill the pore space. The prepared columns are left in a vertical position to react for 24 hours (c) before deionised water is pumped through the columns at a rate of 1 ml/minute with the effluent collected at the outlet for analysis

3.3.3 Nanoparticle immobilisation experiments

Experiments were performed to determine the ability of ureolytic calcite precipitation to immobilize NPs within the different porous media types. Experiments were performed using the gram positive ureolytic bacterium *Sporosarcina pasteurii* (strain ATCC 11859). Details of the bacterial preparation process can be found in Chapter 2.3.2. For each nanoparticle immobilisation (NP-I) experiment, a stock solution containing 100 mM CaCl_2 and 100 mM urea was prepared and then mixed at a ratio of 1:1 with the bacterial suspension (0.14 OD) before the addition of nanoparticles. The final concentrations were therefore 50mM CaCl_2 , 50mM urea, 10 mg/L NPs (Fe concentration) and 0.07 OD *S. pasteurii*. Biotic controls (*S. pasteurii* + urea + NP) and abiotic controls (CaCl_2 + urea + NP) were also run to ensure that NP removal was due to calcium carbonate precipitation as opposed to aggregation or deposition onto the bacterial cell and/or collector surfaces.

Column experiments were set up identically to the above described NP transport experiments (3.3.2), i.e., 8 ml (1 pore volume) of the reaction solution

was added to the empty column first and immediately followed by about 15 ml of glass bead or quartz sand (Figure 3.1). The column was left in a vertical position overnight for the reaction to complete. After 24 hours (the time taken for total urea hydrolysis to occur as determined by batch experiments, see Chapter 2.4) SDW was pumped continuously at a rate of 1 ml min^{-1} for half an hour with bottom to top flow. Samples were collected at the outlet every 4 minutes to determine concentrations of NH_4^+ (by the Nessler assay), dissolved Ca^{2+} , and Fe; the Fe used as a proxy for NP concentration (both Ca^{2+} and Fe were determined by AAS). pH was analysed at the beginning and end of all experiments.

The stock solution pH, dissolved Ca^{2+} and NP concentrations were determined before setting up the column experiments.

3.4 Results

3.4.1 Nanoparticle transport experiments

With the onset of pumping after 24 hrs, NPs were immediately detected at the outlet in all systems where NPs had been suspended in SDW (Figure 3.2a-d). Grain size and porous media type caused relatively little difference in the transport of NPs through the column for SDW suspended NPs. 100% of the NPs added were recovered at the outlet for the glass beads (all sizes) while 93 % were recovered in the quartz column (Figure 3.2a-d). The shape of the breakthrough curves indicates some retardation of NP transport; i.e. the NP concentration quickly decreased during the first 8 minutes of pumping (1 pore volume), then after 1 pore volume was flushed through there was a gradual decrease in NP concentration, approaching zero in all columns, after 16 minutes (~2 pore volumes). Without retardation, one would expect a more square or top-hat shaped breakthrough curve. In the experiments where the NPs were suspended in 50 mM CaCl_2 , notable differences in transport were observed compared to NPs suspended in SDW (Figure 3.2a-d). In glass bead systems, the percentage of NPs detected at the outlet decreased by 8-28 % compared to SDW suspended NPs, whilst a drastic decrease was observed in the quartz sand with only 18 % NPs being detected at the outlet (Figure 3.2d). NP retention followed the order of quartz sand > medium glass beads > fine glass beads > coarse glass

beads for NPs dispersed in 50 mM CaCl_2 . For all glass bead columns, NP concentrations at the outlet in general took longer to reach zero concentration (i.e. they exhibited a longer tail) in CaCl_2 suspended systems compared to SDW suspended system. This is suggestive of greater retardation in the CaCl_2 suspended system. The quartz sand exhibited an entirely different NP recovery curve. Here, no NPs were detected at the outlet with the onset of pumping. After 4 minutes of pumping NP concentration increased slightly until 8-10 minutes before gradually decreasing again.

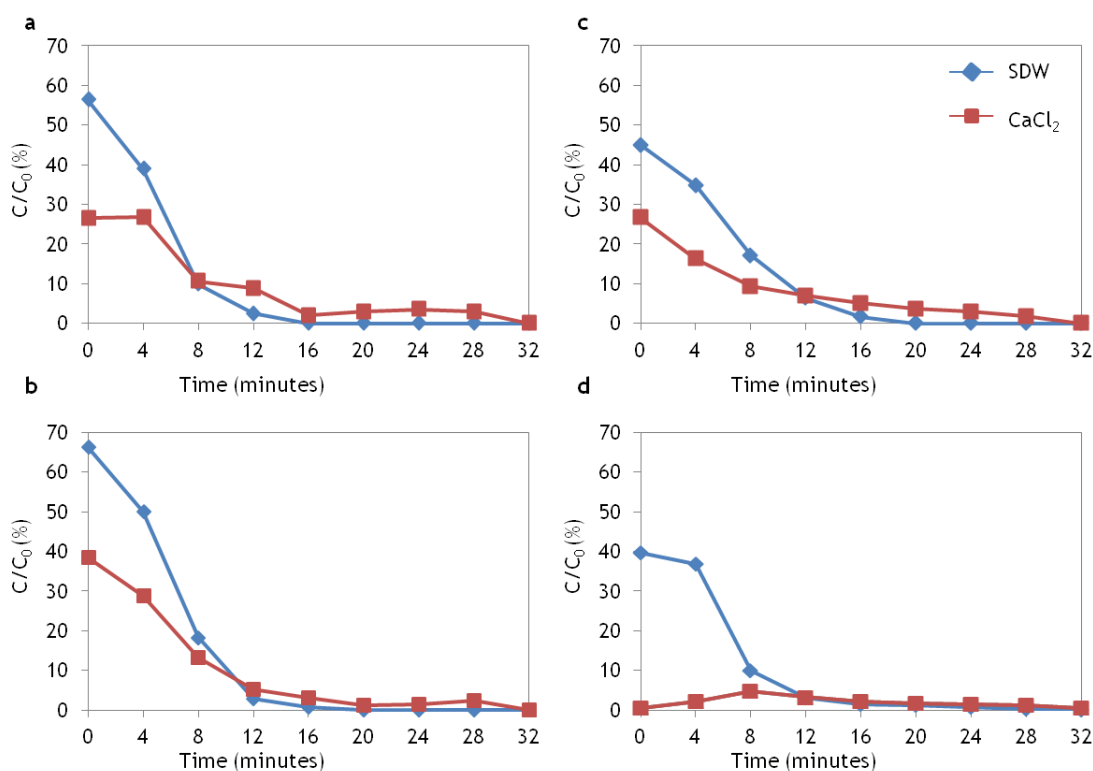


Figure 3.2: Transport of NPs suspended in SDW (diamonds) and 50 mM CaCl_2 (squares) through:
(a) fine, (b) medium, and (c) coarse glass beads and (d) quartz sand (equivalent in size to fine glass beads). (8 minutes = 1 pore volume)

3.4.1.1 Nanoparticle immobilisation through glass bead packed columns

NH_4^+ , Ca^{2+} and NP concentrations in the effluent of the glass bead packed columns allowed the progress of ureolysis, calcite precipitation and NP mobility within the columns to be monitored. After 24 hours reaction time, SDW was pumped through the columns, immediately NH_4^+ was detected in the effluents of all NP-I experiments and biotic controls (Figure 3.3). NH_4^+ recovery for the NP-I

experiment was broadly similar for all glass bead types, with 78 %, 72 % and 75 % recovery for the fine, medium and coarse grained glass beads respectively, (Figure 3.3a-c). Note, calculation of NH_4^+ recovery is based upon the assumption that all urea is hydrolysed. Therefore, the observation that less than 100 % NH_4^+ was recovered may be due to either incomplete hydrolysis of all urea and/or some NH_4^+ retained within the column). The biotic control saw similar rates of elution with 87 %, 65 % and 75 % recovery for the fine, medium and coarse grained glass beads respectively, (Figure 3.3a-c). A summary of the results for all experimental conditions can be seen in Table 3.1.

With the onset urea hydrolysis the solution became highly saturated with respect to calcium carbonate, thus inducing precipitation. Successful calcium carbonate precipitation is demonstrated by the breakthrough curves for Ca^{2+} (Figure 3.4). Ca^{2+} breakthrough curves for the abiotic controls (no calcium carbonate precipitation) follow similar profiles for all glass bead types, with Ca^{2+} breakthrough ranging from 71-76 %. However, in the NP-I experiments (where calcium carbonate precipitation occurred), Ca^{2+} breakthrough was significantly lower. The fine and medium grained glass beads showed almost identical breakthrough profiles with just 18 % and 16 % Ca^{2+} recovery respectively. However, significantly more Ca^{2+} (33 %) was detected in the effluent of the coarse grained column.

The breakthrough curves for NPs exhibit intriguingly different results, depending on solution chemistry and grain size of the porous media (Figure 3.5; Table 3.1). In each experiment NP breakthrough followed the order Biotic control > abiotic control > NP-I. The highest rates of NP mobility were observed in the biotic controls (no calcite precipitation due to absence of Ca^{2+}) for all porous media types with 71-76 % of NPs eluted. The breakthrough curves for the abiotic control exhibit greater immobilisation with 38-58 % NPs detected in the effluent. In the columns where calcium carbonate precipitation was promoted (NP-I), NP immobilisation was greatest, with just 8-31 % detected in the effluent. It is noted here that the small difference in NP breakthrough between NP-I and abiotic control in the fine bead system (31 % and 38 % respectively) cannot be considered significant due to significant error bar overlap (Figure 3.5a). However, the difference between NP-I and abiotic control in the medium and coarse system must be real (error bars do not overlap in the coarse system (Figure 3.5c) while in the medium system the abiotic control data points are

consistently higher than the NP-I with barely touching error bars (Figure 3.5b). Overall this suggests NP-I experiments do immobilize NPs more than abiotic controls.

NP transport in the NP-I experiments did not appear to be related to bead size. The medium grained porous media saw the lowest rates of NP transport, with only 8 % NPs detected in the effluent, followed by 14 % in the coarse grained media (both profiles fall within the margin of error). Whilst significantly higher rates of NP transport was observed in the fine grained media with 31 % NPs eluted.

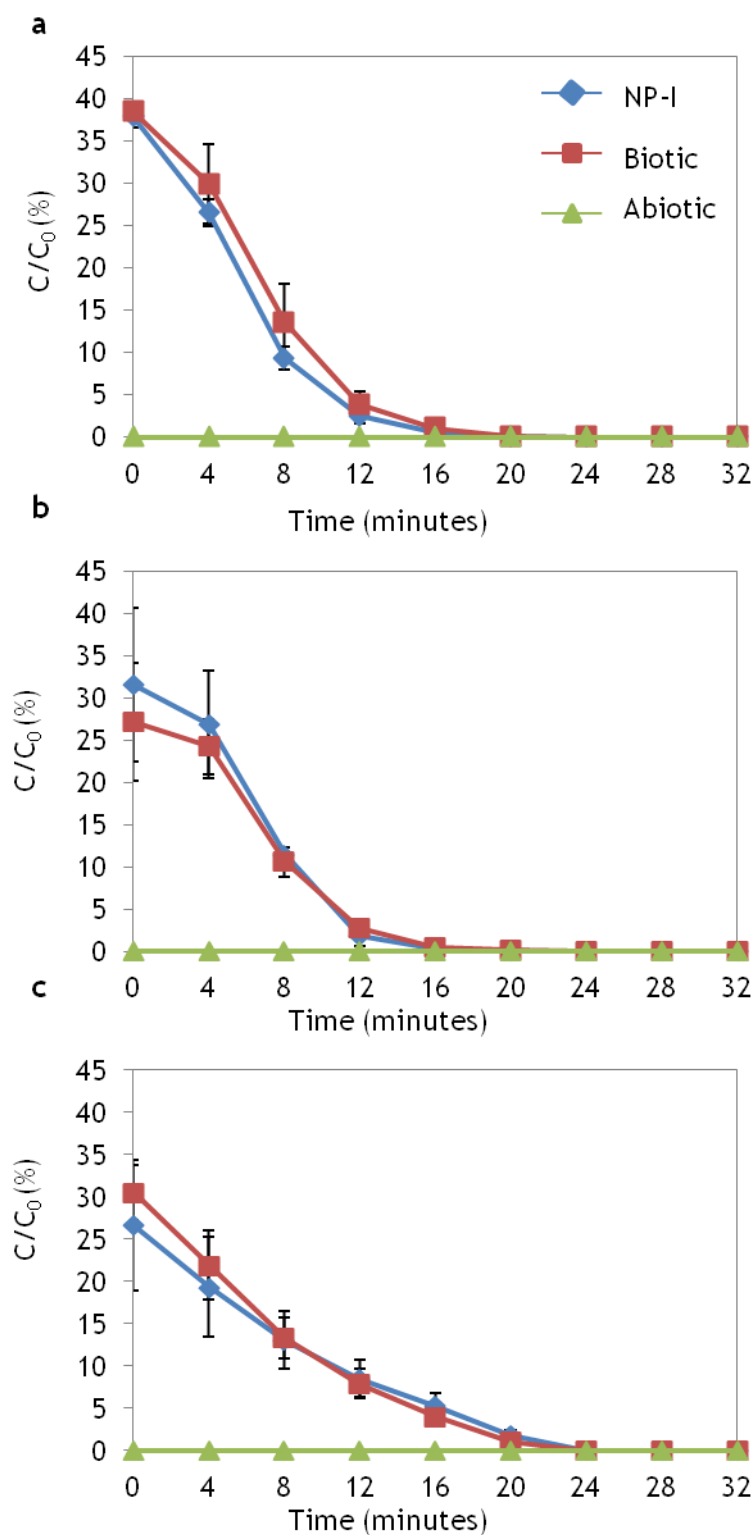


Figure 3.3: Breakthrough curves for the transport of NH_4^+ through the (a) fine, (b) medium and (c) coarse grained glass beads. Each data point represents the average of triplicate experiments with associated standard deviation ($\sigma = 1$, shown as error bars). 8 minutes = 1 pore volume.

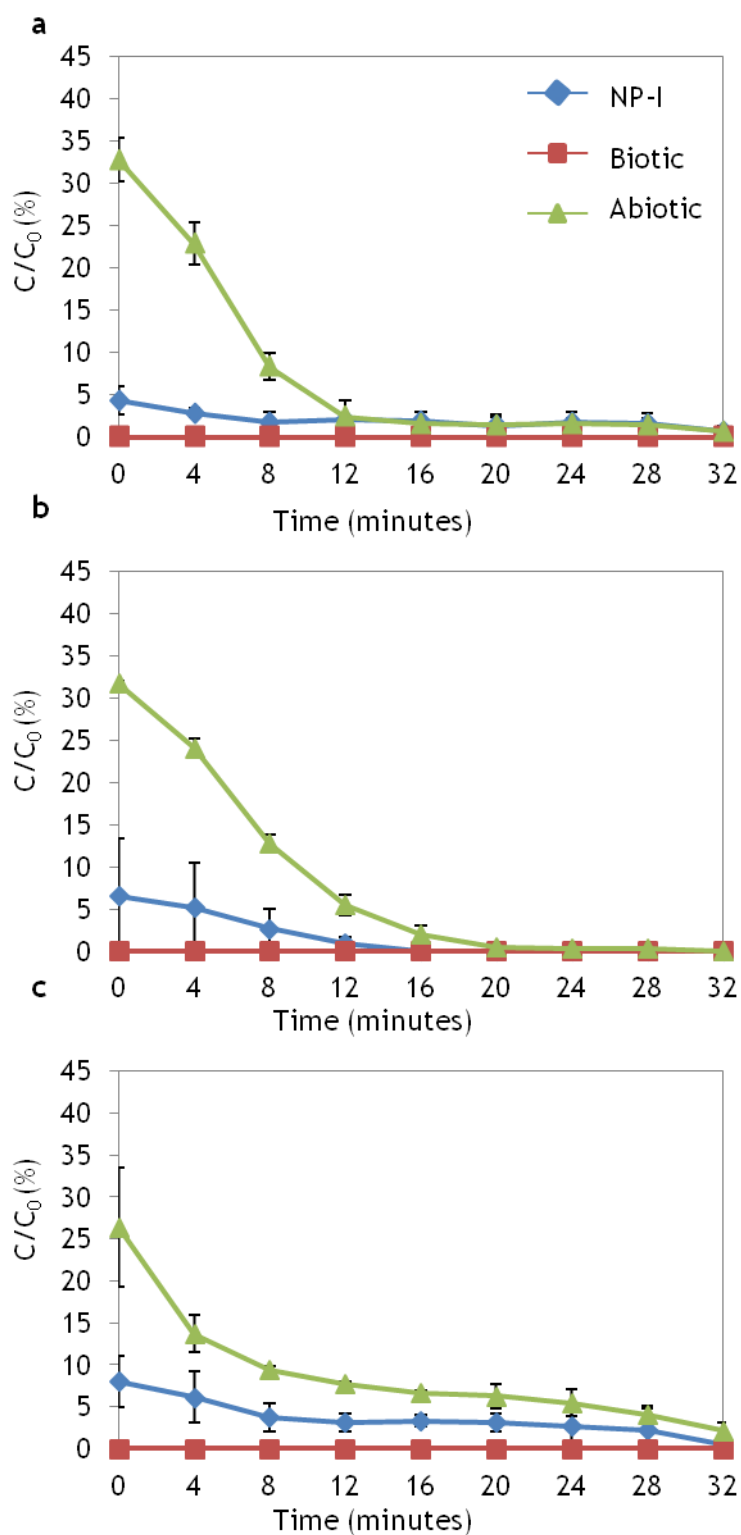


Figure 3.4: Breakthrough curves for the transport of Ca^{2+} through the (a) fine, (b) medium and (c) coarse grained glass beads. Each data point represents the average of triplicate experiments with associated standard deviation ($\sigma = 1$, shown as error bars). 1 pore volume = 8 minutes.

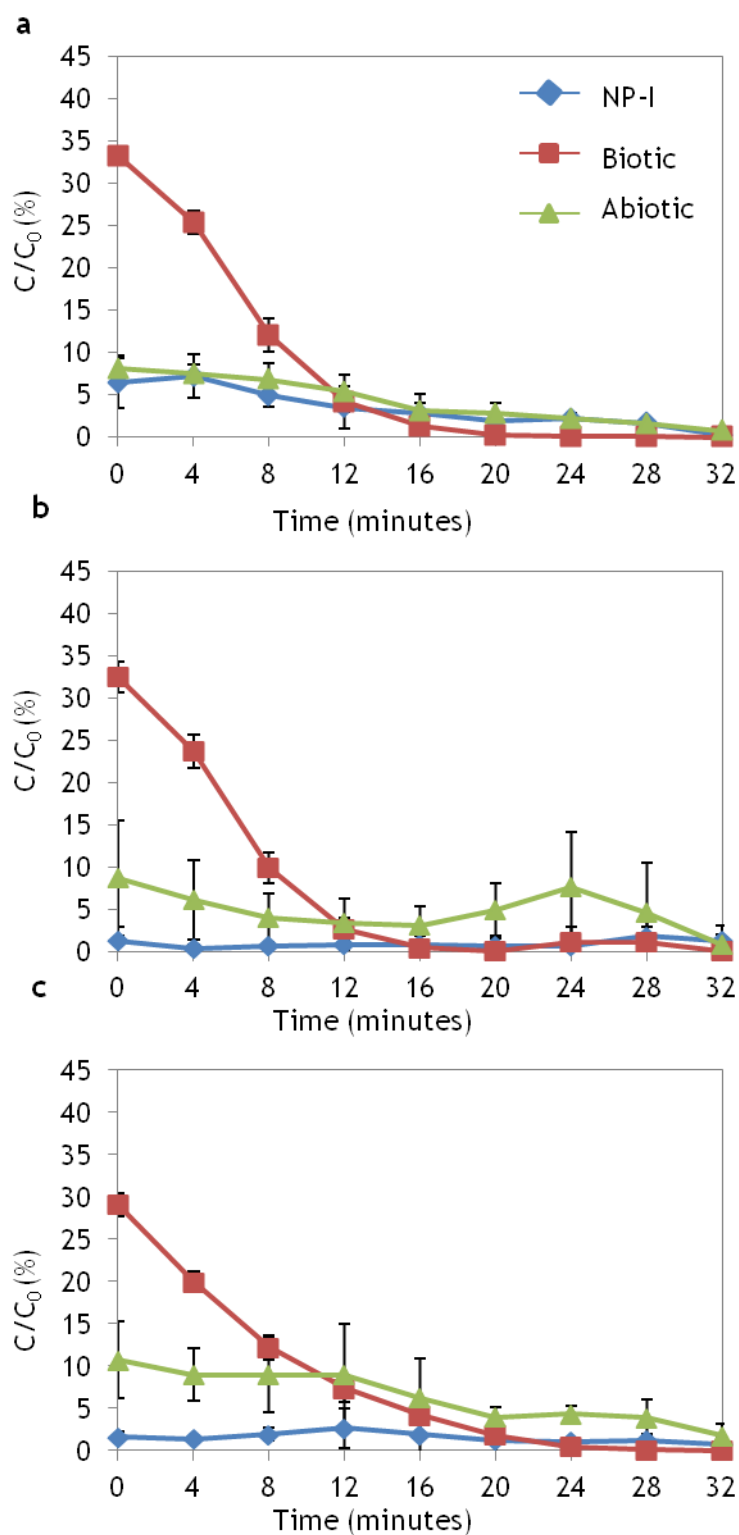


Figure 3.5: Breakthrough curves for the transport of (NPs) through the (a) fine, (b) medium and (c) coarse grained glass beads. Each data point represents the average of triplicate experiments with associated standard deviation ($\sigma = 1$, shown as error bars). 1 pore volume = 8 minutes.

3.4.1.2 Nanoparticle immobilisation through packed sand columns

Although trends were broadly similar, breakthrough profiles for quartz sand columns exhibit somewhat different results compared to glass beads. In the NP-I experiment 53 % NH_4^+ was detected in the effluent, whilst 63 % was detected in the effluent for the biotic control; although overlapping errors bars indicate these were not significantly different (Figure 3.6a). Both values are lower than those of the glass bead experiments (Table 3.1). Figure 3.6b exhibits the breakthrough curves for dissolved Ca^{2+} concentration. In the NP-I experiment only 9 % of the added Ca^{2+} was detected at the outlet compared to 75 % in the abiotic control, again indicating Ca^{2+} removal due to precipitation. The NP-I experiment saw the greatest reduction in the mobility of NPs through the column. Here, only 2 % NPs were detected at the outlet compared to 13 % in the abiotic control (note, however, that the error bars for the the NP-I and abiotic control overlap and so this difference is not statistically significant). The biotic control saw the highest rates of NP mobility with 50 % NP recovery (Figure 3.6c). Similar to the glass bead experiments, the order of NP breakthrough followed the order Biotic control > abiotic control > NP-I. A comparison of all porous media types can be seen in Table 3.1.

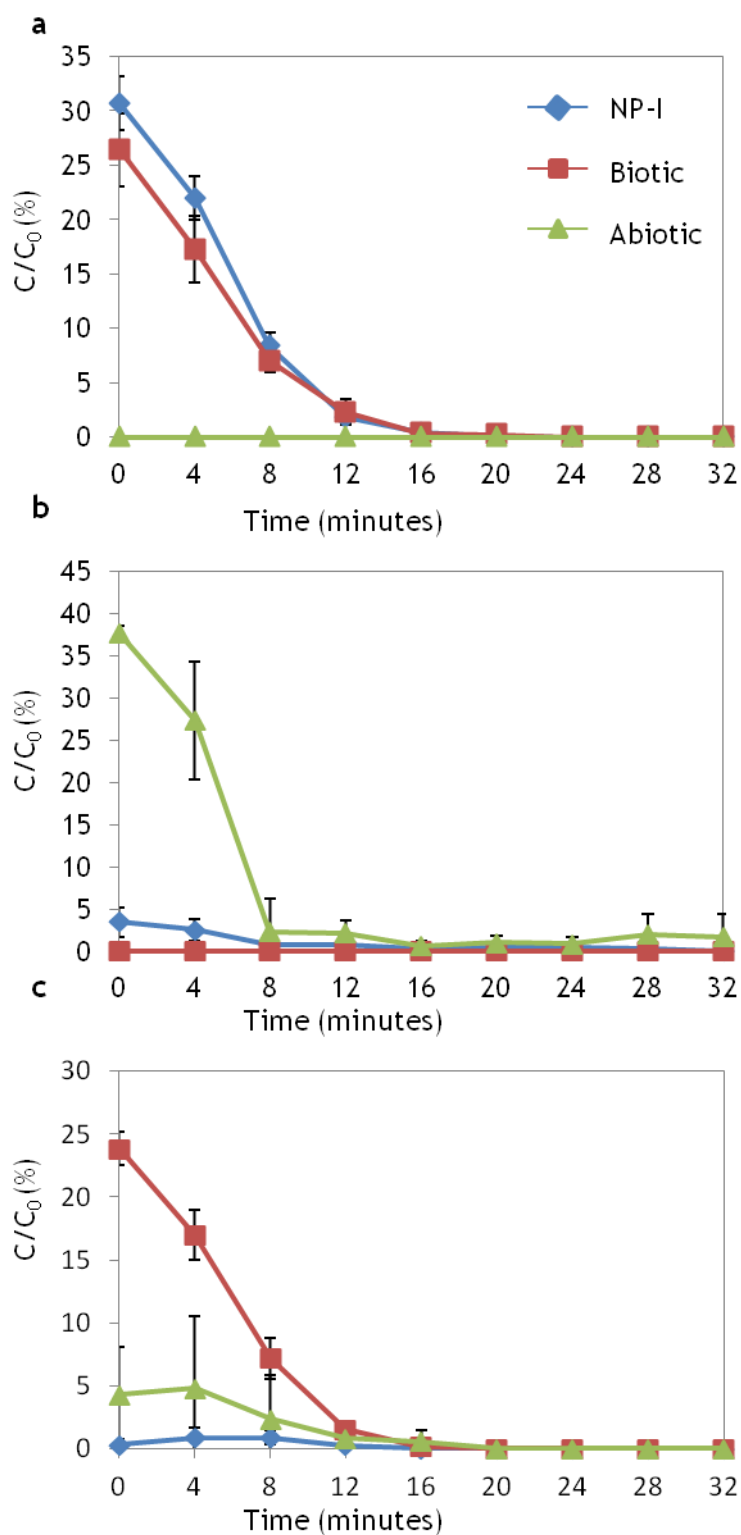


Figure 3.6: Breakthrough curves for the transport of (a) NH_4^+ , (b) Ca^{2+} and (c) NPs sand packed columns. Each data point represents the average of triplicate experiments with associated standard deviation ($\sigma = 1$, shown as error bars). 8 minutes = 1 pore volume.

Table 3.1: Total recovery of NH_4^+ , Ca^{2+} and NPs as calculated from the area under the recovery curve.

Porous media (mm)	pH			NH_4^+ (%)			Ca (%)			NP (%)		
	NP- 	Biotic	Abiotic	NP- 	Biotic	Abiotic	NP- 	Biotic	Abiotic	NP- 	Biotic	Abiotic
Fine (0.1-0.25)	8-9	9-9.5	6.5-8	78	87	-	18	-	73	31	76	38
Medium (0.6-1.8)	8-9	9-9.5	6.5-8	72	65	-	16	-	77	8	71	43
Coarse (2)	8-9	9-9.5	6.5-8	75	79	-	33	-	82	14	75	58
Sand (0.1-0.4)	8-9	9-9.5	6.5-8	63	53	-	9	-	75	2	50	13

3.5 Discussion

Particle transport through porous media is governed by interception by the porous media, sedimentation due to gravity, advection and diffusion via Brownian motion (Dunphy Guzman et al., 2006). For the first 24 hours advection does not influence NP transport, as during this static phase no fluid flow occurred. However with the onset of pumping advection will impart a strong influence on the transport of NPs throughout the column during this time. Furthermore, due to their small size and the absence of aggregation in these highly stable NPs, the effect of gravity induced sedimentation can be considered insignificant. However Brownian motion highly influences particle-particle and particle-collector interactions, especially in the case of very small particles (< 50nm, Schrick et al., 2004). Therefore in these experiments Brownian motion is responsible for NP-NP and NP-collector collisions during the first 24 hour static phase. The frequency of collisions is known to increase as particle size decreases, increasing the probability of NP-NP and NP-collector collisions,

regardless of external factors such as pH, ionic strength etc (Iijima and Kamiya, 2009). If such collisions during the static phase result in permanent attachment (deposition) NP transport will be reduced during the flushing phase.

Physiochemical interactions acting between the NPs and collector surface govern particle attachment (see Chapter 1.1.4 for further detail on NP physiochemical interactions). Attractive van der Waals forces have a strong influence on NP attachment; hence a potential barrier is required to maintain dispersed highly mobile NPs (Iijima and Kamiya, 2009). This may come in the form of electrostatic interactions where by the electric double layer (EDL) provides electrostatic repulsion between particles. However, electrostatic interactions are greatly affected by solution chemistry and cannot necessarily prevent attachment or NP-NP aggregation alone. To overcome this issue NPs are capped with various surface coatings which provide long ranged, robust electrosteric repulsion even at high ionic strengths (Saleh et al., 2008). The NPs used in this study display both electrostatic (zeta potential of -38 mv due to the carboxylated terminations repel from the negative quartz or glass surface) and electrosteric repulsions (provided by the dextran coating).

The first set of experiments aimed to investigate the attachment behaviour of negatively charged NPs in porous media as a function of grain size (fine, medium, and coarse grained) and grain type (quartz vs glass). NPs dispersed in SDW displayed high mobility upon flushing as indicated by 100% and 93% NP recovery in glass beads and quartz sand columns, respectively (Figure 3.2). Under these conditions the highly negative NPs (-38mV) are electrostatically repelled from the negative charge of the collector surfaces (both glass beads and sand grains, Behrens and Grier, 2001). In contrast, in the presence of 50 mM CaCl_2 significantly reduced NP mobility under all tested conditions (Figure 3.2). This is best explained by a reduction in repulsive EDL forces between NPs and grain surfaces in the presence of divalent electrolyte such as Ca^{2+} (see chapter 1.1.4). As a result, the energy barrier required for particles to attach is lower, allowing for enhanced particle-particle and particle-collector interaction (Lecoanet and Wiesner, 2004). Such interactions promote NP aggregation within the pore spaces and deposition onto the collector grains. It is important to note that during batch experiments (Chapter 2) NP aggregation did not occur in the abiotic control (contains 50 mM CaCl_2). Thus deposition onto collector grains rather than aggregation is likely the key mechanism here.

In the NP transport experiments for NPs suspended in SDW, NP retention was highest in the quartz sand column (18% eluted), followed by the coarse grained (72% eluted), then fine grained (84% eluted), and medium grained (92% eluted) glass bead columns (Figure 3.2, Table 3.1). Significantly more NPs were retained in the column containing quartz sand grains (18% eluted) compared to the fine glass beads (84% eluted; the sand grains are closest in size to the fine glass beads). Natural sand will inherently exhibit a larger degree of physical heterogeneity compared to the manufactured glass beads. The irregular size, shape and roughness of the sand grains providing more deposition sites compared to the smooth profile of the beads (Figure 3.7, Zhang et al., 2012). In addition to this sand grains may also contain geochemical heterogeneities such as naturally occurring metal oxide precipitates (Petosa et al., 2010). These are likely to not have been eliminated during washing. If metal oxides are present this may provide a slightly positive surface charge, promoting electrostatic attraction of NPs to the sand grains (Godinez et al., 2013). Indeed, surface charge heterogeneity has been shown to strongly control NP transport through sand packed columns, for example, Dunphy Guzman et al. (2006) found that NPs have limited mobility through natural sandy media rich in metal oxyhydroxides due to deposition.

Results from the transport experiments indicate a combination of both permanent and non-permanent attachment occurs. The observation that less than 100% NPs are recovered from the outlet indicates some permanent attachment (deposition) within the packed sand and glass beads. Furthermore, the presence of a tail in the breakthrough curves also suggests some non-permanent attachment (retardation) is occurring.

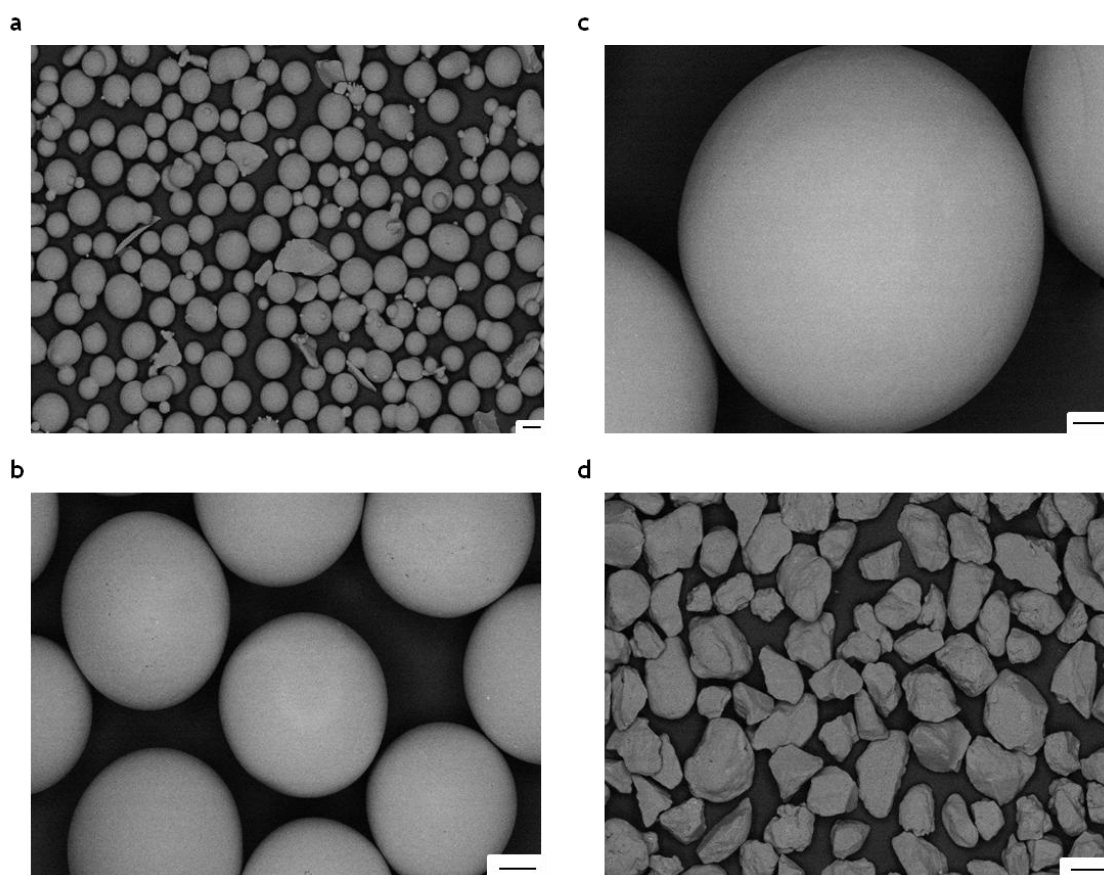


Figure 3.7: Scanning electron microscope images of porous media. Illustrating the smooth nature of the (a) fine (scale bar 100 μm), (b) medium (scale bar 200 μm) and (c) coarse gained glass beads compared to the irregular nature of the quartz sand grains (both scale bars 200 μm) (d).

In the NP immobilization experiments, the lowest rates of NP mobility were found in columns where calcite precipitation was promoted (NP-I experiments), suggesting solid-phase-capture had enhanced NP immobilization. As urea hydrolysis commences the bacterium create a micro-environment around the cell which is oversaturated with respect to calcium carbonate, owed to the formation of NH_4^+ (increasing pH) and the production of HCO_3^- ; (Stocks-Fischer et al., 1999). As calcium carbonate nuclei form in the vicinity of the bacterium the NPs become electrostatically attracted to its positive surface charge and occluded (Chapter 2). The resulting nano-mineral composite is prone to gravitational settling, as seen in the batch experiments performed in Chapter 2. Aided by gravitational settling the nano-mineral composite is cemented to the grain boundaries within the column, preventing further NP transport. See Chapter 2.6 for more details on NP capture mechanisms. Furthermore, it is

important to note that 100% Ca^{2+} elution from the column does not occur in the abiotic control for all experiments, (see Table 3.1) this suggests that Ca^{2+} ions bind to collector surfaces negative charge. Therefore calcite may also nucleate directly on grain boundaries and occlude NPs as it grows away from the grains. Bacteria (which possess a negative surface charge) may become entombed within the mineral precipitate (Tobler et al., 2012), as do the NPs. However if any bacterial entombment did occur this did not significantly impact urea hydrolysis as the breakthrough curve profiles for NH_4^+ for the NP-I and biotic control experiments are almost identical for all porous media types (Figure 3.3 and Figure 3.6a). The process of NP immobilisation is illustrated in Figure 3.8.

It is important to note that the effluent samples were not filtered prior to analysis. Therefore the observation that small amounts of Ca^{2+} and NP eluted from the column in the NP-I experiments (Figure 3.5, Table 3.1) may be due to the flushing out of small NP-containing precipitates which were not cemented to the collector surfaces. The aim of this research was to immobilise NPs within bacterially mediated calcium carbonate in order to prevent NP transport. Therefore NPs which are sufficiently mobile, whether trapped within calcite or not, are deemed as unsuccessfully captured. Despite this, the process of occlusion would cover the surface of any toxic NPs in a benign calcite coating, isolating the NPs toxic surface from the environment. Thus we speculate here that even mobile NPs, if coated in calcite, may have reduced toxicity.

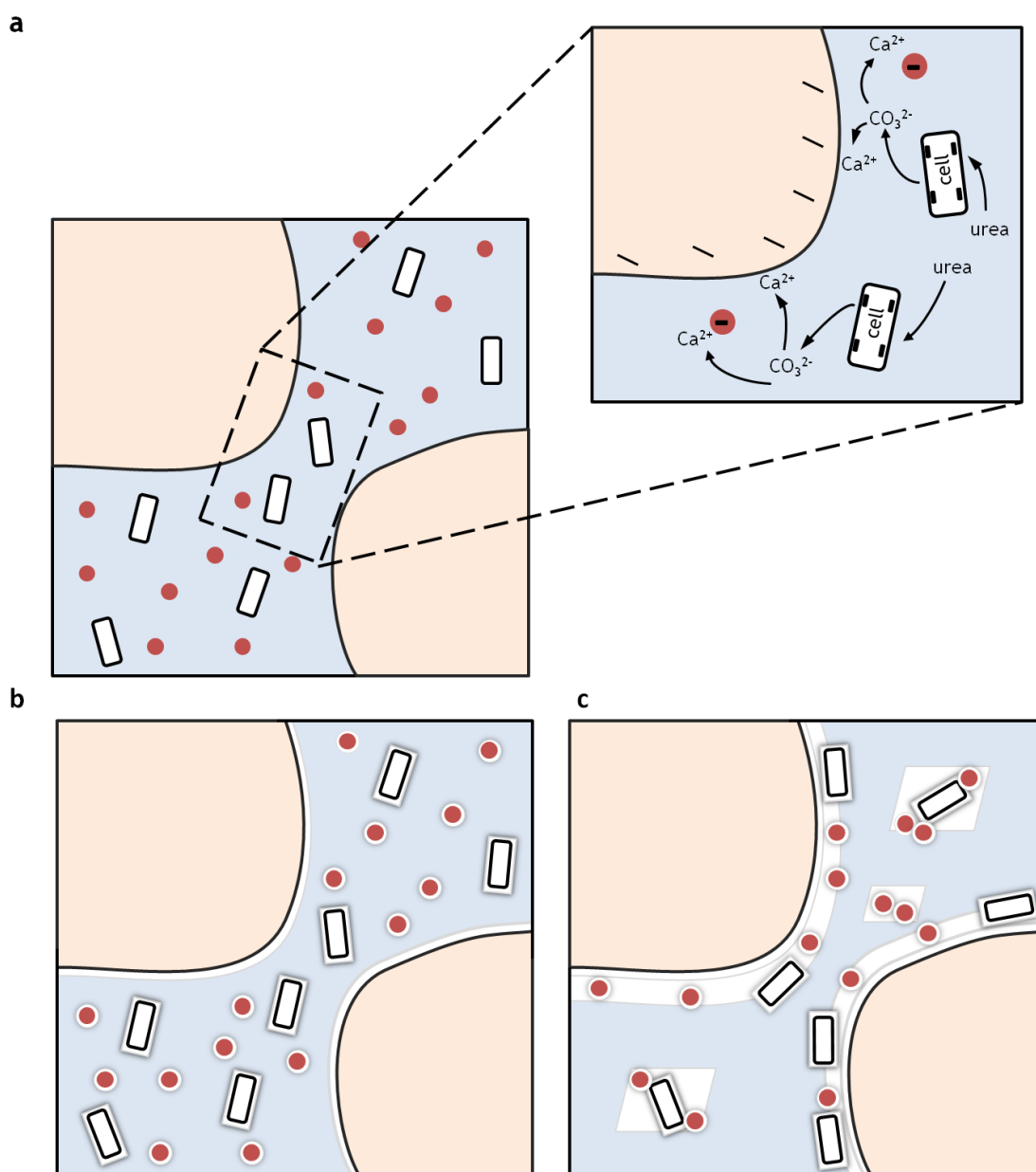


Figure 3.8: Simplified sketch detailing the immobilisation of NPs within porous media. (a) Bacterial cells exist within the pore spaces, being electrostatically repulsed by the NPs and collector surfaces. Ca ions are attracted to the negative charge of the NPs and collector surfaces. As carbonate is produced by ureolysis, calcite precipitates onto available surfaces (b), i.e. the NPs, collector surfaces and the bacteria cells. NPs are also electrostatically attracted to the growing calcite surface (c) With further calcite precipitation NPs and bacteria cells become entrapped within the mineral precipitate, immobilised within the pore spaces and on the collector surfaces.

Aside from the NP-I experiments the abiotic control saw significantly low rates of NP transport compared to the biotic controls. Here, ionic strength (50mM CaCl_2) in the pore water had a marked influence on the retention of NPs in the column (as demonstrated by my NP transport experiments, Figure 3.2). The high salt concentration exhibited in the abiotic control acts to reduce the repulsive EDL forces, allowing for more particle-collector interaction, resulting

in the deposition of NPs on collector surfaces (Figure 3.2a-c). This electrokinetic effect may also come into play for the NP-I experiments. However the ionic strength of the solution, where calcite precipitation is occurring, will change as hydrolysis progresses. The ionic strength (I) of the solution was calculated according to the following equation:

$$I = \frac{1}{2} \sum cz^2$$

where c is the molar concentration and z is the charge of each of the ions in solution. The total ionic strength of the reaction solution at the start of the experiment is 150 M/m^3 due to the presence of 50 mM CaCl_2 . However, as the bacteria hydrolyse urea, ammonium and bicarbonate ions are produced. The bicarbonate ions will immediately bond with the calcium to form calcium carbonate nuclei in solution. Hence the concentration of calcium in solution will decrease as hydrolysis progresses, decreasing the ionic strength of the solution. Whilst the concurrent production of ammonium ions will act to increase the ionic strength of the solution. It is important to note that calcium is a divalent ion, whilst ammonium is monovalent. Hence, a reduction in the calcium concentration imparts a strong influence on the EDL forces acting on the NP and collector surfaces compared to the monovalent ammonium ion. By the time column solution chemistry is analysed, after 24 hours, the net ionic strength has decreased to 100 M/m^3 , that is if total urea hydrolysis occurs, i.e. 100 mM NH_4^+ produced. A reduction in the total ionic strength in the NP-I experiments promotes electrostatic repulsion, aiding NP transport through the column. Hence, NP attachment via solid phase capture must be the dominant removal mechanism in columns where calcite precipitation is promoted.

The highest rates of NP transport for all porous media types were found in the biotic control experiments. Here the concentration of NPs eluted range from 50-76%. The high rates of NP transport exhibited here are in part due to electrostatic repulsion between the negatively charged NPs, bacterium and collector surfaces. More importantly, this electrostatic repulsion is maintained due to the low ionic strength of the solution (no CaCl_2). Despite this NP retention did occur. NP transport through porous media is highly influenced by Brownian motion (Dunphy Guzman et al., 2006). Importantly as particle size decreases the rate of Brownian motion increases, hence particle-collector collisions are highly

likely for very small NPs (<50nm) (Schrack et al., 2004). In addition to this NPs may be transported to collector surfaces due to advection which occurs when pumping commences. Here NPs move with the bulk movement of the fluid, transporting NPs to collector surfaces. It appears that a proportion of the NPs had the ability to overcome the energy barrier required for deposition, becoming attached to collector surfaces. Aside from this a physical straining mechanism may act on the NPs, even though the NPs are significantly smaller than the media pore space. If physical straining is the dominant mechanism of NP removal here it would be expected that the fine grained glass beads would show the highest rates of NP removal. However this was not the case, instead the medium grained beads showed the lowest rates of NP removal with 71% elution whilst the fine grained beads saw the highest rates of NP transport with 76% elution. Furthermore, the spread of data for the glass bead experiments is very narrow with the breakthrough profiles all falling within error of each other. Therefore straining mechanisms are not supported by the data.

Electrokinetic effects play a major role in determining the fate of NPs within the environment. Importantly the ionic strength used here is not representative of the chemistry of natural waters. Instead this was chosen to allow a direct comparison to the chemistry of the NP-I experiments. Typical groundwaters display 1-10 mM monovalent cations (Na^+ , K^+) and 0.1-2 mM divalent cations (Ca^{2+} , Mg^{2+}) (Saleh et al., 2008). Under such conditions Saleh et al. found polymer-modified particles to be highly mobile. In such instances induced calcite precipitation may be employed to immobilise NP pollutants within the subsurface. This may be implemented by drilling strategic injection points where by one well injects the bacterial suspension and another urea and CaCl_2 . When the two fluids mix within the target zone (NP plume) urea hydrolysis will commence stimulating the precipitation of calcium carbonate, resulting in the in-situ immobilisation of NPs.

3.6 Conclusion

In this study ureolytically driven calcium carbonate precipitation was shown to successfully immobilise negatively charged NPs within porous media. Although NP mobility was reduced under all experimental conditions tested, the lowest rates of NP mobility were consistently found in columns where calcium

carbonate precipitation was promoted. The results presented here suggest that bacterially induced calcite precipitation may be used as a tool to significantly reduce NP mobility in environmental systems.

4 Immobilisation of nanoparticles by bacterially precipitated struvite

While an array of techniques are available for *in situ* remediation of numerous groundwater contaminants, there are currently none for *in situ* remediation of nanoparticles (NPs). Experiments presented in chapter 3 showed that bacterially driven calcite precipitation can be used as a tool to immobilise nanoparticles within calcite crystals through solid phase capture. In this process, electrostatic interactions between the growing calcite surface and the NP greatly controlled the degree of NP capture; NPs with a negative surface charge were captured with greater efficiency than those with a positive surface charge, due to stronger electrostatic attachment of negative NPs to positive calcite surfaces. This indicated that in order to immobilise NPs with a positive surface charge, a mineral with a negative surface charge would be required. Struvite ($\text{MgNH}_4\text{PO}_4 \cdot 6\text{H}_2\text{O}$) is such a mineral, commonly forming in high nutrient waters, leading to the deposition of scale deposits on wastewater pipes (Ali, 2007). The struvite precipitating system tested here showed high success rates at capturing positively charged NPs. However, the key mechanism of immobilization appeared to be attachment to the struvite surface, as opposed to occlusion within the growing mineral (as reported for calcite in chapter 3). Results indicated that changes in pH and ionic strength have considerable impact on NP attachment and detachment due to their impact on the surface charge of the mineral and NP with less attachment occurring as pH decreased and ionic strength increased. Overall, these findings suggest that the mineral precipitating system can be specifically tailored to suit the surface character of the NP targeted. NP attachment onto mineral matrices has the potential to be used as a tool to prevent NP mobility in contaminated groundwaters and to remove NPs from wastewater treatment systems.

4.1 Introduction

The potential of bacterially driven solid phase capture to immobilise NP pollutants within the subsurface has yielded promising results. Chapter 2 showed that calcite precipitation driven by bacterial ureolysis is very effective at capturing highly stable and negatively charged NPs within the growing calcite

crystal. This process was underpinned by attractive forces between oppositely charged calcite (positive) and NP (negative) surfaces. Conversely, NPs with a positive surface charge showed poor attachment to calcite surfaces due to electrostatic repulsion and remained in suspension, i.e., could not be immobilised using this approach. Here, we hypothesise that for capturing positively charged NPs within a growing crystal, a mineral possessing a negative surface charge is required.

Struvite ($\text{MgNH}_4\text{PO}_4 \cdot 6\text{H}_2\text{O}$) has been specifically selected as a possible candidate for such a system as it exhibits a negative surface charge (Bouropoulos and Koutsoukos, 2000). In addition to this, it is also used as a remediation technique for excess nitrogen (ammonia) and phosphorus in industrial wastewater (Zhou and Wu, 2012, Ryu and Lee, 2010, Ryu et al., 2008, Pastor et al., 2008, Doyle and Parsons, 2002). This is of particular interest here as the process of bacterial ureolysis (as used to induce calcite precipitation), undesirably, produces ammonia as a by-product, thus the precipitation of struvite could potentially be used in conjunction to ureolysis-driven technologies to remove excess ammonium from environmental systems.

Struvite ($\text{MgNH}_4\text{PO}_4 \cdot 6\text{H}_2\text{O}$) is a white orthorhombic mineral containing equimolar concentrations of magnesium, ammonia and phosphate (Eqn.1). Struvite precipitation is strongly dependant on pH, the ratio of $\text{NH}_4^+:\text{Mg}^{2+}:\text{PO}_4^{3-}$, temperature and the presence of foreign ions such as calcium (Doyle et al., 2003, Doyle and Parsons, 2002). Generally, the solubility of struvite decreases with increasing pH up to pH 9 (Nelson et al., 2003). Above this, struvite solubility increases proportionally with phosphate concentration, but inversely to ammonia concentration (Doyle and Parsons, 2002).



Historically struvite precipitation has been extensively studied due to its formation on waste water pipes from industrial wastewater. The hard deposit causes a range of operational problems ranging from increased pumping costs to the replacement of sections of pipe work (Doyle and Parsons, 2002, Ohlinger et al., 1998, Doyle et al., 2003). Recently the problem mineral has gained positive attention due to its potential use as a slow release fertiliser (Desmidt et al., 2013, Doyle et al., 2003). Traditionally the agricultural industry produces fertiliser from mined phosphate rock (Desmidt et al., 2013). However increasing global

demand for fertiliser is putting pressure on this finite resource and so alternative sources of phosphate are required (Uludag-Demirer et al., 2005). This has provided an economic incentive to recover phosphate from nutrient rich wastewater through controlling the precipitation of struvite. Sales of struvite within the UK have the potential to provide revenue of up to £20,000 a year (Jaffer et al., 2002). In addition struvite precipitation has received attention from a wide range of fields, including such as the veterinary (Osborne et al., 1999), medical (Clapham et al., 1990) and the food and beverage industry (Foletto et al., 2013, Johns, 1995).

In this study we investigate the potential of struvite precipitation to immobilise positively charged NPs while simultaneously removing excess NH_4^+ produced by bacterial ureolysis. It is expected that positively charged NPs electrostatically bind to the negatively charged growing struvite surfaces. As mineral growth proceeds, these NPs become immobilised within the mineral matrix, thereby removing them from the aqueous phase.

4.2 Materials and methods

4.2.1 Nanoparticles

The positively charged NPs (S-posNPs) were prepared in the same manner as in Chapter 2.3.1.

4.2.2 Struvite precipitation experiments

First, struvite precipitation experiments were undertaken in the absence of NPs. These experiments were performed to determine optimal conditions for struvite precipitation. A summary of all the tested experimental conditions are shown in Table 4.1.

Two different types of batch experiments were carried out: S1) struvite precipitation during bacterial ureolysis, i.e., Mg^{2+} and PO_4^{3-} are added at the beginning and NH_4^+ is being continuously produced through ureolysis, and S2) struvite precipitation following ureolysis, i.e., all NH_4^+ is produced first by ureolysis, before Mg^{2+} and PO_4^{3-} are added in four steps.

Both types of experiments were performed using the gram positive ureolytic bacterium *Sporosarcina pasteurii* (strain ATCC 11859). Details of the preparation of bacteria are given in Chapter 2.3.2. For S1a experiments the bacterial pellet was re-suspended in a solution containing 20 mM K_2HPO_4 , diluted to an optical density (OD) of 0.14 (as determined spectrophotometrically at 600 nm). Separately, a solution containing 10 mM urea and 20 mM $MgCl_2$ was prepared. To start the experiment, the urea and $MgCl_2$ solution were mixed at a ratio of 1:1 with the bacterial and K_2HPO_4 suspension. The final concentrations for experiment S1a were 5 mM urea, 10 mM K_2HPO_4 and $MgCl_2$ and 0.07 OD *S. pasteurii*. Biotic controls, S1b (*S. pasteurii* + urea + K_2HPO_4 ; the absence of $MgCl_2$ preventing struvite precipitation) were done to track the progress of ureolysis, while abiotic controls S1c (K_2HPO_4 + $MgCl_2$) were run to ensure that Mg^{2+}/PO_4^{3-} removal would result only as a consequence of NH_4^+ production. Concentrations of K_2HPO_4 and $MgCl_2$ were intentionally kept low in order to prevent the precipitation of magnesium phosphate minerals instead of struvite.

For the S2 experiment the bacterial pellet was re-suspended and diluted in sterile deionised water (SDW). The bacterial solution (0.14 OD *S. pasteurii*) was mixed with a 100 mM urea solution to give a final concentration of 50 mM urea and 0.07 OD *S. pasteurii*. These concentrations were chosen to follow the concentrations used for calcite precipitation in Chapters 2 and 3. This mix was left for 24 hours for urea hydrolysis to complete, giving a final concentration of 100 mM NH_4^+ . A concentration of 100 mM NH_4 was chosen to simulate the level of NH_4^+ produced by bacterial ureolysis in Chapter 3 and 4. To initiate struvite precipitation, 25 mM Mg^{2+} and PO_4^{3-} injections were added as dry solids (using $MgCl_2$ and K_2HPO_4 salts) in 4 stages. Adding Mg^{2+} and PO_4^{3-} sources as dry solids and in 4 stages prevented the premature precipitation of magnesium phosphate minerals.

4.2.3 Nanoparticle capture by struvite precipitation

S2 experiments (staged approach) yielded best conditions for struvite precipitation (see section 4.3.1), thus an identical set-up was chosen for the nanoparticle remediation experiments (N1 and N2, both experiments are identical other than solution pH is maintained between 8 and 9 in the N2 experiment). These were the same as the S2 experiments except that prior to

the addition of the Mg^{2+} and PO_4^{3-} salts, the solution was filtered (using sterile 0.2 μ m membrane filters) to remove bacterial cells that could immobilise the positively charged NPs (as observed in Chapter 2). This was done to ensure that NP removal could only result from struvite precipitation. Following filtration, 10 mg/l NPs were added to the experiment. Biotic and abiotic control experiments were also run (see Table 4.1). All nanoparticle remediation experiments were carried out in triplicate in glass beakers that were covered with parafilm[®] to prevent evaporation.

Table 4.1: Summary of tested experimental conditions.

Run	<i>S. pasteurii</i> (OD_{600})	Urea/ NH_4 (mM)	$MgCl_2$ (mM)	K_2HPO_4 (mM)	NP (mg/l)
<i>Struvite precipitation experiments</i>					
S1a	0.07	5/10	10	10	-
S1b	0.07	5/10	-	10	-
S1c	-	-	10	10	-
S2	0.07	50/100	25*	25*	-
<i>NP immobilisation experiments</i>					
N1a	0.07	50/100	25*	25*	10
N1b	0.07	50/100	-	25*	10
N1c	-	-	25*	25*	10
N2a	0.07	50/100	25*	25*	10
N2b	0.07	50/100	-	25*	10
N2c	-	-	25*	25*	10

* concentrations of $MgCl_2$ and K_2HPO_4 added 4 times to give a final concentration of 100 mM. The N2 experiments were controlled between pH 8 and 9.

4.2.4 Nanoparticle removal by pre-formed struvite

A NP sorption experiment was devised to determine the effect of ionic strength on the attachment of positively charged NPs on to the struvite surface. For this, struvite was precipitated using the same approach as for S2 experiments. Once precipitated the mineral was separated via centrifugation and washed 3 times in SDW to remove excess salts. Equal quantities (0.6 g wet weight) of struvite were weighed and suspended in 10 ml KCl solutions at 4 different concentrations (0, 50, 150 and 250 mM). KCl was used as these are the ions that remain in solution once struvite has precipitated in experiments tested here. NPs were then added to give a concentration of 5 mg/l (Fe concentration). The concentration of NPs was reduced here to save on experimental costs.

4.2.5 Chemical analysis

Solution pH and concentrations of NH_4^+ , Mg^{2+} , PO_4^{3-} and Fe (iron used as a proxy for nanoparticle concentration) were determined at time zero and at regular intervals thereafter. At each sampling time 10 ml aliquots were removed from the experiment; 5 ml were used for pH measurement, 0.5 ml to determine NH_4^+ by the Nessler assay and 4.5 ml were mixed with 1 ml 50% HCl for Mg^{2+} , PO_4^- and Fe measurements. PO_4^- concentrations were determined using the molybdenum blue method (Murphy and Riley, 1958) whilst Mg^{2+} and Fe concentrations were analysed using atomic absorption spectroscopy. For Mg^{2+} analysis calibration standards of 0.3, 0.5, 0.7 and 1 mg/l were prepared prior to each analysis using MgCl_2 . An air-acetylene flame was used for all Mg^{2+} determinations at a flow rate of 0.9 - 1.2 l/min. The spectrometer was operated at a wavelength of 285.2 nm and a spectral band pass of 0.5 nm with the lamp current running at 75%. The analytical limit detected under these conditions is 0.003 mg/l. For details on Fe analysis by AAS see Chapter 2.3.3.

4.2.6 Zeta potential analysis

The zeta potential of struvite was investigated as a function of pH and ionic strength. Preformed struvite crystals (struvite was precipitated using the same approach as for S2 experiments) were separated via centrifugation and washed 3 times in SDW to remove excess salts. The cleaned struvite crystals were separated via centrifugation before equal quantities (0.6 g wet weight) of struvite were weighed and suspended in 10 ml KCl solutions at 4 different concentrations (0, 50, 150 and 200 mM). KCl was used as these are the ions that remain in solution once struvite has precipitated in experiments tested here. The pH of the reaction solution was then adjusted using NaOH and HCl over the pH range of 6 to 12. Zeta potential measurements were immediately run using Zetasizer Nano ZS (Malvern Instruments) at 25°C.

4.2.7 Scanning Electron and Raman Microscopy

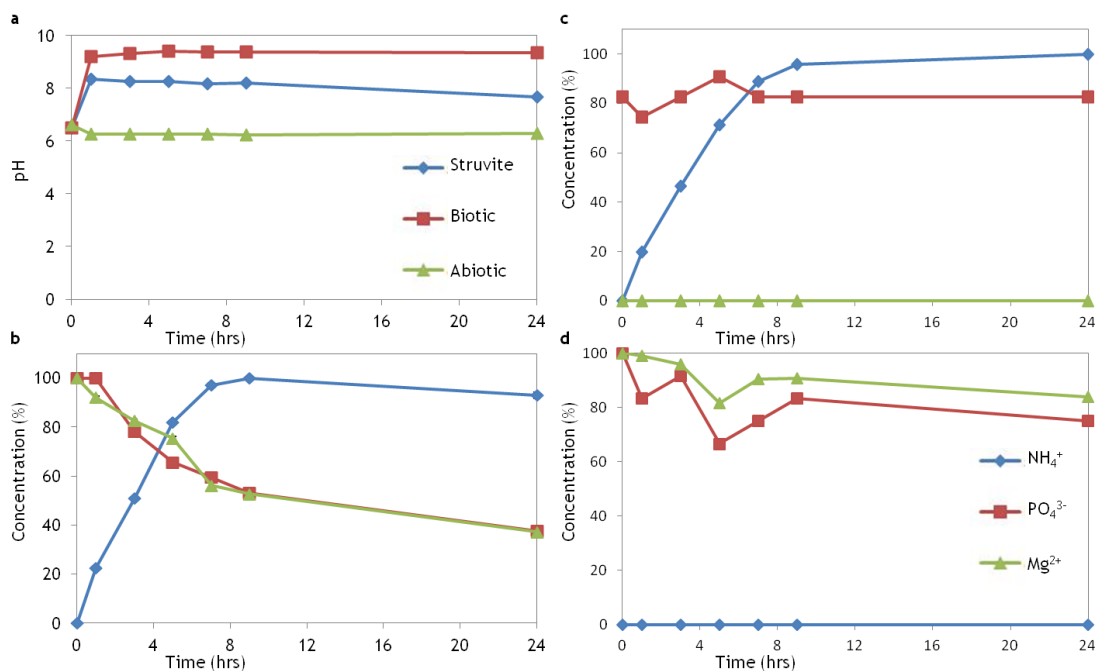
Mineral identification was performed by SEM and Raman analysis. Once the reactions were completed, precipitates were removed by centrifugation, washed three times with SDW, and then dried for 24 hours at 30°C. Dried precipitates were mounted on aluminium stubs, carbon coated and imaged using a Zeiss Sigma Field-Emission Scanning Electron Microscope with a beam intensity of 20

kV. Raman spectroscopy was carried out to gather additional chemical information of the struvite crystals. Uncoated precipitates were analysed using Renishaw Invia Raman Microscope with Wire 3.2 software. Samples were excited using a 514-nm edge green laser, and spectra were obtained using a static scan with a centre of 920 cm^{-1} .

4.3 Results

4.3.1 Struvite precipitation experiments

In the first set of struvite precipitation experiments (S1: struvite precipitation during ureolysis) bacterial ureolysis led to an increase in NH_4^+ in both the struvite precipitation experiment (S1a) and biotic control (S1b, 4.1b-c, Table 4.1). With the onset of ureolysis in S1a, it was expected that the increase in NH_4^+ would lead to struvite supersaturation and hence struvite precipitation. This in turn would result in a decrease in NH_4^+ , Mg^{2+} and PO_4^{3-} . However, this was not observed. Instead, NH_4^+ increased at almost identical rates in the struvite precipitation and in the biotic control experiment (4.1b-c), 95% of the initially added urea was hydrolysed within only 8 hours. The absence of NH_4^+ removal showed that struvite precipitation did not occur. Nevertheless, a white coloured precipitate was observed at the bottom of the reaction vessel. The simultaneous decrease in dissolved Mg^{2+} and PO_4^{3-} from 100 to 40% over the duration of the experiment (4.1b) indicated this precipitate was some form of Mg-phosphate. In the biotic control (S1b; 4.1c) no precipitation was observed due to the absence of Mg^{2+} . Similarly, no precipitation was observed in the abiotic control (S1c; 4.1d) despite the presence of both Mg^{2+} and PO_4^{3-} ions (although Mg^{2+} and PO_4^{3-} concentrations did decrease slightly over the duration of the experiment).



4.1: Time series showing changes in pH, NH_4^+ , Mg^{2+} , PO_4^{3-} concentration for the S1 experiment.

(a) pH over time for the struvite precipitation experiment, the biotic (S1b) and the abiotic control (S1c). (b, c and d) NH_4^+ , Mg^{2+} and PO_4^{3-} concentration profiles for (b) S1a struvite precipitation experiment which contained 0.07 OD *S.pasteurii*, 5 mM urea giving 10 mM NH_4^+ , and 10 mM Mg^{2+} and PO_4^{3-} (c) S1b contained all components except MgCl_2 and (d) S1c contained all components except bacteria and urea. For the S1 experiment each data point represents the average of triplicate experiments with associated standard deviation ($\sigma = 1$, shown as error bars).

In the second struvite precipitation experiment (S2; struvite precipitated after ureolysis, Table 4.1), urea hydrolysis was completed before adding Mg^{2+} and PO_4^{3-} sources. Upon *S.pasteurii* addition urea hydrolysis was completed within 24 hours producing 100 mM NH_4^+ . In order to prevent precipitation of magnesium phosphate phases, Mg^{2+} and PO_4^{3-} were added in 4 stages of 25 mM (added as dry solids to prevent dilution of the NH_4^+ solution) to equal the NH_4^+ concentration of 100 mM. After the first addition of Mg^{2+} and PO_4^{3-} an immediate decrease in NH_4^+ by 25% was observed (Figure 4.2). The concentration of Mg^{2+} and PO_4^{3-} was also noted to return to zero (Figure 4.2), indicating a stoichiometric 1:1:1 ratio of NH_4^+ , Mg^{2+} and PO_4^{3-} had been removed from solution. This was accompanied by the formation of a white coloured precipitate (4.5a), which considering the 1:1:1 stoichiometry was likely to be struvite. After the second Mg^{2+} and PO_4^{3-} addition, no decrease in NH_4^+ was observed. However, after the third addition, NH_4^+ decreased to 60% (Figure 4.2). Following the fourth addition, NH_4^+ continued to decrease to give a final concentration of 2% NH_4^+ , indicating that almost all NH_4^+ was removed. By this stage, all Mg^{2+} and PO_4^{3-}

had also been removed, again indicating a stoichiometric removal of 1:1:1 for NH_4^+ , Mg^{2+} and PO_4^{3-} , consistent with struvite formation. It is important to note that the concentration of $\text{Mg}^{2+}/\text{PO}_4^{3-}$ at each sample point shown in Figure 4.2 is a percentage of the total $\text{Mg}^{2+}/\text{PO}_4^{3-}$ that was added prior to the sampling point. For example sample point 2 reads 3 % Mg^{2+} , that is 3 % of the 25 mM Mg^{2+} added remained in solution. Similarly the sample point at 1.5 hrs reads 20 % Mg^{2+} , meaning that 20 % of the total 100 mM Mg^{2+} added remained in solution. The erratic removal of NH_4^+ may be explained as $\text{Mg}^{2+}/\text{PO}_4^{3-}$ salts were added as dry solids (in order to prevent dilution), and so all of the added $\text{Mg}^{2+}/\text{PO}_4^{3-}$ may not have fully dissolved before the subsequent sampling point (this would be difficult to observe due to the immediate precipitation of struvite creating a cloudy appearance to the reaction solution). Therefore, as the experiment progresses more $\text{Mg}^{2+}/\text{PO}_4^{3-}$ is becoming available through dissolution, allowing for the continual precipitation of struvite. This method of struvite precipitation has shown much better success compared to the S1a experiment, where no struvite formed. This experimental approach was therefore used for the NP immobilisation experiments.

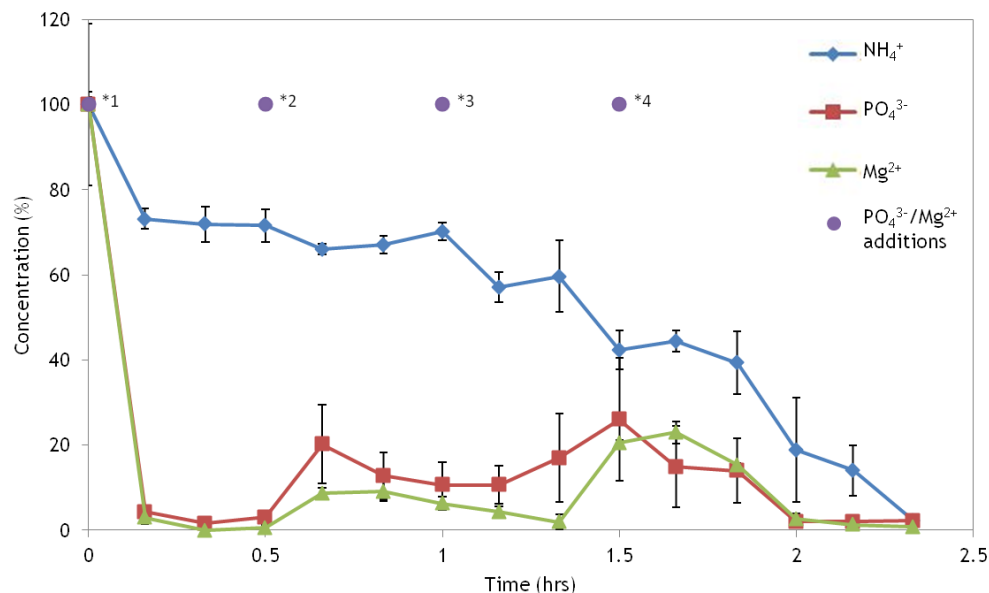


Figure 4.2: Time series showing changes in pH, NH_4^+ , PO_4^{3-} and Mg^{2+} concentration for experiment S2.

Experiment S2 contained 0.07 OD *S.pasteurii* and 50 mM urea, giving 100 mM NH_4^+ , once total urea hydrolysis was achieved 25 mM K_2HPO_4 and MgCl_2 were added 4 times to give a final concentration of 100 mM. The graph here shows data points after total urea hydrolysis had occurred (i.e. it shows the period of time during which K_2HPO_4 and MgCl_2 were added). The $\text{Mg}^{2+}/\text{PO}_4^{3-}$ concentration at each sample point is a percentage of the total $\text{Mg}^{2+}/\text{PO}_4^{3-}$ that was added prior to that sampling point. The purple circles represent the time points at which PO_4^{3-} and Mg^{2+} sources were added giving a total $\text{Mg}^{2+}/\text{PO}_4^{3-}$ concentration of (*1) 25

mM $\text{Mg}^{2+}/\text{PO}_4^{3-}$ (*2) 50 mM $\text{Mg}^{2+}/\text{PO}_4^{3-}$ (*3) 75 mM $\text{Mg}^{2+}/\text{PO}_4^{3-}$ (*4) 100 mM $\text{Mg}^{2+}/\text{PO}_4^{3-}$. Each data point represents the average of triplicate experiments with associated standard deviation ($\sigma = 1$, shown as error bars).



4.3: Photo graph of struvite precipitated in the absence of NPs (experiment S2).

4.3.2 Nanoparticle capture by struvite

Identical to the S2 experiment all urea was first hydrolysed over a period of 24 hours. The solutions were then filtered to remove bacterial cells and amended with 10 mg/l Fe NPs. Following this, 25 mM Mg^{2+} and PO_4^{3-} was added to the struvite precipitation (N1a) experiment in 4 stages, leading to supersaturated conditions with respect to struvite, which immediately resulted in the precipitation of struvite. This is demonstrated by the trends in NH_4^+ , Mg^{2+} and PO_4^{3-} concentrations (Figure: 4.4b). Throughout the duration of the experiment NH_4^+ concentration decreased in a stepped like manner mirroring the time points at which $\text{Mg}^{2+}/\text{PO}_4^{3-}$ salts were added. With each 25 mM addition a decrease between 10 - 35% NH_4^+ was observed, resulting in the total removal of 80% NH_4^+ , initially produced by ureolysis. $\text{Mg}^{2+}/\text{PO}_4^{3-}$ trajectories, remained low throughout the duration of the experiment, indicating they were immediately removed by struvite precipitation. The final amount of NH_4^+ , Mg^{2+} and PO_4^{3-} precipitated had a stoichiometry close to 1:1:1 suggesting the precipitate was likely struvite.

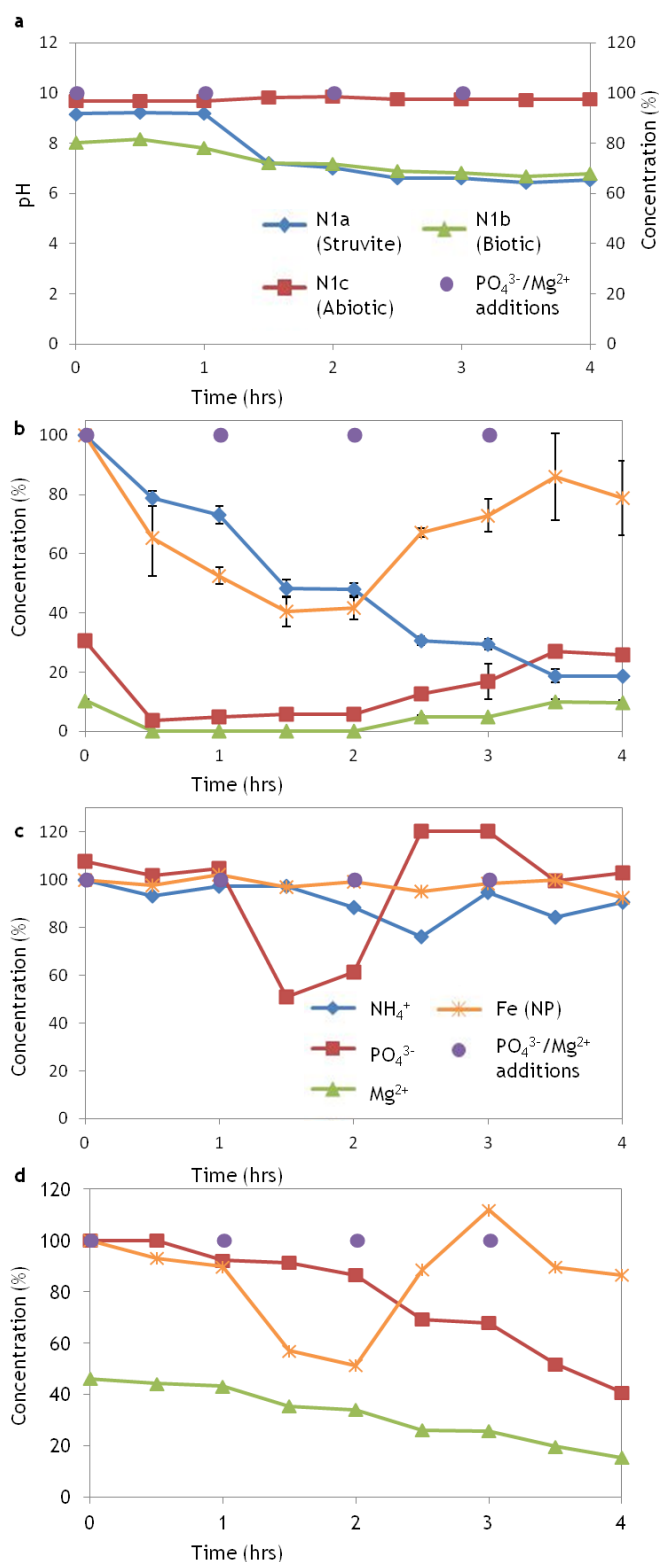


Figure: 4.4: Time series showing changes in pH, NH₄⁺, Mg²⁺, PO₄³⁻ and Fe (NP) concentration (%) for experiment N1.

(a) Change in pH for the struvite (N1a), biotic (N1b) and abiotic (N1c) experiments. (b) Experiment N1a contained 0.07 OD *S.pasteurii* and 50 mM urea, giving 100 mM NH₄⁺. Once total urea hydrolysis was achieved, bacteria were removed by filtration and 10 mg/l Fe (NPs) were injected before 25 mM MgCl₂ and K₂HPO₄ were added 4 times to give a final concentration of 100 mM; The graph shown here shows data points after total urea hydrolysis had occurred (i.e. it shows the period of time during which K₂HPO₄ and MgCl₂ were added) (c) N1b contained all components except MgCl₂; (d) N1c contained all components except bacteria and urea. The Mg²⁺/PO₄³⁻ concentration at each sample point is a percentage of the total Mg²⁺/PO₄³⁻ that was added prior to that sampling point. The purple circles represent the time points at which PO₄³⁻ and Mg²⁺ sources were added giving a total

Mg^{2+}/PO_4^{3-} concentration of (*1) 25 mM Mg^{2+}/PO_4^{3-} (*2) 50 mM Mg^{2+}/PO_4^{3-} (*3) 75 mM Mg^{2+}/PO_4^{3-} (*4) 100 mM Mg^{2+}/PO_4^{3-} . For the N1 experiment each data point represents the average of triplicate experiments with associated standard deviation ($\sigma = 1$, shown as error bars).

* Note key shown at the bottom of d refers to Figures b-d.

As struvite precipitated, the percentage of suspended NPs initially decreased similarly to the NH_4^+ trend. After the second Mg^{2+}/PO_4^{3-} injection 60% of the NPs were successfully immobilised (Figure: 4.4b). However, unexpectedly the third and fourth injections led to an increase in NP concentration by 40% despite the continuation of struvite precipitation (Figure: 4.4b). Thus, at the end of the experiment 80% of the positive NPs were re-suspended while only 20% NPs were immobilised through struvite precipitation. The re-suspension of NPs in the latter half of the experiment may be influenced by the decrease in pH over the duration of the experiment. Figure: 4.4a demonstrates that after the first Mg^{2+}/PO_4^{3-} addition little pH change was observed in the struvite precipitation (N1a) experiment. However, the second and third addition led to a pH drop from pH 9 to pH 7 and 6.5, respectively. The final addition induced little decrease in pH, remaining at around 6.5. Interestingly, the pH decrease from 9 to 7 corresponded with a slower removal of NPs: only 25% NP removal was observed compared to 35% when the pH was highest at pH 9. Critically, once the pH drops below 7, an increase in NP concentration was observed, coinciding with the re-suspension of 40% of the previously immobilised NPs. These variations in NP removal may relate to pH dependent changes in the zeta potential of the struvite surface, as discussed later in 4.3.4.

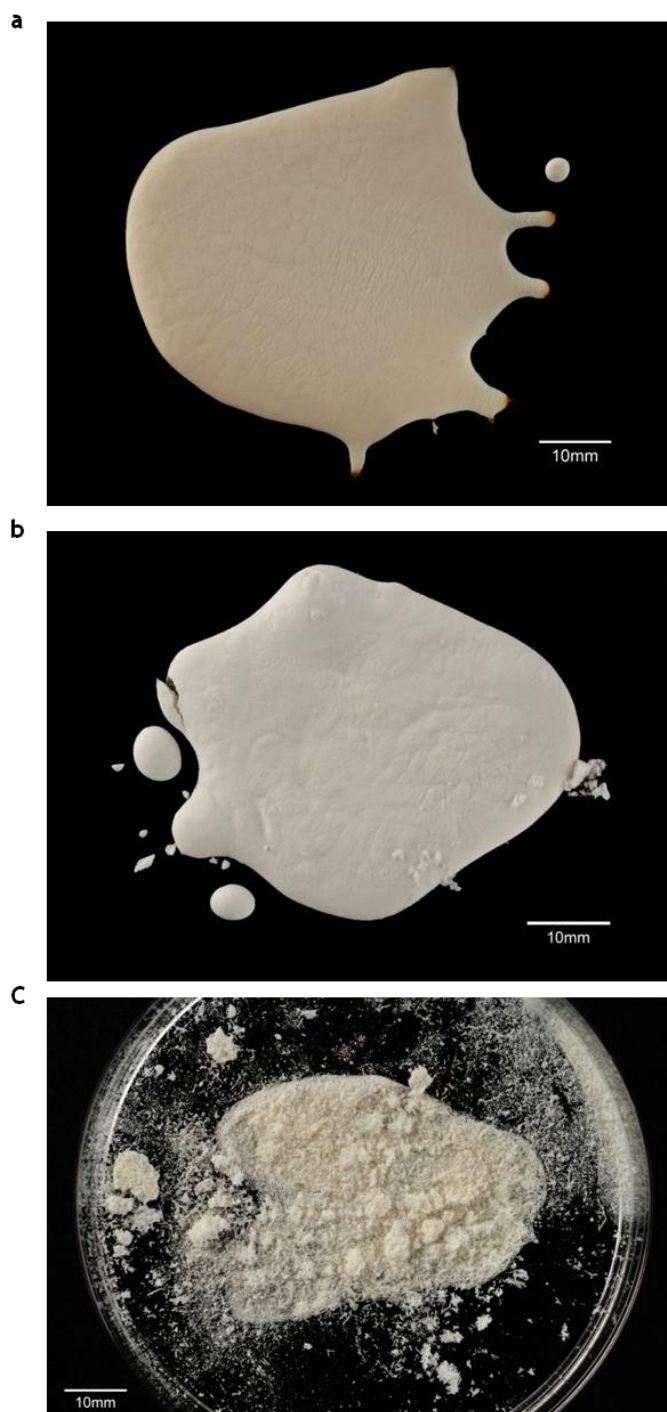
In the biotic control (N1b) experiment, NPs and ammonium were not removed during the course of the experiment (Figure: 4.4c) and no precipitates were observed. There was also no PO_4^{3-} removal by the end of the experiment (despite unexplained fluctuations). The lack of precipitate and lack of NP removal indicates NPs are not removed by, for example, aggregation or attachment to reaction vessel walls. This supports the suggestion that NP removal in experiment N1a occurred due to struvite precipitation. In the abiotic control (N1c) 85% and 58% of the added Mg^{2+} and PO_4^{3-} (respectively) were removed over the course of the experiment (Figure: 4.4d). This corresponded with the removal of 49% NPs after the second Mg^{2+}/PO_4^{3-} addition. As with the NP immobilisation experiment, N1a, the third and fourth Mg^{2+}/PO_4^{3-} additions saw

the resuspension of all the previously captured NPs. By the end of the experiments 100% of the NPs remained in solution despite the precipitation of some form of magnesium phosphate.

In order to improve NP immobilisation this experiment was re-run with the aim to maintain pH between 8 and 9, as it appeared that lower pHs may inhibit NP removal by struvite. In this experiment (N2a), struvite precipitation was more efficient, removing 92% NH_4^+ (Figure 4.6b) compared to 80% NH_4^+ in N1a experiment. Mg^{2+} and PO_4^{3-} concentrations also remained low, indicating efficient removal. Again removal of NH_4^+ , Mg^{2+} and PO_4^{3-} displayed a stoichiometry close to 1:1:1, indicating the precipitate was likely struvite. Struvite precipitation was accompanied by the removal of significantly more NPs during the first two $\text{Mg}^{2+}/\text{PO}_4^{3-}$ additions, immobilising 80% of the suspended NPs (Figure 4.6b), compared to just 60% in the N1a experiment where pH was not adjusted. However, the third $\text{Mg}^{2+}/\text{PO}_4^{3-}$ addition saw no further decrease in NP concentration, whilst the fourth saw an NP increase by 30% (Figure 4.6b). At the end of the experiment, struvite precipitation immobilised 50% of the NPs. Figure 4.6: Time series showing changes in pH, NH_4^+ , Mg^{2+} , PO_4^{3-} and Fe (NP) concentration. b portrays struvite precipitates removed after the second $\text{Mg}^{2+}/\text{PO}_4^{3-}$ injection where maximum NP removal occurred, note the dark orange-brown colour indicating the presence of NPs. Whilst Figure 4.6: Time series showing changes in pH, NH_4^+ , Mg^{2+} , PO_4^{3-} and Fe (NP) concentration. c depicts struvite precipitates removed at the end of the experiment. The struvite precipitates here are much whiter in colour indicating that less NPs are present. SEM combined with Raman analysis showed that struvite was the dominant mineral phase (Figure 4.7a and Figure 4.8a).

Again, no precipitation occurred in the biotic control (N2b; Figure 4.6c), however a small decrease in NP concentration was observed. Here, 20% NP removal was observed however as no precipitation occurred it is not clear what the removal mechanism may be (note this drop has not been seen in biotic control before). In contrast the abiotic control (N2c; Figure 4.6d) saw the precipitation of some form of magnesium phosphate. The first addition of $\text{Mg}^{2+}/\text{PO}_4^{3-}$ sources saw no decrease in $\text{Mg}^{2+}/\text{PO}_4^{3-}$, however the following additions saw a drastic decrease in $\text{Mg}^{2+}/\text{PO}_4^{3-}$ by 92%/88% respectively (Figure 4.6d). This was accompanied by the instantaneous precipitation of magnesium phosphate as indicated by the continual low levels of $\text{Mg}^{2+}/\text{PO}_4^{3-}$ concentration,

(Figure 4.6d). By the end of the experiment approximately 10% of the $\text{Mg}^{2+}/\text{PO}_4^{3-}$ ions added remained in solution (Figure 4.6d). SEM and Raman analysis was performed for these precipitates (Figure 4.7b and Figure 4.8b). Identical to the struvite precipitation experiment (N2a), this form of magnesium phosphate mineralisation concurrently removed NPs from solution in a step like manner (Figure 4.6d) throughout the duration of the experiment, producing a lightly orange coloured precipitate (4.5c). By the end of the experiment almost identical removal rates were recorded, the struvite precipitation experiment (N2a) removed 52% NPs, whilst the abiotic control which precipitated magnesium phosphate (N2c) saw the removal of 49% NPs (Figure 4.6b and d). Figure 4.7b highlights the morphological differences between the minerals struvite and magnesium phosphate sampled from these sets of experiments.



4.5: Photographs of struvite and magnesium phosphate precipitates. (a) struvite precipitate in the presence of NPs sampled after the second $\text{Mg}^{2+}/\text{PO}_4^{3-}$ addition for the N2 experiment where NP removal was greatest, (b) struvite precipitated in the presence of NPs at the end of the N2a experiment and (c) magnesium phosphate precipitated in the presence of NPs at the end of experiment N2c. Scale bar 10 mm.

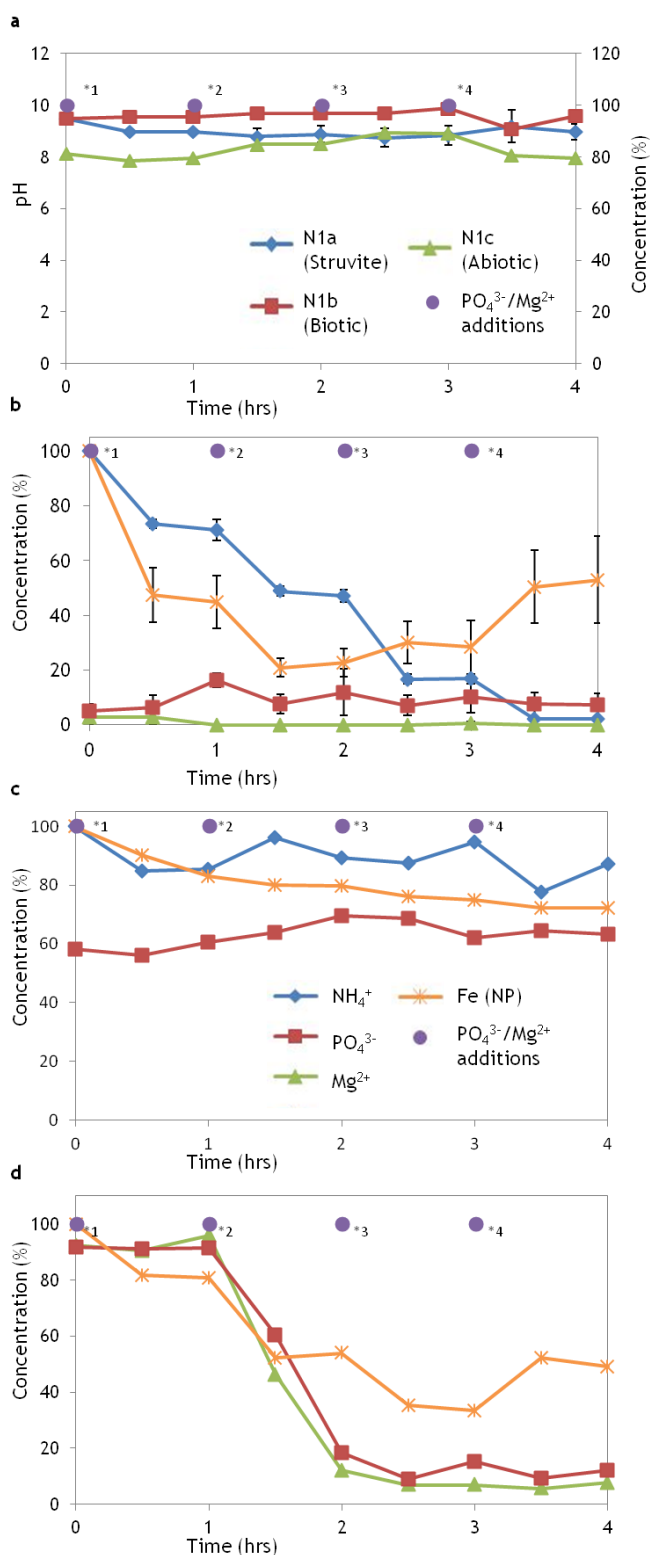


Figure 4.6: Time series showing changes in pH, NH₄⁺, Mg²⁺, PO₄³⁻ and Fe (NP) concentration. (a) Change in pH for the struvite (N2a), biotic (N2b) and abiotic (N2c) experiments. For the duration of the experiment solution pH was maintained between 8 and 9. (b) Experiment N2a contained 0.07 OD *S.pasteurii* and 50 mM urea, giving 100 mM NH₄⁺, once total urea hydrolysis was achieved 10 mg/l Fe (NPs) were injected before 25 mM MgCl₂ and K₂HPO₄ were added 4 times to give a final concentration of 100 mM; (c) N2b contained all components except MgCl₂; (d) N2c contained all components except bacteria and urea. The Mg²⁺/PO₄³⁻ concentration at each sample point is a percentage of the total Mg²⁺/PO₄³⁻ that was added prior to that sampling point. The purple circles represent the time points at which PO₄³⁻ and Mg²⁺ sources were added giving a total Mg²⁺/PO₄³⁻ concentration of (*1) 25 mM Mg²⁺/PO₄³⁻ (*2) 50 mM Mg²⁺/PO₄³⁻ (*3) 75 mM Mg²⁺/PO₄³⁻ (*4) 100 mM Mg²⁺/PO₄³⁻. For the

N2 experiment each data point represents the average of triplicate experiments with associated standard deviation ($\sigma = 1$, shown as error bars).

* Note key refers to Figures b-d.

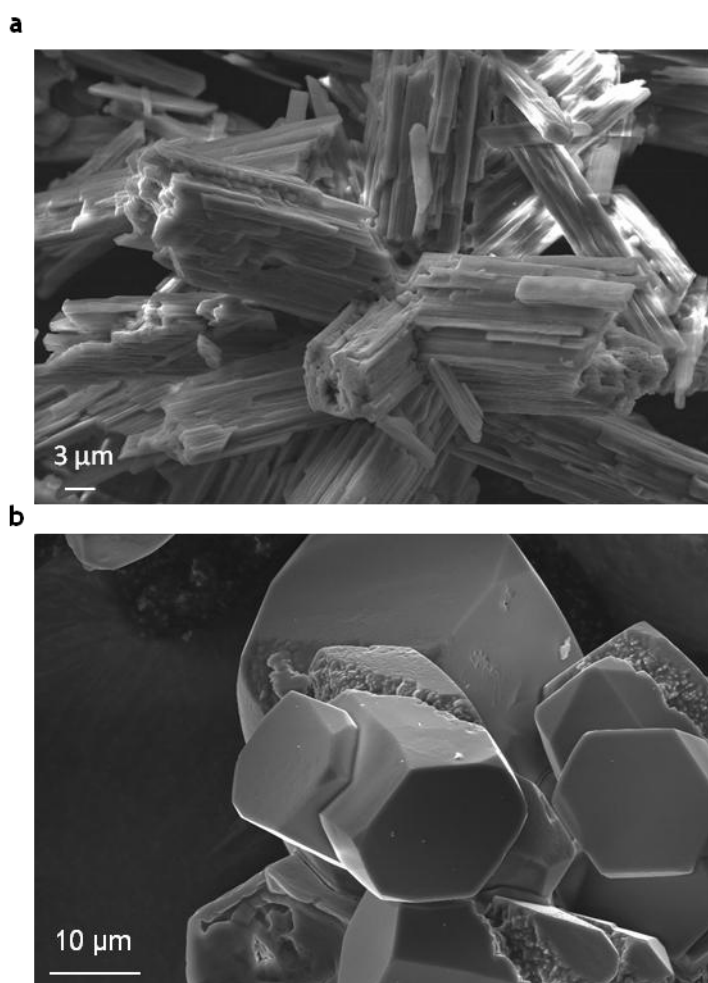


Figure 4.7: Scanning Electron Microscope (SEM) image illustrating (a) typical orthorhombic struvite crystals (scale bar 3 μm) and (b) magnesium phosphate minerals (scale bar 10 μm).

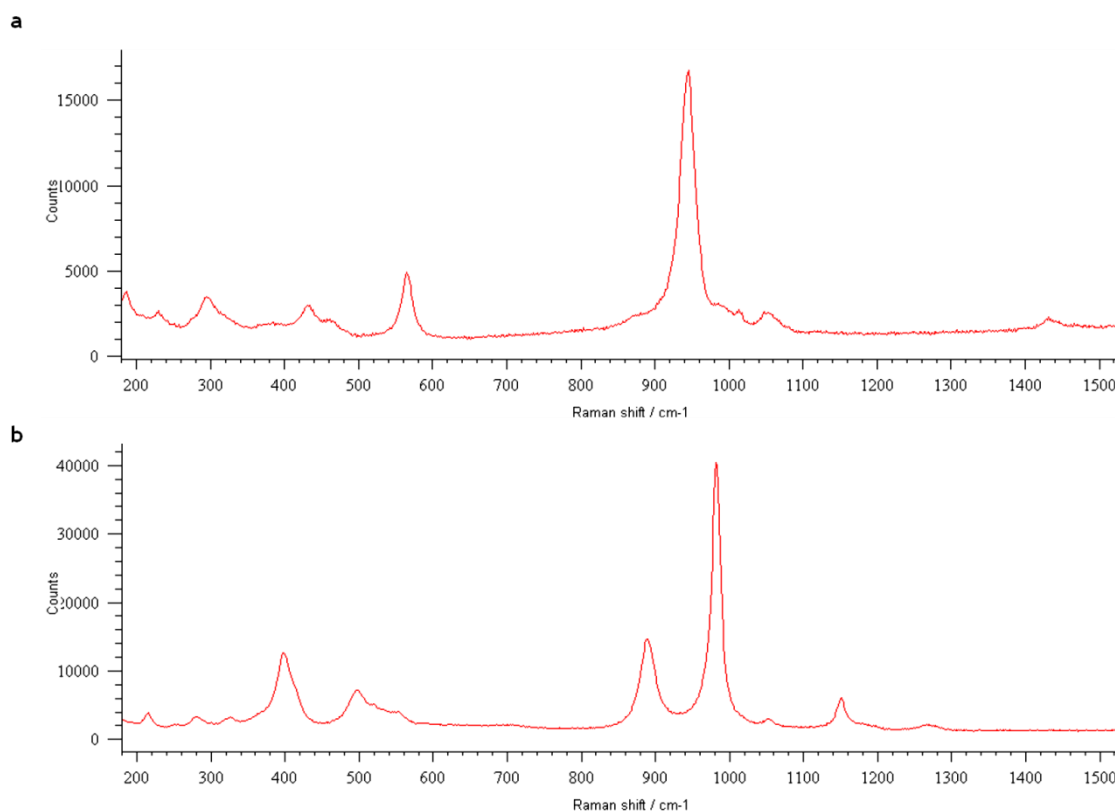


Figure 4.8: Raman spectra of struvite and magnesium phosphate minerals. (a) struvite showing a distinct single peak at 944 cm⁻¹, (b) magnesium phosphate exhibiting a peak at 983 cm⁻¹ and another smaller peak at 889 cm⁻¹.

4.3.3 Nanoparticle removal by pre-formed struvite crystals

Figure 4.9 shows the impact that ionic strength has on NP removal onto preformed struvite surfaces. Here struvite precipitates and NPs were suspended in SDW with varying KCl concentrations. Generally, increasing ionic strength resulted in a decrease in percentage of NPs attached onto the mineral surface although not in a linear fashion. Increasing the ionic strength from 50 to 150 mM KCl led to a drastic decrease in NP attachment by 15 %, while increasing the ionic strength by a further 100 mM led to little change in NP attachment, decreasing by only 1 %.

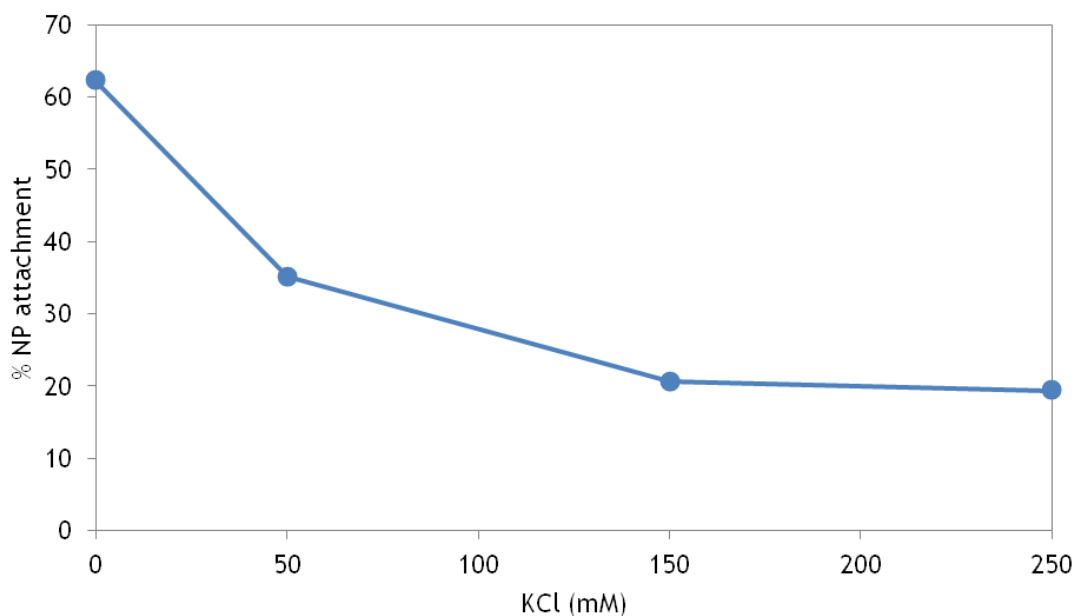


Figure 4.9: Percentage of Fe (NPs) electrostatically attached to struvite mineral surfaces when suspended in increasing concentrations of KCl.

4.3.4 Zeta potential of struvite

Zeta potential measurements were determined as a function of both pH and ionic strength (KCl concentration; KCl was used as these are the ions left in solution once struvite precipitates). Increasing ionic strength resulted in a decrease in surface charge of struvite, rendering it less negative (Figure 4.10). For example, at pH 12 struvite displayed a surface charge of -20 mV in 0 mM KCl, decreasing to -6 mV at 150 mM KCl. Furthermore, an increase in solution pH resulted in an increase in the negative surface charge of struvite. For example struvite crystals suspended in 0 mM KCl exhibited a zeta potential of -20 mV at pH 12 whilst at pH 6 this values decreased to -10 mV (Figure 4.10).

Zeta potential measurements were attempted over the pH range of 6 to 12 for ionic strengths of 0 to 200 mM KCl. However, due to particle aggregation accurate zeta potential measurements were not obtained for some of the lower pH ranges and higher ionic strengths. The dotted line on Figure 4.10 indicates conditions that induced struvite aggregation. This indicates that under these conditions the precipitates were approaching a zeta potential of zero to allow for particle aggregation. (See section 1.1.4 for further discussion on how zeta potential affects aggregation).

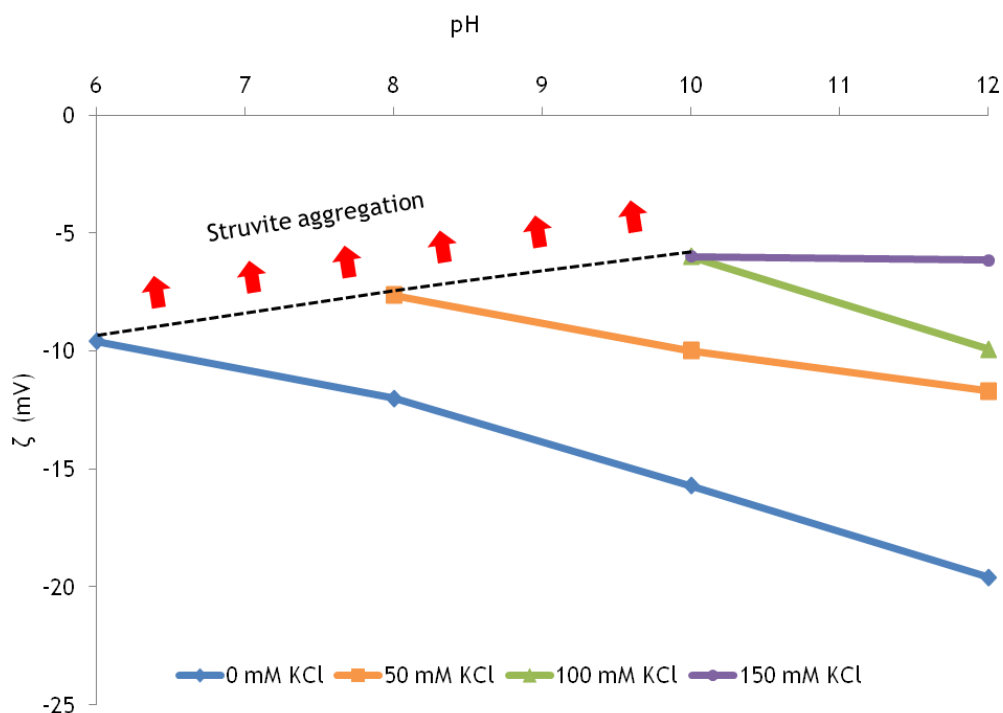


Figure 4.10: Zeta potential of struvite crystals measured as a function of pH and KCl concentration.

4.4 Discussion

In this study pH exerted a control over struvite supersaturation. In experiment S1a (where Mg^{2+} and PO_4^{3-} sources were added prior to urea hydrolysis), magnesium phosphate minerals precipitated instead of struvite, despite the production of NH_4^+ . This is due to urea hydrolysis inducing an extremely rapid pH rise from 6.5 to 8 (4.1a). Figure 4.11a, demonstrates that above pH 7.25, both struvite and magnesium phosphate minerals are supersaturated. Above pH 8 $Mg_3(PO_4)_2$ exhibits a higher saturation index than struvite (Figure 4.11a). Therefore as the reaction solution rapidly increases from 6.5 to 8, the pH where struvite exhibits the greatest saturation is passed and the system quickly enters and then remains at a pH where $Mg_3(PO_4)_2$ exhibits the greatest saturation. Hence the dominance of magnesium phosphate precipitation in this experiment. In the case of the biotic control experiment, no Mg^{2+} was added and no precipitation (e.g., struvite, Mg-phosphates) was observed (4.1b). In contrast the abiotic control (S. 1c) contains both $MgCl_2$ and K_2HPO_4 , yet magnesium phosphate precipitation did not occur. Here, due to the absence of bacteria and urea, ammonium production did not occur and thus solution pH remained low (between pH 6 and 6.6, 4.1a), keeping the solution

undersaturated (or very weakly saturated) with respect to struvite and Mg-phosphates. Figure 4.11 demonstrates that at 2 forms of magnesium phosphate are oversaturated under the experimental conditions experienced here (see Table A1 for a list of minerals which could potentially be formed from the components of the S1 experiment). $Mg_3(PO_4)_2$ saturation increases rapidly with increasing pH, being undersaturated between pH 6-7 and oversaturated above pH 7. Whilst $MgHPO_4 \cdot 4H_2O$ is oversaturated above pH 6, increasing slightly to pH 7 before levelling off. However, above pH 7.5 $Mg_3(PO_4)_2$ is far more oversaturated than $MgHPO_4 \cdot 4H_2O$ precipitation. Experiment S1a exhibited a pH of above 8 where $Mg_3(PO_4)_2$ is extremely oversaturated, hence, this form of magnesium phosphate should preferentially be precipitated over $MgHPO_4 \cdot 4H_2O$. However, 4.1b demonstrates an almost identical decrease in Mg^{2+} and PO_4^{3-} (i.e. a near 1:1 stoichiometry) which would suggest the formation of $MgHPO_4 \cdot 4H_2O$. If $Mg_3(PO_4)_2$ was precipitated one would expect the removal of more Mg^{2+} relative to as PO_4^{3-} in order to successfully precipitate $Mg_3(PO_4)_2$. In addition no magnesium phosphate precipitation occurred in the abiotic control despite $MgHPO_4 \cdot 4H_2O$ being oversaturated (experimental pH remained above pH 6). Without further in-depth analysis it is difficult to say which form of magnesium phosphate is precipitated here. However as magnesium phosphate precipitation was found to be pH dependant it is likely $Mg_3(PO_4)_2$ and that the decrease in PO_4^{3-} was not highlighted possibly due to experimental error.

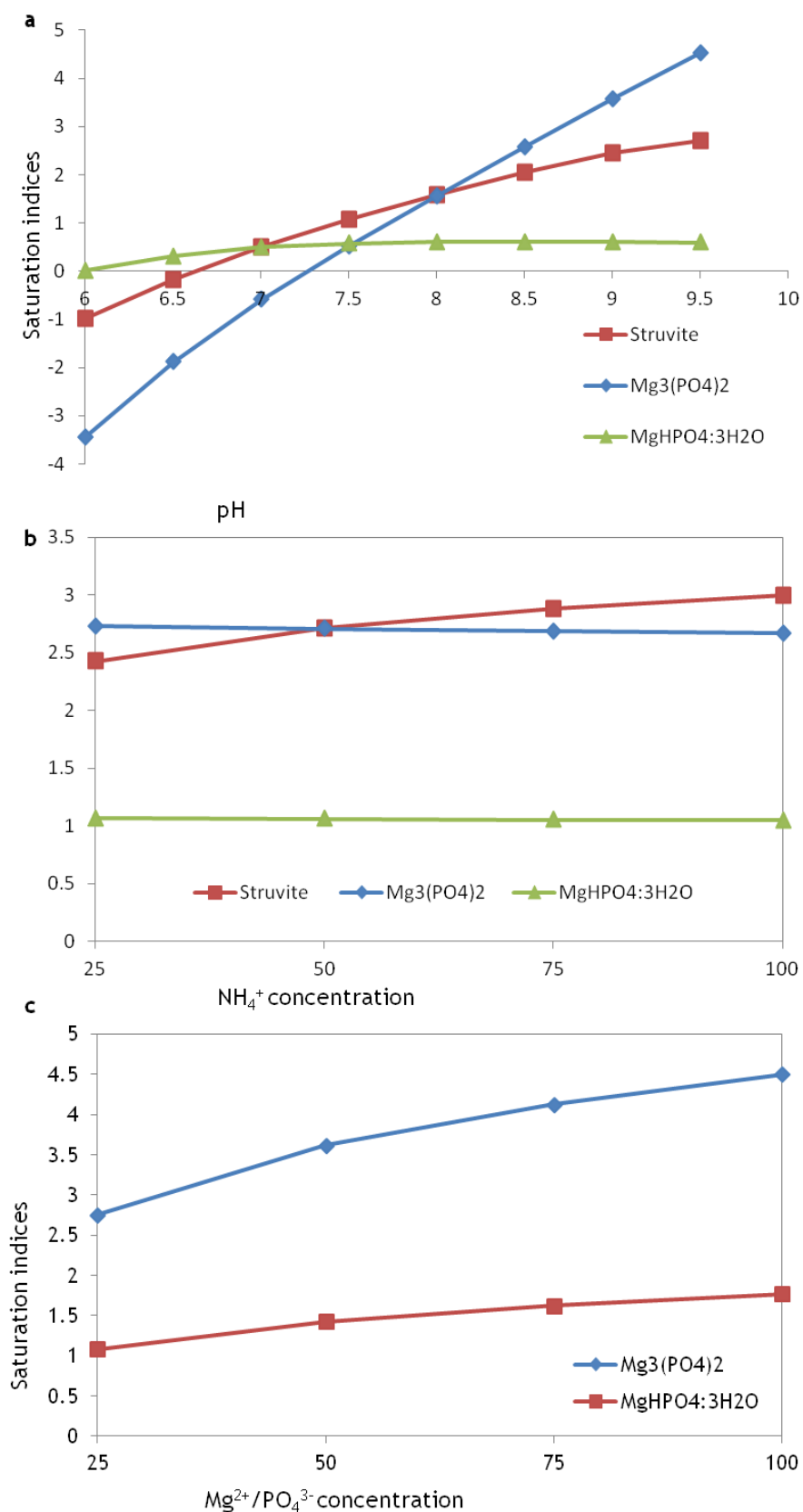


Figure 4.11: Saturation index values for Mg₃(PO₄)₂, MgHPO₄:3H₂O and struvite. (a) 10 mM NH₄⁺, Mg²⁺ and PO₄³⁻ as a function of pH (b) as a function of increasing NH₄⁺ (this is to replicate the S2a experiment, here NH₄⁺ increases but Mg²⁺ and PO₄³⁻ remain at 25 mM as these sources are immediately removed via struvite precipitation) and (c) as a function of increasing Mg²⁺ and PO₄³⁻ concentration (as to replicate experiment S2c). Visual MINTEQ, version 3.0.

In order to promote struvite precipitation more NH_4^+ ions must be present relative to Mg^{2+} and PO_4^{3-} to ensure struvite exhibits a higher saturation index than magnesium-phosphate (as in experiment S2). Figure 4.11b demonstrates that at >50 mM NH_4^+ struvite exhibits a higher saturation index than magnesium phosphate at pH 8. Below this threshold, theoretically, magnesium phosphate minerals should preferentially precipitate over struvite. Notably, however, Figure 4.2 demonstrates that all of the 100 mM NH_4^+ produced by ureolysis was removed by struvite precipitation. This is surprising as one may expect struvite precipitation to occur until just under 50 mM NH_4^+ is left in solution, at which point Mg-phosphate would precipitate. A possible explanation for the total removal of NH_4^+ may be that preformed struvite crystals already exist, acting as templates for the precipitation of struvite rather than magnesium phosphate.

Struvite precipitation was extremely effective in removing positively charged NPs from solution during the initial stages of the experiments. However, by the third $\text{Mg}^{2+}/\text{PO}_4^{3-}$ addition, i.e., precipitation event, NP resuspension occurred. As with a calcite precipitating system electrostatic interactions control the success of NP immobilisation (Chapter 2). However, the re-suspension of NPs elucidates an important process of NP immobilisation via struvite precipitation. In both cases NPs are electrostatically attracted to the mineral surface. However, the ability of NPs to be released at increasing ionic strength and decreasing pH in the struvite system, suggests they are merely attached to the struvite surface, rather than occluded within the struvite crystal. This is likely because the calcite precipitating system is driven during bacterial ureolysis, and so the process of precipitation is much slower. Slower mineral growth allows the NP to be overtaken by the advancing solidification front, entrapping the NP within the mineral precipitate. Conversely, the struvite precipitation system developed and applied here leads to instantaneous homogeneous nucleation of struvite crystals through which struvite precipitation was observed within matter of seconds (after $\text{Mg}^{2+}/\text{PO}_4^{3-}$ additions). As such NPs have not had time to attach and become occluded within the quickly forming crystals. Instead NPs simply sorb onto the surface of the mineral once they formed and start to settle out. This process occurs with every addition of $\text{Mg}^{2+}/\text{PO}_4^{3-}$, initiating struvite precipitation followed by NP sorption. This occurs until a certain pH/ionic strength is reached where the mineral and NP surface

charge are dulled to the point where NPs are no longer attracted to the mineral surface, and start to desorb.

This phenomenon is demonstrated by the changes in pH induced by the removal of NH_4^+ via struvite formation induced by the addition $\text{Mg}^{2+}/\text{PO}_4^{3-}$ salts (Figure: 4.4a). In the N1a experiment the solution pH decreased from pH 9 at the start of the experiment to pH 6.5 after the removal of 82% NH_4^+ (Figure: 4.4a). Solution pH has long been known to exert a strong control on mineral surface charge in aqueous solution (Van Cappellen et al., 1993, Carre and Lacarriere, 2006, Hazen and Sverjensky, 2010). Typically, at lower pH mineral surfaces become protonated, thus becoming increasingly positively charged (or less negatively charged). Conversely, with increasing pH mineral surfaces become progressively more negative due to deprotonation (Hazen and Sverjensky, 2010). This is demonstrated by Figure 4.10. Here the zeta potential of struvite decreases from -20 mV to -10 mV when the pH of the solution is reduced from pH 12 to 6 respectively (when suspended in 0 mM KCl). With this the mineral becomes less negative, resulting in a weakening of the electrostatic attraction of the positively charged NP to the mineral surface and thus facilitating the release of nanoparticles back into solution. It should be noted here that the amine groups on the positively charged nanoparticle likely exhibit pKa's between 8-9 (Phoenix et al., 2002). From this we can approximate that as pH drops through pH 8 or 9, the amine groups are protonating and becoming more positively charged. This may counteract the loss of negative charge on the struvite, to assist electrostatic attraction, although evidently not sufficiently enough to prevent NP remobilization.

With the aim of increasing the electrostatic attraction between the positively charged NP and the negatively charged mineral surface, the NP immobilisation experiments were repeated with solution pH controlled between pH 8-9. Maintaining a high pH showed a marked improvement by enhancing NP removal by 30%. This is likely due to an increased surface charge on the mineral (struvite) surface enhancing electrostatic attraction (this also indicates that at these pHs the NP was still positively charged and had not deprotonated). However, this increase in NP capture may also be attributed to the formation of a larger mineral surface area, due to the formation of more crystallites. As pH increases, the saturation index for struvite also increases (Figure 4.11a), and so at pH 9, 98% of the NH_4^+ produced by ureolysis was removed through struvite

precipitation compared to 80% when the pH dropped below 7 (compare Figure 4.4b and Figure 4.6b). Here, an increase in the mineral surface area available for NPs to attach may also explain the increase in NP immobilisation. Either way, a higher pH was favourable for increased NP attachment.

Intriguingly, despite maintaining a high pH NP re-suspension still occurred. Aside from pH, solution ionic strength also exerts a strong control on surface charge with increasing ionic strength reducing surface charge (see Chapter 1.1.3). Here, it is the increase in ionic strength, which accounts for the re-suspension of NPs in the NP immobilisation experiment (N2a, Figure 4.6b). Each addition of Mg^{2+}/PO_4^{3-} leads to an increase in the ionic strength of the solution, as the K^+ and Cl^- ions are left over from the added salts, ($MgCl_2$ and K_2HPO_4) whilst Mg^{2+} and PO_4^{3-} ions are removed by struvite precipitation. With each addition, dissolved K^+ and Cl^- concentration increases by 50 mM, giving a final concentration of 200 mM KCl. Increasing solution ionic strength results in a decrease in the EDL for the mineral surface and the NP, weakening the electrostatic attraction between these two surfaces leading to the re-suspension of previously immobilised NPs. Figure 4.10 highlights this phenomenon. Here preformed struvite precipitates were suspended in 50, 100, 150mM and 200 mM KCl and zeta potential was measured using Zeta Potential Analyser (Zetasizer Nano ZS, Malvern). With increasing KCl concentration the zeta potential of the mineral surface decreased from -20 to -6 with an increase in KCl from 0 to 150mM KCl respectively when measured at pH 12. Figure 4.6b shows significant re-suspension of NPs after the final addition of Mg^{2+}/PO_4^{3-} , here the concentration of K^+ and Cl^- increases from 150 to 200 mM, with this final addition a tipping point is reached, compressing the EDL to such an extent that NPs are no longer bound to the mineral surface by electrostatic attraction. This is further confirmed by Figure 4.10 as an accurate zeta potential measurement could not be obtained at this ionic strength and pH (200 mM KCl, pH 8-9) due to aggregation of struvite crystals. This indicates that the precipitates were approaching a zeta potential of zero which led to particle aggregation (during the zeta potential measurement) and resuspension of NPs (in the NP immobilisation experiments). The role that ionic strength plays in influencing the sorption of NP onto the mineral surface is displayed in Figure 4.9 which shows NP sorption onto struvite. Here, with increasing ionic strength the percentage of attached NPs decreases.

The potential for NP attachment to struvite precipitates was modelled using the classical Derjaguin-Landau-Verwey-Overbeek (DLVO) model. This is described in full in Chapter 2.6. The tested parameters used are identical for those used in Chapter 2 aside from the Hamaker constant for struvite (A_{22}) which was calculated as 1.54×10^{-20} using the Hamaker constant calculator published by Overney (2009), see Appendix B. This generates a combined NP-struvite-water (A_{132}) Hamaker constant of -1.58×10^{-20} . The DLVO model was run for the N2 experiment where the pH was maintained between pH 8 and 9. Figure 4.12 demonstrates interaction energy profiles between the positively charged NPs and the negatively charged struvite precipitates. Here, a repulsive van der Waals interaction is counteracted by an attractive electrical double layer resulting in a complex total interaction energy profile (Figure 4.12). As the two surfaces approach, a small repulsive energy exists. Once this repulsive interaction energy is passed an attractive well exists at less than 5 nm separation distance. This results from the dominance of the attractive electrical double layer, that is, until a few 10ths of an nm are reached where a very strong repulsive interaction energy exists due to the dominance of the repulsive van der Waals interaction. The Debye length used for Figure 4.12 was calculated based on the second $\text{Mg}^{2+}/\text{PO}_4^{3-}$ addition, i.e. 50 mM KCl and 75 mM NH_4^+ . Under these conditions NP sorption onto struvite precipitates is observed. Based on the DLVO model observed here, this would suggest NPs are attached due to the small energy well. Whilst Figure 4.13 demonstrates that with increasing ionic strength (due to the addition of K^+ and Cl^- ions left over from the added salts, MgCl_2 and K_2HPO_4) the depth of the attractive energy well decreases until at 200 M/m³ the total interaction energy profile becomes repulsive. This agrees with what is observed experimentally for the N2a experiment where after the final $\text{Mg}^{2+}/\text{PO}_4^{3-}$ addition NP concentration increased by 30% Figure 4.6b. Confirming that increasing solution ionic strength results from a weakening of the electrostatic attraction resulting from the attractive EDL between the mineral and the NPs, leading to the re-suspension of previously immobilised NPs. Overall, the DLVO model produced here is interesting in that the interaction energies are largely repulsive (apart from the energy well), despite NP and mineral surfaces exhibiting opposite charges. This repulsive interaction energy results from a negative combined Hamaker constant (A_{132}) of -1.58×10^{-20} produced from the interaction of the positively charged NPs, struvite precipitates and the dispersing medium

(water). As the Hamaker constant is a measure of the strength of the van der Waals force, a negative Hamaker constant results in a positive van der Waals interaction, thus producing a repulsive van der Waals interaction which dominates over the attractive EDL interaction.

Table 4.2 Summary of the experimental parameters for each Mg^{2+}/PO_4^{3-} addition

NH_4^+ (mM)	KCl (mM)	Total ionic strength (M/m^3)	Inverse Debye length (M/m^2)
75	50	87.5	$9.63 \times 10^{+08}$
50	100	125	$1.15 \times 10^{+09}$
25	150	162.5	$1.31 \times 10^{+09}$
0	200	200	$1.46 \times 10^{+09}$

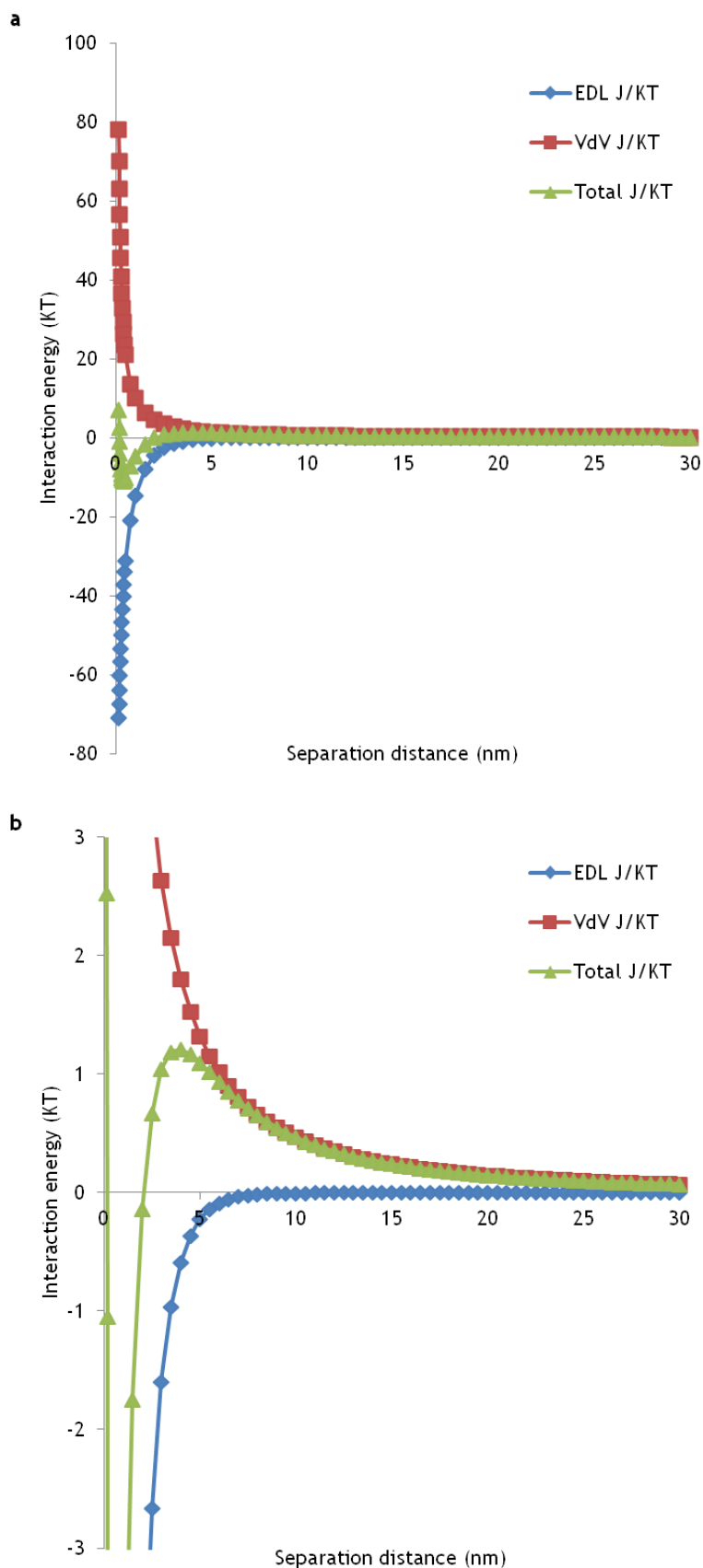


Figure 4.12 Interaction energy profiles calculated for the positively charged NPs and the negatively charged struvite surfaces (using a Hamaker constant for struvite of 1.54×10^{-20}). Note (b) is an enlargement of graph (a).

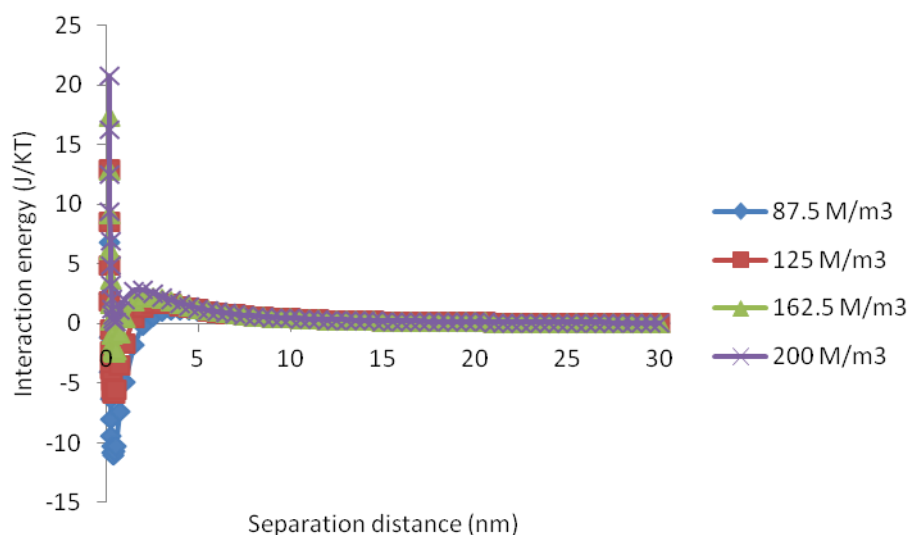


Figure 4.13: Total interaction energy profile for positively charged NPs interacting with struvite surfaces as a function of increasing KCl concentrations from 87.5 to 200 M/m³.

Unexpectedly the abiotic control resulted in the precipitation of magnesium phosphate minerals in both NP immobilisation experiments (N1c and N2c). Here, with every addition of Mg^{2+}/PO_4^{3-} magnesium phosphate is becoming increasingly oversaturated, (Figure 4.11c) resulting in the precipitation of magnesium phosphate. The precipitation of magnesium phosphate also resulted in a decrease in NP concentration, indicating the magnesium phosphate also exhibits a negative surface charge and thus can capture NPs. As with the struvite precipitating system, NP resuspension occurred in the latter half of the experiment for the first NP immobilisation experiment, N1c (Figure: 4.4d). This suggests NPs were captured by surface adsorption rather than occlusion. Here, all of the immobilised NPs desorbed from the Mg-phosphate mineral surfaces resulting in no NP removal by the end of the experiment. However, in the second NP immobilisation experiment, N2c, maintaining solution pH between 8 and 9 showed a noticeable improvement in NP capture. By the third addition 65% NPs were removed by electrostatic attraction onto the Mg-phosphate surfaces (Figure 4.6d). However, with the fourth addition 15% of the adsorbed NP desorbed again, resulting in the immobilisation of 49% NPs (Figure 4.6d). Under these conditions almost identical rates of NP immobilisation occurred under both the struvite (immobilised 52% NPs) and magnesium phosphate (immobilised 49% NPs) precipitation systems.

4.5 Conclusion

Struvite has shown to not only immobilise positively charged NPs from solution but also successfully remove close to 100% NH_4^+ produced by bacterial ureolysis. NP immobilisation was found to be highly dependent on both pH and ionic strength. Maintaining solution between pH 8 and 9 showed a marked improvement in NP immobilisation, removing 80% Fe NPs. However once the ionic strength exceeds 100 mM KCl NP resuspension occurs, indicating that NPs are reversibly attached to the mineral surface by electrostatic attraction. Under certain environmental conditions struvite may be used as a tool to immobilise toxic NPs from environmental and wastewater treatment systems.

5 Bacterial biosorption of nanoparticles

5.1 Summary

Bacteria and biofilms are widely used to adsorb and degrade numerous contaminants and are commonly used as a treatment step in many wastewater treatment plants. Here, we test the ability of *B. subtilis*, a common groundwater bacterium, and wastewater treatment biofilms to adsorb and remove NPs from solution. Both biosorbent materials were highly efficient at removing positively charged NPs from solution, while failed to adsorb negatively charged NPs. Adsorption of positive NPs onto *B. subtilis* was found to be dependent on pH, with greater adsorption at higher pH. This pH dependence must result from the greater negative surface charge exhibited by bacteria at higher pH. Desorption studies, however, revealed adsorption was only partly reversible. In addition, the presence of slower adsorption kinetics in biofilms compared to planktonic biofilms suggests diffusion of NPs through the porous structure of the biofilm. Overall, these findings highlight that planktonic bacteria and biofilms are highly efficient biosorbents for NPs, this holds implications for NP transport in environmental systems and through wastewater treatment plants.

5.2 Introduction

The ability for bacteria to adsorb/immobilise NPs from solution was briefly highlighted when testing the ability of bacterially driven solid phase capture to immobilise NPs (Chapter 3). Here, positively charged NPs (S-posNPs) were shown to adsorb onto the negative bacterial surface of *S. pasteurii* while negatively charged NPs (S-negNPs) remained in suspension. To date, a significant amount of geomicrobial research has focused adsorption of cations by bacteria (Gorman-Lewis et al., 2005, Yee and Fein, 2001, Yee et al., 2004, Ngwenya et al., 2003, Small et al., 2001, Fein et al., 1997). Despite this, the potential for bacteria to adsorb nanoparticles (NPs) has received little attention.

Bacteria, ubiquitous to all ecosystems, have the ability to adsorb an array of cations from environmental systems. The cell wall of gram positive bacteria contain several organic functional groups; such as amine, carboxyl, hydroxyl and phosphoryl groups (Fein et al., 1997). The ionisation of these proton active

functional groups (namely carboxyl, phosphoryl and hydroxyl functional groups) creates a negative charge which surrounds the cell (Yee et al., 2004). The electric field surrounding the bacterium determines the distribution of the ions and counterions at the cell-water interface, strongly influencing the metal binding capacity of the cell wall (Yee et al., 2004). Potential bacterial biosorbents include the genre of *Bacillus*, *Pseudomonas* and *Streptomyces* (Vijayaraghavan and Yun, 2008). Such biosorbents have the ability to bind significant quantities of toxic metals from environmental systems, for example Ziagova (2007) saw the successful biosorption of 278 mg g^{-1} cadmium by the organism *Pseudomonas sp.*

Currently municipal wastewater treatment plants (WWTP) take advantage of the biosorbent properties of bacteria, using them as part of their treatment system. Biofilm reactors such as fluidised beds, up flow sludge blankets and granular sludge blankets contain dense bacterial flocs (activated sludge) which sorb and degrade an array of pollutants (Nicolella et al., 2000, Lazarova and Manem, 1995, Vijayaraghavan and Yun, 2008). Bacterial flocs or granules are capable of operating both anaerobically and aerobically. Anaerobic granulation has been extensively studied and is most commonly used by wastewater treatment plants (Liu et al., 2004, Liu and Tay, 2004). Hence, in this study only anaerobic granules were tested. Biogranules are more complex than their single celled counterparts, being composed of multiple communities bound by extracellular polymeric substances (EPS) via a process of self immobilisation (Liu and Tay, 2004). The process of self immobilisation is initiated by the introduction of inorganic nuclei and is carefully controlled by the reactors operating conditions (Tay et al., 2004, Liu and Tay, 2004). In addition the filamentous bacterium *Methanotrix* has been suggested to play a key role in binding the microbial components together, creating a dense floc composed of millions of organisms per gram of biomass (Quarmby and Forster, 1995, Liu and Tay, 2004). Flocs offer key advantages, such as high biomass retention, cell-liquid separation via sedimentation and can withstand high-strength wastewater and shock loadings due to their regular, dense and strong structural properties (Nicolella et al., 2000, Liu and Tay, 2004). With the increasing use of nanomaterials, WWTPs are likely to play a key role in determining pathways for NP pollutants. Indeed Kiser et al. (2010) reports the detection of titanium dioxide NPs of up to $3000 \mu\text{g Ti/L}$ in raw sewage at a full scale municipal WWTP in Arizona (USA). Kiser et al.

(2009) analysed effluent samples collected from each unit process at four different times (7:00, 11:00, 15:00 and 18:00) each day in June. From this Keiser et al. (2009) found that on average $79\% \pm 23\%$ of the titanium dioxide NPs that entered the plant were removed from the wastewater via biosorption to activated sludge. Despite this, environmentally relevant concentrations of up to $100 \mu\text{g/L}$ Ti NPs were discharged to surface waters (Kiser et al., 2009).

In this study we investigate the potential for the gram positive bacterium *B. subtilis* and wastewater bacterial flocs to immobilise (adsorb) positively charged and negatively charged NPs. The sorption of NPs is examined as a function of bacterial concentration, pH and ionic strength.

5.3 Materials and Methods

5.3.1 Nanoparticles

The negatively and positively charged NPs (S-neg and S-pos respectively) were used in this study. Further details of NPs used here can be found in Chapter 2.3.1.

5.3.2 *Bacillus subtilis* adsorption experiments

5.3.2.1 Growth of Culture

B. subtilis cells cultures were grown from trypticase soy broth, at 30°C for 24 hours on a rotary shaker at 120 rpm. After incubation, cells were harvested by centrifugation and washed 4 times in sterile deionised water before resuspension in 1, 10 or 100 mM NaCl to the desired optical density (OD, either 0.25 or 0.5 OD) as determined spectrophotometrically at 600 nm.

5.3.2.2 Bacterial concentration dependant adsorption experiments

NP binding experiments were first preformed as a function of bacterial concentration. Bacterial suspensions were prepared at a concentration of 0.5 and 1 OD and then mixed at a ratio of 1:1 with 20 mg/l NPs suspended in 20 mM NaCl. The final concentrations were 0.25 or 0.5 OD *B. subtilis*, 10 mM NaCl and 10 mg/l NPs (S-neg or S-pos NPs). A control was also run containing NPs suspended in 10 mM NaCl. The analyses of NP concentration (using Fe as a proxy for NP concentration) were determined at time zero and regular intervals thereafter.

5.3.2.3 pH and ionic strength dependant adsorption experiments

NP sorption experiments were performed as a function of pH (pH 2-10) in 1, 10 and 100 mM NaCl. A bacterial concentration of 0.25 OD and the S-pos NP were chosen for the pH experiments. The pH of the bacterial solution was adjusted using NaOH and HCl before addition of the NP-NaCl solution and left to react for 90 minutes before sampling (this sample period was chosen based on the kinetic data obtained from experiments presented in section 5.4.1.1. Note that the experiments were performed as batch reactions (each analysed pH is an individual experiment).

5.3.2.4 Desorption experiments

Desorption experiments were performed to determine the reversibility of NP adsorption onto the surface of *B. subtilis*. The pH of the bacterial - NaCl solution was adjusted to pH 10 using NaOH before addition of NPs. The solution was left to react for 20 minutes before the pH was dropped using HCl in a stepwise fashion, sampling at every pH, until pH 2.

5.3.3 Wastewater biofilm adsorption experiments

5.3.3.1 Wastewater Biofilm samples

Anaerobic wastewater biofilms were sampled from 485 m³ expanded granular sludge bed treating distillery wastewater in Edinburgh, UK. The Biofilm flocs ranged from 1 to 3 mm in diameter and were composed of an agglomeration of several bacterial species (Figure 5.1). Biofilm flocs were washed 4 times with sterile deionised water SDW to remove any impurities.



Figure 5.1: Image of wastewater biofilm flocs.

5.3.3.2 Concentration dependant adsorption experiments

NP binding experiments were first performed as a function of biofilm concentration. Two and 4 g of biofilm (wet weight) were weighed and added to 10 mg/l S-pos NPs suspended in 10 mg/l NaCl. The biofilm-NP solutions were gently agitated on a rotary shaker at 50 rpm to ensure the biofilm flocs remain in suspension throughout the duration of the experiment, yet remained intact. The analyses of Fe (NP) concentration were determined at time zero and regular intervals thereafter.

5.3.3.3 pH and ionic strength dependant adsorption experiments

NP adsorption experiments were then performed as a function of pH (pH 3-10) in 1, 10 and 100 mM NaCl. pH and ionic strength dependent adsorption experiments were not performed at pH 2 due to the release of Fe (possibly obtained from the distillery) from the biofilm under such acidic conditions. A biofilm concentration of 2 g was chosen for the pH dependant experiments. The biofilm samples were suspended in the desired NaCl solutions and the pH of the solution was adjusted using NaOH and HCl. Once the desired pH was reached, 10 mg/l Fe NPs were directly added to the biofilm-NaCl solution and left to react for 90 minutes before sampling. The biofilm-NP solutions were gently agitated on a rotary shaker at 50 rpm to ensure the biofilm flocs remain in suspension

throughout the duration of the experiment. Note that each pH is an individual experiment (i.e. batch reaction).

A summary of all the tested experimental conditions can be seen in

Table 5.1.

5.3.4 Chemical analysis

At each sampling time 5 ml aliquots were removed from the experiment. After pH measurement 3 ml of the sample was mixed with 1 ml 50% HCl for Fe (NP) measurement by atomic absorption spectroscopy.

5.3.5 Transmission Electron Microscopy (TEM)

Bacteria and biofilms were examined by Transmission Electron Microscopy (TEM) to confirm the presence of attached nanoparticles. After reaction with NPs, bacteria and biofilms were first fixed overnight in 2.5% glutaraldehyde in 0.05M HEPES buffer at pH 7. These were then washed in phosphate buffer three times, dehydrated through an ethanol series (30%, 50%, 70%, 90%, 4x100%), then embedded in Epon812 resin and cured at 60°C. Once the resin had cured, samples were sectioned into ultra-thin sections using a diamond knife and ultramicrotome. Note that during processing samples were split into three groups to receive different levels of contrast staining. One set was pre-stained with 1% Osmium tetroxide (1 hour) followed by post-staining with 2% uranyl acetate (1 hour). A second set was only post-stained in uranyl acetate, while a third set was not stained at all. Note that pre-staining occurs before embedding in resin, while post-staining occurs after the embedded samples have been microtomed into ultra-thin sections. Different levels of staining were done to provide different levels of contrast in the TEM. Staining is useful as the heavy metal stains bind to the bacterial cell, giving it contrast in TEM and thus making cells easier to see. However, as the NPs have magnetite cores, this mineral will already exhibit strong contrast and thus NPs will be easily visible, and indeed easier to spot, without staining. Sections were viewed on a FEI Tecnai T20 TEM operating at 120 kv.

Table 5.1: Summary of tested experimental conditions.

Run*	Bacterial concentration (OD ₆₀₀ or g)**	NaCl (mM)	pH	NP (mg/l)
<i>Bacillus subtilis</i> experiments				
Bs1	0.25	10	-	10 (S-pos)
	0.5	10	-	10 (S-pos)
	0.25	10	-	10 (S-neg)
	-	10	-	10 (S-pos)
Bs2	0.25	1	2-10	10 (S-pos)
	0.25	10	2-10	10 (S-pos)
	0.25	100	2-10	10 (S-pos)
Bs3	0.25	10	2-10	10 (S-pos)
Wastewater Biofilm experiments				
WB1	2	10	-	10 (S-pos)
	4	10	-	10 (S-pos)
	8	10	-	10 (S-pos)
	-	10	-	10 (S-pos)
WB2	2	1	3-10	10 (S-pos)
	2	10	3-10	10 (S-pos)
	2	100	3-10	10 (S-pos)

*Bs1 is the concentration dependant adsorption experiment, Bs2 is the pH and ionic strength dependant adsorption experiment and Bs3 represents the desorption experiment for *Bacillus subtilis* whilst WB1 is the concentration dependant adsorption experiment and WB2 is the pH and ionic strength dependant adsorption experiment for the wastewater biofilm flocs.

** Bacterial density is OD₆₀₀ for *B. subtilis* experiments and grams (wet weight) for biofilm experiments

5.4 Results

5.4.1 *Bacillus subtilis* adsorption experiments

5.4.1.1 Concentration dependant adsorption experiments with *B. subtilis*

NP adsorption experiments (Bs1) were first tested as a function of time with the gram positive bacteria *B. subtilis*. In experiments containing S-pos NPs, NP adsorption occurred within 10 minutes (Figure 5.2). Increasing the bacterial concentration from 0.25 OD to 0.5 OD resulted in an increase in the percentage of NPs adsorbed from 71% to 100% respectively (Figure 5.2). In both experiments,

further NP sorption was minimal after the first sampling point (10 minutes). In contrast S-negNP adsorption fluctuated between 0-10%, almost identical to the blank (containing S-pos NPs only) experiment (Figure 5.2).

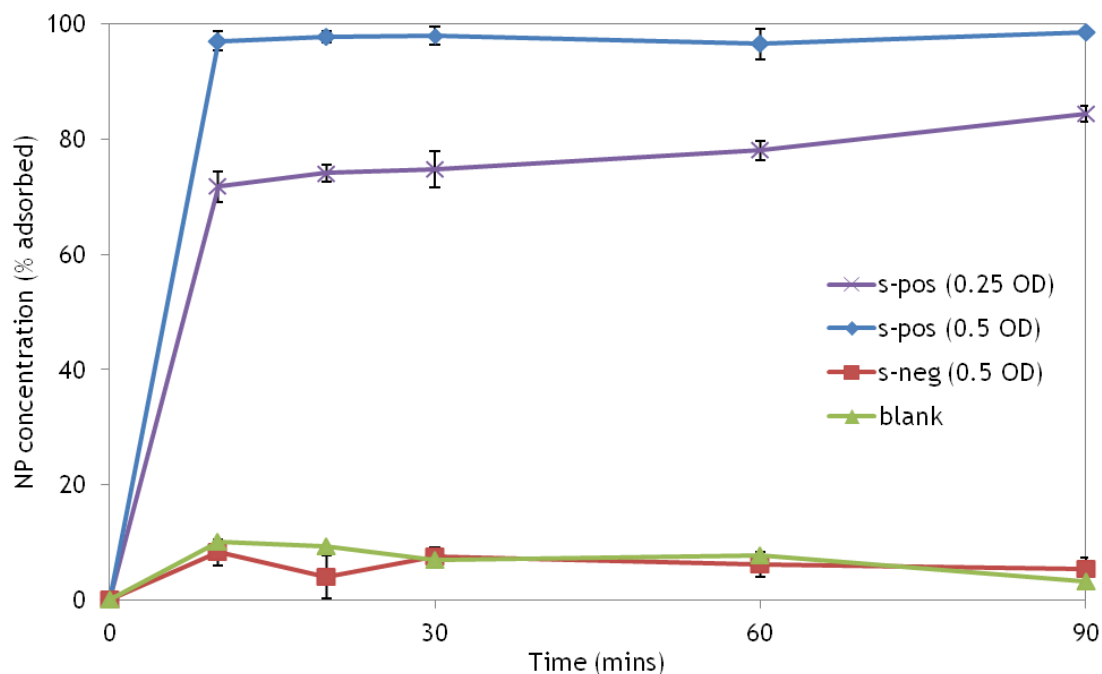


Figure 5.2: Percent NPs adsorbed by *B. subtilis* as a function of time in 10 mM NaCl. Concentrations of 0.25 OD (blue diamond's) and 0.5 OD (purple crosses) were chosen for concentration dependant analysis of the sorption of S-pos NP suspended in 10 mM NaCl. The sorption of S-neg NPs was also tested (red squares) for a concentration of 0.5 OD *B. subtilis*. A blank experiment (green triangles) containing S-pos NPs without bacteria was also run. Each data point represents the average of triplicate experiments with associated standard deviation ($\sigma = 1$, shown as error bars).

5.4.1.2 pH and ionic strength dependant adsorption experiments with *B.subtilis*

A bacterial concentration of 0.25 OD was chosen for the pH and ionic strength dependant adsorption experiments (Bs2) as 100% NP removal was not observed at this bacterial density in the concentration dependent experiments (Figure 5.2, purple crosses). Hence, any change in bacterial adsorption due to pH and ionic strength effects would be observed. The concentration of NPs adsorbed onto *B. subtilis* was shown to be highly dependent on both pH and ionic strength. Generally, as pH increased so too did NP adsorption onto the surface of *B. Subtilis*. For example at pH 10, 95% of the S-pos NPs were removed from

solution when suspended 10 mM NaCl, whereas at pH 2 only 25% NP adsorption occurred (Figure 5.3, red squares). In addition to this, increasing the ionic strength of the solution resulted in a decrease in the percentage of NPs adsorbed by *B. subtilis*. At pH 8, 95% of the NPs added were adsorbed by *B. subtilis*, when suspended in 1 mM NaCl (Figure 5.3, blue diamond's). In comparison only 55% NP adsorption occurred when suspended in a solution of 100 mM NaCl at the same pH (Figure 5.3, green triangles). Similarly the influence pH exerts on NP adsorption is controlled by ionic strength, resulting in pH dependent adsorption trends exhibiting a steeper slope at lower ionic strengths (at least between pH 2-9, Figure 5.3).

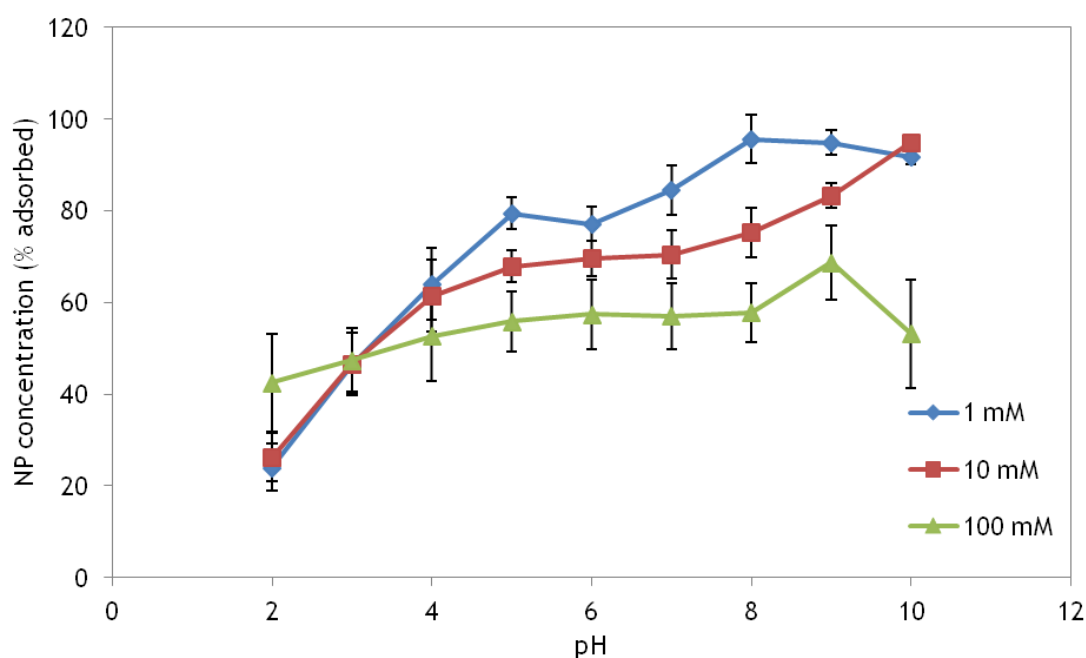


Figure 5.3: NP sorption as a function of pH and ionic strength.

NP sorption onto 0.25 OD *B. subtilis* was tested as a function of pH in 1 mM (blue triangles), 10 mM (red squares) and 100 mM (green triangles) NaCl electrolyte concentration. Each data point represents the average of triplicate experiments with associated standard deviation ($\sigma = 1$, shown as error bars).

5.4.1.3 Desorption experiments with *B.subtilis*

Desorption experiments were performed to test the reversibility of NP adsorption onto the surface of *B. subtilis*. The bacteria-NaCl (10 mM) suspension was adjusted to pH 10 before addition of S-pos NPs. At this pH 91% S-Pos NPs were removed from solution; this is in excellent agreement with the adsorption experiment whereby 95% NPs were adsorbed from solution (Figure 5.4).

Decreasing the pH of the bacterial-NP solution imparted no notable change in the percentage of NPs adsorbed onto the cell wall of *B. subtilis*, that is until pH 5. Here, 10% of the previously adsorbed NPs were resuspended with a pH drop from 6 to 5. The resuspension of a further 10% of the S-pos NPs occurred when decreasing the solution pH to 2 (Figure 5.4). There is a clear difference between the adsorption and desorption trends. While there is 69% difference in NP removal between pH 2 and 10 in the adsorption experiment, there is only 16% difference in NP removal in the desorption experiment (Figure 4).

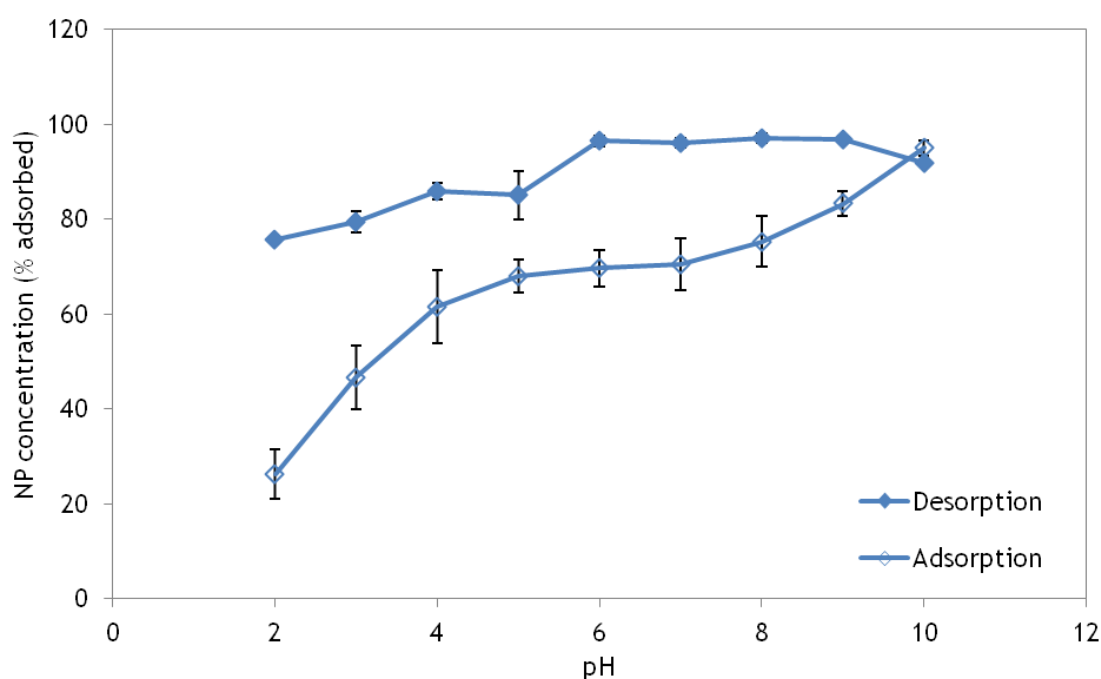


Figure 5.4: NP desorption vs. adsorption experiments. NP desorption experiments (solid diamonds) were performed in 10 mM NaCl with 0.25 OD *B. subtilis*. The adsorption trend line is taken from figure 2. Each data point represents the average of triplicate experiments with associated standard deviation ($\sigma = 1$, shown as error bars).

5.4.2 Wastewater biofilm sorption experiments

5.4.2.1 Concentration dependant adsorption experiments with biofilm flocs

NP adsorption experiments were then tested as a function of time using S-pos NPs with wastewater biofilm flocs. In these experiments NP adsorption was complete within 10 minutes for the 4 g experiment, while at lower floc concentrations (2 g), NP adsorption was slower, reaching completion at approximately 90 minutes (Figure 5.5). Note that neither the 4 nor 2 g

experiment had reached equilibrium at the concentrations texted here. Increasing the bacterial concentration from 2 g to 4 g did not result in an increase in the final percentage of NPs adsorbed as total adsorption of NPs occurred with 98% and 96% adsorbed respectively (Figure 5.5). In contrast little removal was observed in the blank (containing S-pos NPs only), fluctuating between 0-10% for the duration of the experiment (Figure 5.5).

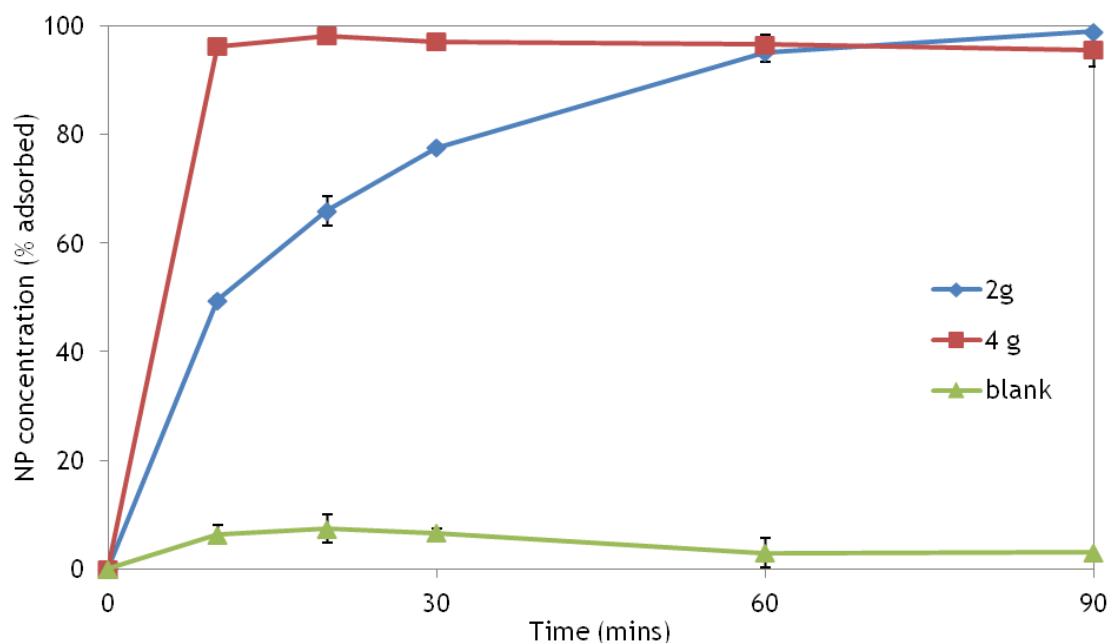


Figure 5.5: Percent Fe (NPs) adsorbed by wastewater biofilm as a function of time in 10 mM NaCl.

Biofilm concentrations of 2 g (blue diamond's) and 4 g (red squares) were chosen to determine the impact of biofilm concentration on the sorption of S-pos NP suspended in 10 mM NaCl. A blank experiment (green triangles) containing S-pos NPs without biofilm was also run. Each data point represents the average of triplicate experiments with associated standard deviation ($\sigma = 1$, shown as error bars).

5.4.2.2 pH and ionic strength dependant adsorption experiments with biofilm flocs

A biofilm concentration of 2 g was chosen for the pH and ionic strength dependant experiments. The concentration of NPs adsorbed onto the biofilm flocs was highly dependent on ionic strength, with greater adsorption occurring at lower ionic strengths (Figure 5.6). In contrast, pH imparted no significant effect on the adsorption of NPs in solutions containing 1 mM and 100 mM NaCl (Figure 5.6). Notably, pH exerted a significant control on the adsorption of NP onto biofilm flocs when suspended in 10 mM NaCl. Generally as pH increased the percentage of NPs adsorbed onto the biofilm increased. However, as with the *B. subtilis* pH and ionic strength experiments, this was not a linear trend (Figure

5.3 and Figure 5.6). Figure 5.6 illustrates the pH dependence of the biofilm flocs suspended in 10 mM NaCl (red squares). At pH 10 95% NPs are adsorbed. Decreasing the pH to 8 results in a sharp decrease in the percentage of NPs adsorbed by 15%. Whilst decreasing the pH further to 5 caused little change, decreasing NP adsorption by a mere 5%. A final decrease by 10% occurred with a pH drop to 4, with no change thereafter.

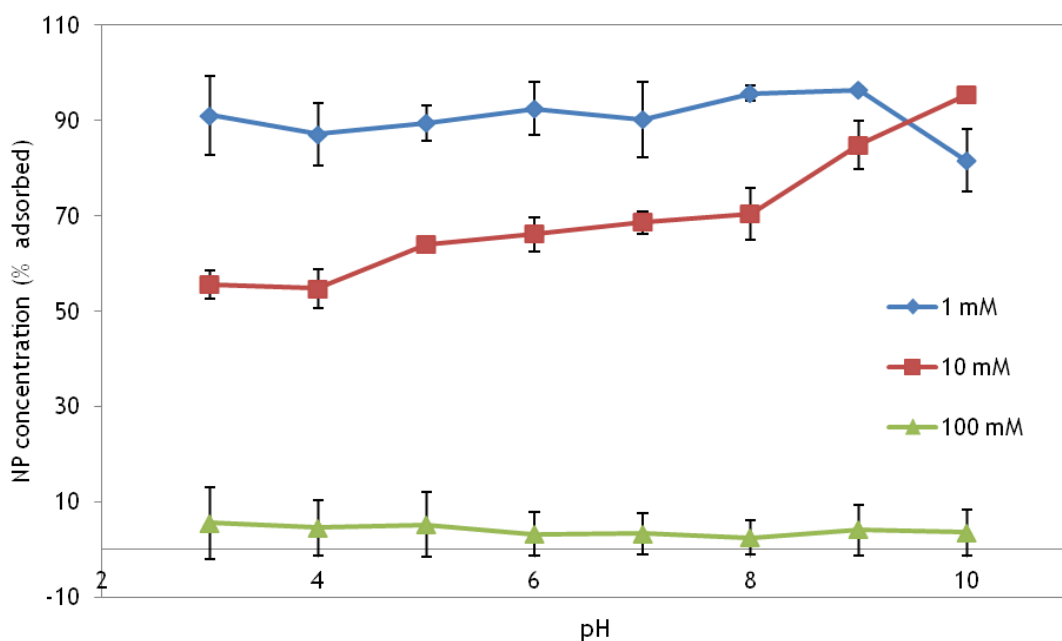


Figure 5.6: NP sorption onto 2 g wastewater biofilm as a function of pH in 1 mM (blue triangles), 10 mM (red squares) and 100 mM (green triangles) NaCl electrolyte concentration. Each data point represents the average of triplicate experiments with associated standard deviation ($\sigma = 1$, shown as error bars).

5.4.3 Transmission Electron Microscopy (TEM)

TEM of *B. subtilis* cells reacted with s-posNPs are shown in Figure 5.7. Samples that are both pre- and post-stained (Figure 5.7a) and samples that are just post-stained (Figure 5.7b) show similarly good contrast of the cytoplasm and cell walls. As expected, the cytoplasm and cell wall lacks contrast in the unstained samples (Figure 5.7c). The cells appear to be surrounded by a layer of nanoparticles up to 200 nm thick. In samples that were pre- and post-stained (Figure 5.7a), the nanoparticles do not stand out so clearly as they appear to be embedded in material that exhibits contrast. However, when either just post-stained or non-stained the nanoparticles stand out more clearly as any material

they are embedded in exhibits no contrast (Figure 5.7b,c,d). It is possible the nanoparticles are embedded in a diffuse extracellular polymeric substance (EPS) layer that is only picked up by the double staining approach. Alternatively, the nanoparticles may have aggregated on the surface to form the thick layer of nanoparticles. However, as these nanoparticles do not aggregate, this seems unlikely. It is also notable that intracellular NPs were not observed, indicating the NPs could not be transported across the cell wall.

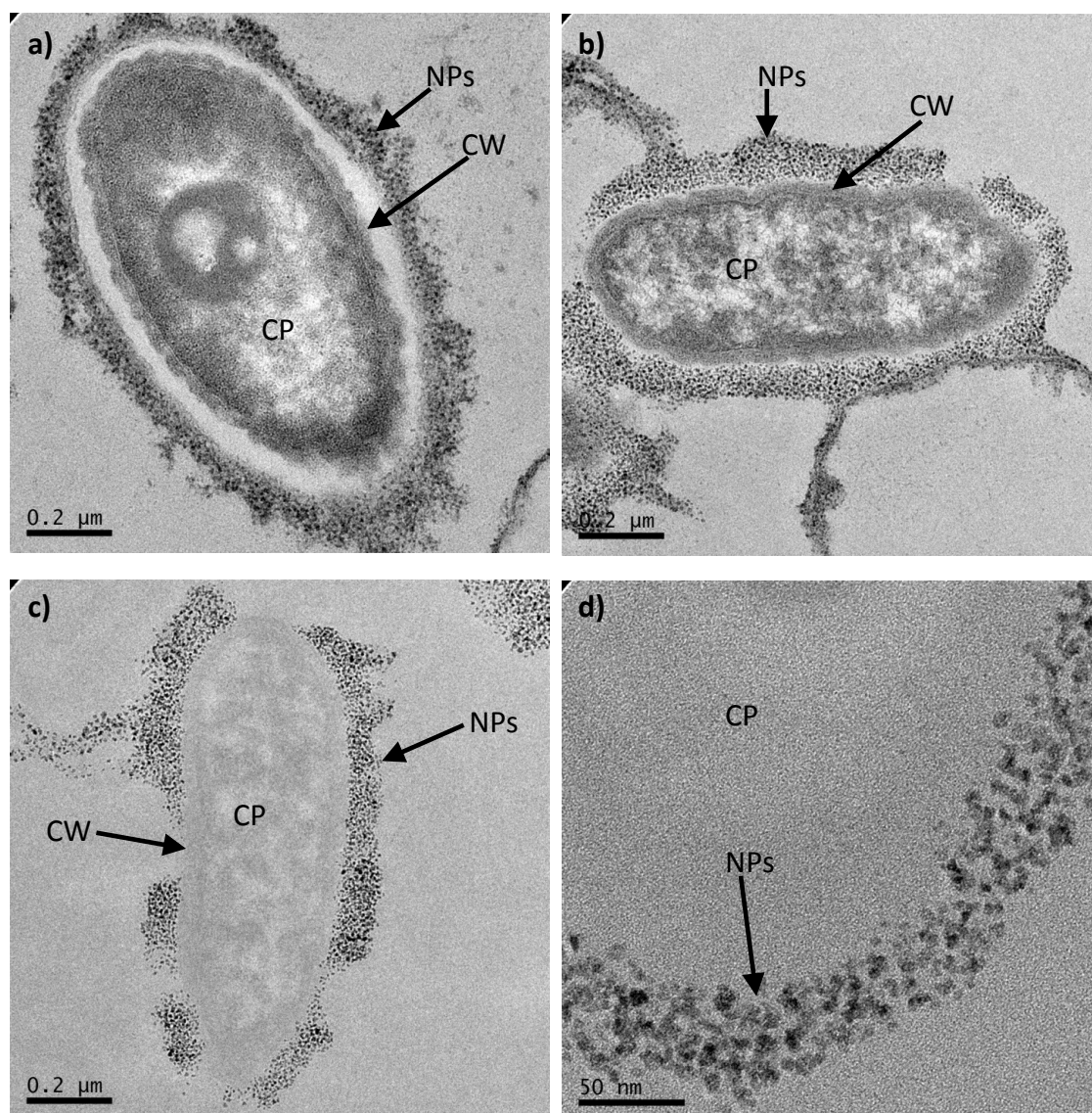


Figure 5.7: TEM micrographs of *B. subtilis* cells reacted with s-posNPs. (a) pre- and post-stained sample, (b) post stained sample, (c) and (d) unstained sample. NPs = nanoparticles, CP = cytoplasm, CW = cell wall.

TEM of biofilm reacted with s-posNPs is shown in Figure 5.8. The biofilm is composed of a dense pack of cells, some intact and likely viable as evidenced by their intact cytoplasm and cell walls, while others had clearly lysed and only

distorted cell walls remained (Figure 5.8a,b). Pre-and-post and just post-stained samples exhibited identical levels of contrast. They also exhibited possible nanoparticles attached to EPS (Figure 5.8, c,d), however, as these could not be found in non-stained samples it is not possible to confirm if these were nanoparticles. Problematically, the condition of the TEM filament at the time of analysis was not sufficient for chemical analysis by EELS, and thus further examination of these potential NPs was not possible. The difficulty in finding nanoparticles in the biofilm compared to the *B.subtilis* cells is likely due to two reasons. Either areas of the biofilm imaged did not come into contact with the NPs (possibly because the NPs could not diffuse to that region, e.g. NPs were bound to the biofilm surface and these images are not of the surface), or because the NPs were highly dispersed to a low density among the voluminous biofilm such that they were hard to find.

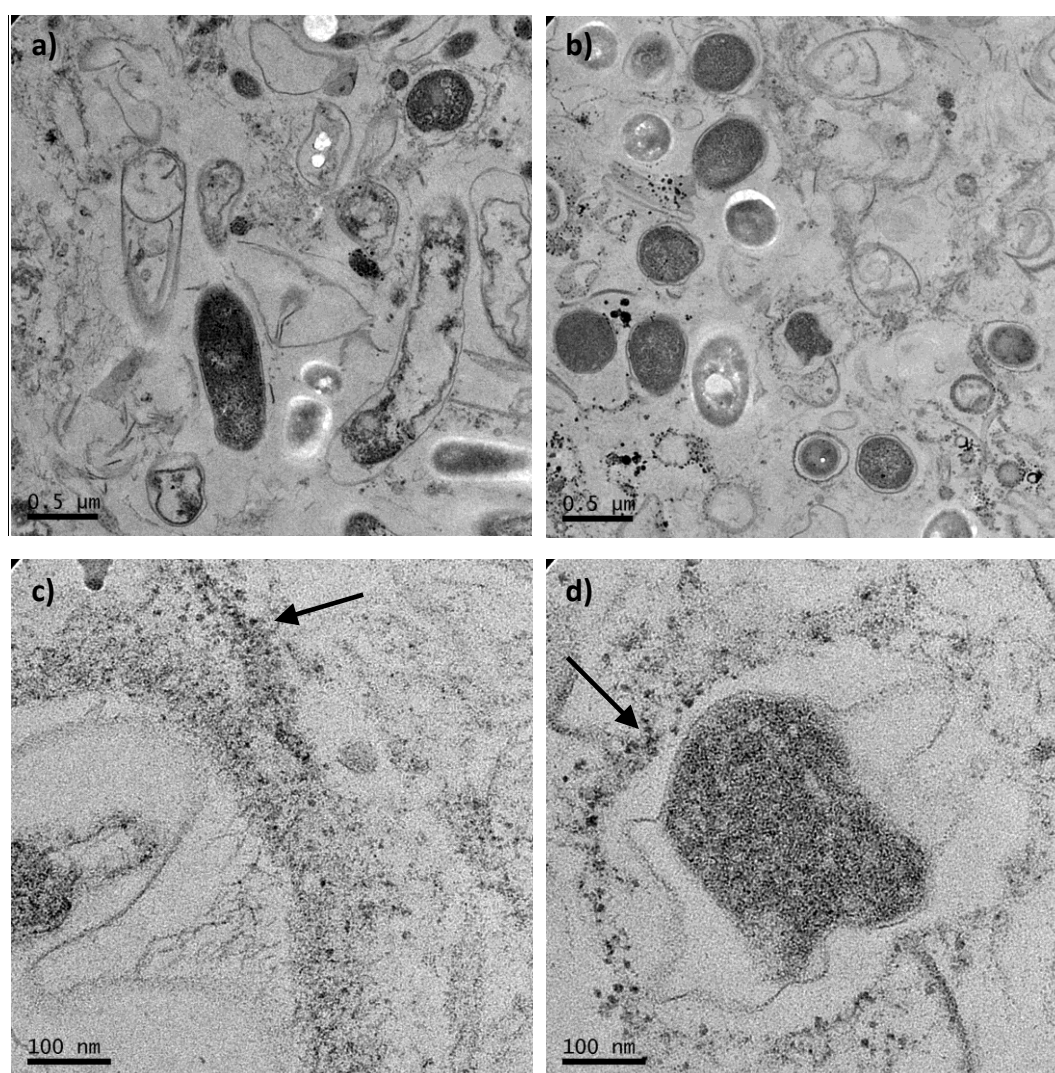
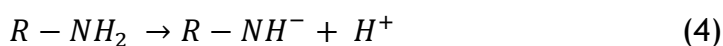
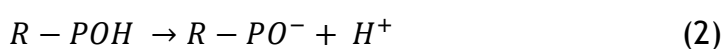
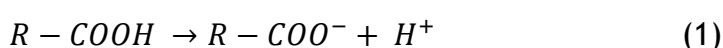


Figure 5.8: TEM images of biofilm reacted with s-posNPs. All images are post-stained. Arrows indicate possible NPs.

5.4.4 Discussion

In this study both the single celled bacteria *B. subtilis* and multi-community wastewater biofilm flocs showed significant adsorption of the s-pos NPs under most conditions. In contrast no adsorption of s-neg NPs occurred. However the degree to which pH and ionic strength affects the biosorbant properties of each agent varied. Here, the *B. subtilis* system was found to be highly dependent on pH, with greater pH sensitivity at lower ionic strengths. In contrast the biofilm flocs were found to be highly ionic strength dependant with any change in pH having less influence on the adsorption properties of the biofilm.

In the case of the *B. subtilis* system the bacterial cell wall is the first component that comes into contact with NPs. The cell wall of *B. subtilis* and other gram positive bacteria are primarily composed of a thick peptidoglycan layer (Doyle et al., 1980, Vijayaraghavan and Yun, 2008). Several functional groups which exist on the outer surface of the bacterial cell wall have long been known to control metal cation adsorption by a variety of microorganisms (Fein et al., 1997, Doyle et al., 1980, Beveridge, 1989, Ngwenya et al., 2003). These include carboxyl, phosphoryl, amine and hydroxyl groups. It is the ionisation (deprotonation) of these functional groups which imparts a negative charge surrounding the cell. The reaction for the deprotonation of carboxyl, phosphoryl and hydroxyl groups are as follows:



where *R* represents the bacterial membrane to which (from top to bottom) the carboxyl, phosphoryl, hydroxyl and amine functional groups are attached (after Fein et al. (1997)).

This process induces an electrostatic attraction between the positively charged NPs and the negatively charged bacterial cell, resulting in the

adsorption of up to 100% of the positively charged NPs, depending on pH, ionic strength and bacterial density. In the case of the s-neg NPs an electrostatic barrier between the bacterium and the NP exists due to electrostatic repulsion, preventing adsorption of the negatively charged NPs. TEM analysis of *B. subtilis* cells reacted with s-posNPs suggested the NPs may be embedded within a thin (up to 200 nm) layer of EPS surrounding the cell wall. Similar to the cell wall, this EPS layer could also exhibit functional groups imparting it with a negative charge.

The adsorption of positively charged NPs onto the surface of *B. subtilis* was found to be highly pH and ionic strength dependant. Generally, NP adsorption increases with increasing pH, and decreases with increasing electrolyte concentration. The deprotonation of surface functional groups with increasing pH results in an increasingly negative cell surface charge at higher pH's, increasing attractive electrostatic interactions between the NP and bacterial cell. Notably this is not a linear trend. For intermediate and low electrolyte concentration (1 and 10 mM NaCl) a steepening of the adsorption profile can be seen between pH 2 to 4 (Figure 5.3). The ionisation of carboxyl functional groups are likely responsible for NP adsorption within the lower pH range of 2 to 4. Carboxylic functional groups have been shown to become active over a pH range of 2 to 6, with a mean pK_a of 4.5 (Cox et al., 1999). Within this range the carboxylic functional groups deprotonate, increasing the negative charge surrounding them. This would appear to result in an increased affinity for the positively charged NPs, as demonstrated by a steep increase in NP adsorption from 25% at pH 2 to 60% at pH 4 for intermediate and low electrolyte concentration (Figure 5.3). A similar trend is visible in the 100 mM NaCl experiment however here NP adsorption increased by only 10% when solution pH increased from pH 2 to 4 (Figure 5.3). The deprotonation of the carboxylic functional groups had less of an electrostatic effect here as the increased electrolyte concentration resulted in a dulling of the negative charge on the bacteria, hence weakening the electrostatic attraction between the NP and bacterial surface. Increasing solution pH from 4 to 8 caused a smaller rate of change in NP adsorption. Within this range phosphoryl sites become active. Again higher ionic strengths caused the rate of change in NP adsorption to be reduced compared to at lower ionic strengths. It is important to note that the NPs are surrounded by amine functional groups, imparting a positive charge

around the particle. Since amine functional groups begin to deprotonate at pH 9 (Cox et al., 1999), the positive charge surrounding the NP will decrease from around pH 9 upwards. However, there is no clear evidence from the adsorption profiles that this has any impact on NP adsorption (for example, while a decrease in NP adsorption is seen between pH 8-10 at 1 mM NaCl, an increase is seen at 10mM NaCl)

Increasing solution ionic strength had a marked impact on the adsorption of NPs onto the cell surface of *B. subtilis*. Overall increasing electrolyte concentration resulted in a decrease in NP adsorption. Here, increasing solution electrolyte concentration masks the negative charge of the bacterium and the positive charge on the NP, resulting in a dulled electrostatic attraction between the NP and the bacterial cell wall. Figure 5.3 demonstrates that 95% NP adsorption occurred at pH 10 when suspended in 10 mM NaCl, however when the electrolyte concentration increased to 100 mM NaCl, NP adsorption onto the cell decreased to 53% due to the masking effect of the Na⁺ and Cl⁻ ions acting on the NP and bacterial surface.

It is important to note the 'meeting' point of the curves in Figure 5.3. Here all three curves cross at pH 3, this is close to the isoelectric point for *B. subtilis* bacterial cells which occurs at approximately pH 2.4 (Yee et al., 2004). This is consistent with work carried out by Yee et al. (2004) where metal biosorption experiments were performed using *B. subtilis*. Here, Ca²⁺ Sr²⁺ and Ba²⁺ ions suspended in three different electrolyte concentrations all converge at pH 3.

However, unlike in most cation adsorption experiments, NP adsorption here was largely irreversible. Figure 5.4 displays the desorption of only 15% NPs when solution was dropped from pH 10 to 2. These findings are notably different from desorption experiments using *B. subtilis* and metal cations. When metal cations are bound to bacterial cell wall, desorption curves follow very similar profiles to the adsorption curves (i.e. almost no hysteresis) (Fowle and Fein, 2000). It is clear then that while metal cation adsorption is fully reversible (Fowle and Fein, 2000), NP adsorption displays relatively little reversibility. Permanent attachment of NPs confirms that electrostatic interactions are not the only force controlling NP adsorption onto the bacterial surfaces. Another force must be responsible for the permanent attachment of NPs as if

electrostatic interactions were the sole force acting on the NP and bacterium then NP binding would be expected to be fully reversible. NP uptake by *B. subtilis* is suggested to occur as a two step process. The first step involves electrostatic forces attracting the NP to the cell surface to allow for initial electrostatic attachment to take place. The second step results in the largely irreversible attachment of NPs onto the cell surface. A combination of electrical and non-electrical interactions occurring between the outer cell surface and the outer surface of the NP may be responsible for such attachment. These electrosteric interactions may be repulsive or attractive (Rijnaarts et al., 1999). Repulsive forces dominate if the cell surface is hydrophilic and has no affinity for the substratum whilst irreversible bridging may occur if attractive forces exist, this is likely to result if both particles are hydrophobic and some attractive force exist (Rijnaarts et al., 1999). The hydrophobic properties of microbial cells have been well reported. It is widely agreed that microbial cell surface hydrophobicity is the dominant control of microbial adhesion to surfaces, educing biofilm formation (Ahimou et al., 2000). Microbial adhesion has been found to be ionic strength dependant, with steric interactions becoming stronger as ionic strength increases, enhancing bacterial attachment to surfaces (Rijnaarts et al., 1999). Hydrophobic interactions may therefore account for NP adsorption under high ionic strength conditions (Figure 5.3Figure 5.6). In addition , Ahimou et al (2000) determined that the production of lipopeptide by *B. subtilis* increases the hydrophobicity of the cell, increasing the attractive van der Waals interaction (van Loosdrecht et al., 1990). It is important to note that the NPs are also surrounded by hydrophobic amine terminations (cyclohexylamine), these may form bridges with the hydrophobic bacterial surface polymers, permanently attaching NPs to the cell surface of the bacteria. Indeed, based on TEM, this may not just occur upon the cell surface but possibly within a matrix of EPS which surrounds the cell. Despite this some desorption did occur. Figure 5.4 highlights the resuspension of only 15% of previously adsorbed NPs due to decreasing solution pH from 10 to 2, indicating that not all NPs are permanently attached to the bacterial surface. Clearly some NPs are not influenced by the irreversible electrosteric interactions; instead they are electrostatically controlled, allowing for reversible adsorption onto the bacterial cell.

Wastewater biofilm flocs were shown to be highly successful adsorbents, showing 100 % NP adsorption for the 2 and 4 g/10 ml adsorption experiments (Figure 5.5). As with the *B. subtilis* system NP adsorption first occurs through electrostatic attraction. Then, based on the *B. subtilis* experiments, permanent attachment occurs on the cell wall of individual bacterium and EPS in the biofilm. In the case of the wastewater biofilm NP binding will occur on the bacteria on the outer perimeter of the floc. In addition to this diffusion and advection of NPs into the bacterial pellet may also occur, embedding NPs within the bacterial floc. Evidence for diffusion of NPs into the flocs was revealed by determining the total quantity NPs immobilized per unit of biomass. Results show that typically 0.057 mg NPs/mg dry mass of biofilm were adsorbed, while 0.079 mg NPs/mg dry mass *B. subtilis* were adsorbed. If only the surface of the flocs was available for NP binding, one would expect orders of magnitude less NP adsorption compared to *B. subtilis*, as the flocs are orders of magnitude larger than *B. subtilis* and therefore will have orders of magnitude less surface area. However, the fact that total NP immobilization is broadly similar in both *B. subtilis* and floc experiments, suggests NPs are diffusing into the flocs to access other surfaces (i.e. cells and EPS inside the biofilm). Diffusion is the dominant process for solute transport within biofilm flocs (Stewart, 2003, Stoodley and Lewandowski, 1994, de Beer et al., 1997). The production of EPS has been shown to be an important factor in the retention of colloids (Leon Morales et al., 2007). Leon Morales et al. (2007) determined that the production of extracellular proteins resulted in the increased retention of colloids through sand columns inoculated with *Pseudomonas aeruginosa*. The porosity and diffusive properties exhibited by biofilm flocs are predominantly controlled by the production of EPS in a biofilm (Golmohamadi et al., 2013). NP transport studies determined that NP size is the dominant control for NP uptake by biofilms via diffusion (Golmohamadi et al., 2013, Peulen and Wilkinson, 2011). Peulen et al. (2011) found that NPs smaller than 50 nm were readily adsorbed by biofilm coated sand grains via diffusion, however those larger than 50 nm were poorly incorporated. This finding is in agreement with Golmohamadi et al. (2013) whereby 66 nm titanium dioxide NPs did not penetrate biofilms produced from a strain of *Pseudomonas fluorescens*, i.e. NPs were larger than the pore size exhibited by EPS, thus completely excluding the NPs from the biofilm. The porous structure of the biofilm flocs may be responsible for slow uptake of NPs by the 2g/10 ml

biomass system as the NPs used here fall within this size range (<66 nm, Figure 5.6) i.e., they are small enough to diffuse into the biofilm but their transport is slow. Slow uptake kinetics are not observed in the 4g system as there is more biomass and therefore NP immobilization is faster. In addition, cellular uptake of NPs by the biofilm is possible via facilitated transport. This process occurs as channel like transmembrane proteins transport NPs across the membrane (Kiser et al., 2010). Crucially, the largest transmembrane porins exhibit an opening diameter of 6 nm (Kiser et al., 2010) and so the NPs used here are unlikely to exhibit cellular uptake by the biofilm. However, NPs <10 nm have been reported to penetrate bacterial cells (Choi and Hu, 2008). In contrast, NP adsorption exhibited here likely occurs via a process of self-diffusion where by the NPs are influenced by Brownian motion within the biofilm matrix, rather than the cellular uptake of NPs. Hence, diffusion aided by electrostatic attraction is thought to be the dominant transport mechanism for NP immobilisation by wastewater biofilms.

The adsorption of NPs onto the biofilm was found to be pH and ionic strength dependant for intermediate electrolyte concentration; however pH did not significantly influence NP adsorption for the low and high electrolyte concentration experiments (Figure 5.6). As with the single celled *B. subtilis* adsorption experiments NP adsorption increased with increasing pH (for intermediate electrolyte concentration) and decreased with increased ionic strength. The pH effect can be clearly seen in the intermediate electrolyte experiment (10 mM NaCl, Figure 5.6,). Here as pH increased NP adsorption increased due to the deprotonation of functional groups on the cell wall of the bacterium and EPS, resulting in an increase from 55% at pH 2 to 95% NP adsorption at pH 10. However any change in pH has little effect on the low and high ionic strength adsorption experiments. This may be expected in the high ionic strength experiments as the increased electrolyte concentrations masks the surface charge upon the NPs and biofilm flocs. However for NPs and biofilm suspended in 1 mM NaCl any change in pH should be clearly observed, however this was not the case with all sample points falling within error of each other (Figure 5.6, blue triangles). This may be explained by the fact that the 1mM system exhibited close to 100% adsorption at pH 2, and therefore there was insufficient 'head-room' in the system to demonstrate greater adsorption at higher pH's.

5.4.5 Conclusion

In this study the removal of NPs by *B. subtilis* and wastewater biofilm flocs was examined. Both biosorbent agents were highly efficient at removing positively charged NPs, whilst negatively charged NPs were poorly adsorbed by *B. subtilis*, being electrostatically repelled from the bacterial surface. For both biosorbent materials the removal of positively charged NPs is facilitated by the electrostatic attraction of positively charged NPs to the negative bacterial cell/floc. In the case of single celled bacteria permanent attachment occurred due to attractive van der Waals interactions, combined with the strong bridging between the NP's hydrophobic amine terminations (cyclohexylamine) and hydrophobic bacterial surface polymers. A key difference in the adsorption mechanism of NPs by *B. subtilis* and wastewater biofilm flocs is diffusion into the porous structure of the biofilm occurs. The results indicate that NP biosorption via *B. subtilis* was highly pH and ionic strength dependant. Whilst wastewater biofilm flocs were ionic strength dependant, whilst varying solution pH offered little change in the sorption properties of the flocs in 1 and 100 mM NaCl. The results presented here indicate that both single celled *B. subtilis* and wastewater biofilm flocs are successful biosorbents for positively charged NPs whilst negatively charged NPs are repelled from the cell of *B. subtilis* and would require alternative methods of immobilisation. Overall, these findings highlight that planktonic bacteria and biofilms are highly efficient biosorbants for NP's, this holds implications for NP transport in environmental systems and through wastewater treatment plants.

6 Conclusion

6.1 Summary

The aim of this PhD was to develop mechanisms to reduce and ultimately immobilise nanoparticles within water and waste water in order to prevent the transport of nanoparticles to sites where they have the potential to cause harm. Over recent years intense research has focused on the toxicity of manufactured nanoparticles and their effects on human health and the natural environment. A growing body of evidence indicates that nanoparticles have the potential to exhibit toxicity to aquatic organisms and have the potential for bioaccumulation in the food chain (Lasagna-Reeves et al., 2010, Zhu et al., 2010, Lee et al., 2008). As the nanotechnology industry continues to expand NPs will inevitably be release into the natural environment. Hence, developing methods to deal with nano-pollution is essential to prevent future environmental pollution incidents and to ensure the safe development of the nanotechnology industry. This was achieved by inducing mineral precipitation in the presence of NPs. The electrostatic interactions occurring between the NP and the mineral surface determined whether the NP became occluded within the mineral precipitate or whether they remained in solution. In addition to mineral precipitating systems, NP immobilisation by bacteria (*B. subtilis* and wastewater treatment biofilm) was also investigated.

This chapter presents a summary of the main finding from each research chapter, highlighting potential future work in this area of research.

6.2 Immobilisation of nanoparticles by mineral precipitating systems

An array of techniques exists for the remediation of numerous groundwater contaminants yet none have been specifically designed to deal with NPs. Here we address this fundamental technology gap by developing mechanisms to immobilise and remove NPs from solution. Microbially mediated calcite precipitation was first tested as this process has been extensively studied over recent years due to its potential in a diverse array of applications. These range

from soil stabilisation (Whiffin et al., 2007) to the solid phase capture of heavy metals and radionuclides (Warren et al., 2001).

This method showed great success in removing negatively charged nanoparticles in batch experiments whilst positively charged nanoparticles remained in solution. Electrostatic interactions greatly controlled the degree of nanoparticle capture. It was hypothesised that negatively charged nanoparticles act as nucleation sites for the precipitating calcite. However the kinetic analysis of calcite precipitation rates determined that the nanoparticle type (surface charge) had no impact on nucleation. Instead nanoparticles attach to growing calcite surfaces in solution, eventually becoming overtaken by the growing solidification front and thus occluded. Negatively charged nanoparticles exert a strong electrostatic attraction to the positively charged calcite surface, facilitating particle entrapment. Whilst in the case of positively charged nanoparticles an electrostatic repulsion exists. DLVO modelling confirms these observations, with attractive energy well acting between the calcite and negative nanoparticles, whilst a repulsive energy barrier exists between the calcite and the positive nanoparticles.

As electrostatic interactions acting between the mineral and nanoparticle determine whether or not the nanoparticle becomes occluded within the mineral, the mineral precipitating system could therefore be specifically tailored to suit the nanoparticle surface character. Thus, in order to capture positively charged nanoparticles, a mineral possessing a negative surface charge would be required. Struvite was chosen not only because it exhibits a negative surface charge but it also requires ammonia to form as it is a magnesium ammonium phosphate mineral. Hence the precipitation of struvite has the potential to remove the undesirable concentrations of ammonia produced as a by-product of ureolysis, whilst also removing positively charged nanoparticles from solution.

Struvite precipitation was first tested in the absence of nanoparticles in order to determine the optimal condition for struvite precipitation. Struvite precipitation was initially tested during ureolysis. That is magnesium and phosphorus are added at the beginning of the experiment so that when ammonium is produced by ureolysis struvite would immediately form. However this was not the case, instead some form of magnesium phosphate mineral was

precipitated despite the production of ammonium. Following this, struvite precipitation was tested again with total urea hydrolysis complete before the addition of magnesium and phosphorus sources in four stages of 25 mM each. This method showed great success, removing 100% of the ammonium produced by ureolysis. This approach was therefore used for the nanoparticle immobilisation experiments. As the mineral precipitates nanoparticles were concurrently removed from solution, up until a point. Nanoparticle removal was found to be highly pH and ionic strength dependant. As the solution pH decreased and ionic strength increased nanoparticle concentration increased. These findings suggest that nanoparticles are electrostatically attached to the mineral surface as opposed to occlusion within the growing mineral (as reported in the calcite precipitating system). Hence, any change in solution pH and ionic strength will greatly affect the surface charge of the nanoparticle and mineral surface. This has the potential to weaken the electrostatic attraction between the nanoparticle and mineral surface, allowing for the resuspension of previously immobilised nanoparticles from solution. The findings here suggest that struvite precipitation removes 100% of the ammonia produced by ureolysis. In addition struvite precipitation successfully removed positively charged nanoparticles from solution. Here the nanoparticles are reversibly attached to the mineral surface and so solution pH and ionic strength must be carefully controlled in order to ensure the removal of positively charged nanoparticles. The fact that nanoparticles are electrostatically attached to the mineral surface could be advantageous. This approach has the potential to be used to recycle nanoparticles by separating them from solution, altering the solution chemistry to resuspend the nanoparticles for secondary use.

The results presented here indicate that the mineral precipitation system may be specifically tailored to treat the NP surface character. Inducing mineral precipitation has the potential to immobilise nanoparticles from contaminated groundwater systems, impacting their transport and fate in environmental systems.

6.3 Immobilisation of nanoparticles through porous media by calcium carbonate precipitation

Following the successful immobilisation of negatively charged nanoparticles by calcium carbonate precipitation in batch experiments this method was tested again through porous media. This was done to in order to increase the complexity of the system, replicating a more real life scenario such as a sand aquifer. Immobilisation was tested as a function of porous media type (glass beads and sand) and grain size (fine, medium and large).

Negatively charged nanoparticles displayed high mobility through all porous media types tested when suspended in deionised water. Nanoparticle mobility was reduced under all experimental conditions tested, however, the lowest rates of nanoparticle mobility were consistently found in columns where calcium carbonate precipitation was promoted. As ureolysis commenced, calcium carbonate precipitation occurred around the nanoparticles, on grain boundaries and within the pore spaces. As in chapter 3, nanoparticles become occluded within the mineral precipitate. In addition, gravitational settling of the nano-calcite composite allows nanoparticles to become cemented to the grain boundaries within the column. The findings from this chapter suggest that microbially mediated calcite precipitation may be used as a tool to significantly reduce nanoparticle mobility in environmental systems.

6.4 Bacterial biosorption of nanoparticles

Bacteria and biofilms are commonly used to adsorb and degrade an array of pollutants, being commonly used as a treatment step in wastewater treatment plants. Here, we tested the ability of *B subtilis*, a common groundwater bacterium, and wastewater biofilm to remove nanoparticles from solution.

The experiments presented here suggest that *B. subtilis* and wastewater biofilm are highly effective at removing positively charged nanoparticles whilst negatively charged nanoparticles remained in solution. The positively charged nanoparticles are electrostatically attracted to the negative charge of the bacterial cell/floc. A key difference in the adsorption mechanism of nanoparticles by *B. subtilis* and wastewater biofilm flocs is that nanoparticles have the ability to diffuse into the porous structure of the biofilm. Both

biosorbent materials were found to be ionic strength dependant, with fewer nanoparticles being removed at higher ionic strength. *B. subtilis* was found to be highly pH dependant, with greater sorption at higher pH, due to the ionisation of surface functional groups increasing the negative charge on the bacterial surface. In contrast any change in pH offered little difference in the sorption properties of the wastewater granules in solutions of 1 and 100mM NaCl.

The results presented here highlight that planktonic bacteria and wastewater treatment biofilm are highly effective sorbents of positively charged nanoparticles. These findings suggest that current municipal wastewater treatment works have the potential to remove positively charged nanoparticles during the biological treatment stage of the process. Wastewater treatment biofilm and activated sludge are removed from the treatment process as settlement sludge. Currently settlement sludge is processed and in some cases is sold as fertiliser to farmers. In such instances it is crucial to monitor this sludge for toxic elements before handing it over to a third party. In the case of negatively charged nanoparticles alternative methods would be required. The removal of negatively charge nanoparticles may be facilitated by the precipitation of calcium carbonate where by the calcite-nano composites are settle and removed. They may then be treated separately or disposed of responsibly.

6.5 Future work

The research presented here demonstrates that nanoparticle immobilisation mechanisms may be specifically tailored to suit the nanoparticle surface properties. In addition current wastewater treatment technologies may be successful sorbents of positively charged nanoparticles whilst negatively charged nanoparticles have the potential to discharge from wastewater treatment works into environmental systems. To ensure the safe development of the nanotechnology industry the immobilisation methods developed throughout this thesis must be explored further. Future work must therefore focus on 1) establishing the current and predicted future environmental concentrations of NPs in the UK and globally; 2) the mineral precipitating systems discussed in this thesis must be scaled up to field scale application; 3) the mineral precipitating systems must be tested with a variety of NP types and concentrations.

Current NP concentrations may be investigated through 24 hour sampling at significant wastewater treatment works to determine the current NP concentration in waste streams. A major flaw of many NP toxicity and transport studies is that researchers do not perform their experiments with environmentally relevant concentrations NPs. This is due to a lack of information regarding the environmental concentration of NPs. However, some estimates of future NP concentrations have been published. These are based on models which look at information such as production volume of NPs, particle release from products and environmental conditions (Mueller and Nowack, 2008). Such studies have rarely been conducted due to the complexity nature of the nanotechnology industry. More needs to be done in this field for researchers and regulatory bodies to fully understand the risk associated with the expansion of the nanotechnology industry.

The bench scale experiments presented here showed great success. However these need to be scaled up in order to increase the complexity of the systems, with the intention of deploying field scale tests. In the case of microbially mediated calcium carbonate precipitation it would be of interest to design a larger scale experiment which exhibits mixing of the reacting fluids, instead of simply bottom to top flow which occurred in the column experiments. A sand box for example could be used. Through this the optimum injection strategy of the reaction fluids could also be tested to ensure the maximum removal of negatively charged nanoparticles. Once an optimum strategy is developed field scale trials may be employed. Such trials may be performed in areas which already have bore holes emplaced such as a disused quarry. Performing field trials in locations such as this would reduce operational costs and to limit environmental damages.

In order to develop the immobilisation of positively charged nanoparticles by struvite precipitation, column experiments must be performed. Here a porous media exhibiting a positive surface charge (such as calcite or dolomite) would be required to ensure that the positively charged nanoparticles are sufficiently mobile. If the column experiments prove to be successful a similar escalation procedure could be followed for the struvite as precipitation experiments as was done for the calcite experiments.

The nanoparticle concentration remained constant at 10 mg/l for all experiments performed in this thesis. It would be of interest to determine whether varying the nanoparticle concentration would impact the removal efficiency of nanoparticles for the methods tested. It would also be of importance to test the technologies presented here with a variety of nanoparticle types, shapes and sizes. For example does nanoparticle shape influence nanoparticle immobilisation by microbially mediated calcium carbonate precipitation? The incorporation of carbon nanotubes for example could be compared to the results presented in chapter 2. In addition silver nanoparticles are specifically tailored for their antimicrobial properties (Rai et al., 2009). Thus it would be of interest to determine if their presence would exhibit toxicity to the bacterial strains utilised in this thesis.

Appendix A

Table A 1: Saturation indices for minerals which could potentially be formed from 10 mM NH_4 , MgCl_2 and K_2HPO_4 at pH 8 as exhibited in the S1 experiment. (Visual MINTEQ, version 3.0).

Mineral	Saturation Index
Struvite	1.587
$\text{Mg}_3(\text{PO}_4)_2$	1.569
$\text{MgHPO}_4 \cdot 4\text{H}_2\text{O}$	0.606
Brucite	-3.672
KCl	-4.484
$\text{Mg}^{2+}(\text{OH})_2$	-5.366
$\text{Mg}_2(\text{OH})_3\text{Cl} \cdot 4\text{H}_2\text{O}$	-8.935
Periclase	-8.157

Appendix B

The Hamaker constant for 2 phases interacting across a medium (3) was calculated according to the equation by Overney (2009):

$$A \approx \frac{3}{4} kT \left(\frac{\varepsilon_1 - \varepsilon_3}{\varepsilon_1 + \varepsilon_3} \right) \left(\frac{\varepsilon_2 - \varepsilon_3}{\varepsilon_2 + \varepsilon_3} \right) + \frac{3h\nu_e}{8\sqrt{2}} \frac{(n_1^2 - n_3^2)(n_2^2 - n_3^2)}{\sqrt{(n_1^2 + n_3^2)}\sqrt{(n_2^2 + n_3^2)}\left\{\sqrt{(n_1^2 + n_3^2)} + \sqrt{(n_2^2 + n_3^2)}\right\}}$$

where ε is the dielectric constant, n the refractive indices and ν_e the absorption frequency.

List of references

- AHIMOU, F., JACQUES, P. & DELEU, M. 2000. Surfactin and iturin A effects on *Bacillus subtilis* surface hydrophobicity. *Enzyme and Microbial Technology*, 27, 749-754.
- ALI, M. I. 2007. Struvite Crystallization in Fed-Batch Pilot Scale and Description of Solution Chemistry of Struvite. *Chemical Engineering Research and Design*, 85, 344-356.
- ALLOTROPES, C. 2013. *SINGLE-WALL CARBON NANOTUBES* [Online]. Available: <http://www.carbonallotropes.com/carbon-nanotubes/39-single-wall-carbon-nanotubes.html> [Accessed 07/09/14].
- ASTHANA, R. & TEWARI, S. N. 1993. The Engulfment Of Foreign Particles By a Freezing Interface. *Journal of Materials Science*, 28, 5414-5425.
- BAKER, B. J. & BANFIELD, J. F. 2003. Microbial communities in acid mine drainage. *FEMS Microbiology Ecology*, 44, 139-152.
- BALL, J. & NORDSTROM, D. 1992. Geochemical model to calculate speciation of major, trace and redox elements in natural waters. *US Geological Survey, International Groundwater Modeling Centre*.
- BANFIELD, J. F. & NEALSON, K. H. 1997. *Geomicrobiology: Interactions between microbes and minerals*, Mineralogical Society of Amer.
- BAR-ILAN, O., ALBRECHT, R. M., FAKO, V. E. & FURGESON, D. Y. 2009. Toxicity assessments of multisized gold and silver nanoparticles in zebrafish embryos. *Small*, 5, 1897-1910.
- BAZYLINSKI, D. A. & FRANKEL, R. B. 2003. Biologically controlled mineralization in prokaryotes. *Reviews in Mineralogy and Geochemistry*, 54, 217-247.
- BEHRENS, S. H. & GRIER, D. G. 2001. The charge of glass and silica surfaces. *The Journal of Chemical Physics*, 115, 6716-6721.
- BEN-MOSHE, T., DROR, I. & BERKOWITZ, B. 2010. Transport of metal oxide nanoparticles in saturated porous media. *Chemosphere*, 81, 387-393.
- BEVERIDGE, T. J. 1989. Role of cellular design in bacterial metal accumulation and mineralization. *Annual Reviews in Microbiology*, 43, 147-171.
- BOARD, T. S. 2009. Nanoscale Technologies Strategy 2009-12. In: BOARD, T. S. (ed.). Innovate UK.
- BOUROPOULOS, N. C. & KOUTSOUKOS, P. G. 2000. Spontaneous precipitation of struvite from aqueous solutions. *Journal of Crystal Growth*, 213, 381-388.
- BRADFORD, S. A. & TORKZABAN, S. 2008. Colloid Transport and Retention in Unsaturated Porous Media: A Review of Interface-, Collector-, and Pore-Scale Processes and Models All rights reserved. No part of this periodical may be reproduced or transmitted in any form or by any means, electronic or mechanical, including photocopying, recording, or any information storage and retrieval system, without permission in writing from the publisher. *Vadose Zone J.*, 7, 667-681.
- BRADFORD, S. A., YATES, S. R., BETTAHAR, M. & SIMUNEK, J. 2002. Physical factors affecting the transport and fate of colloids in saturated porous media. *Water Resources Research*, 38, 1327.
- BRAR, S. K., VERMA, M., TYAGI, R. D. & SURAMPALLI, R. Y. 2010. Engineered nanoparticles in wastewater and wastewater sludge - Evidence and impacts. *Waste Management*, 30, 504-520.
- BRITANNICA, E. 2014. Bacteria.
- BYSTRZEJEWSKA-PIOTROWSKA, G., GOLIMOWSKI, J. & URBAN, P. L. 2009. Nanoparticles: Their potential toxicity, waste and environmental management. *Waste Management*, 29, 2587-2595.

- CARRE, A. & LACARRIERE, V. 2006. Study of surface charge properties of minerals and surface-modified substrates by wettability measurements. *Contact Angle, Wettability and Adhesion*, 4, 1.
- CHATTERJEE, R. 2008. The Challenge of Regulating Nanomaterials. *Environmental Science & Technology*, 42, 339-343.
- CHEN, H., ROCO, M. C., SON, J., JIANG, S., LARSON, C. A. & GAO, Q. 2013. Global nanotechnology development from 1991 to 2012: patents, scientific publications, and effect of NSF funding. *Journal of Nanoparticle Research*, 15, 1-21.
- CHOI, O. & HU, Z. 2008. Size dependent and reactive oxygen species related nanosilver toxicity to nitrifying bacteria. *Environmental Science & Technology*, 42, 4583-4588.
- CLAPHAM, L., MCLEAN, R., NICKEL, J., DOWNEY, J. & COSTERTON, J. 1990. The influence of bacteria on struvite crystal habit and its importance in urinary stone formation. *Journal of Crystal Growth*, 104, 475-484.
- COLMAN, B. P., ARNAOUT, C. L., ANCIAUX, S., GUNSCH, C. K., HOHELLA JR, M. F., KIM, B., LOWRY, G. V., MCGILL, B. M., REINSCH, B. C. & RICHARDSON, C. J. 2013. Low concentrations of silver nanoparticles in biosolids cause adverse ecosystem responses under realistic field scenario. *PloS one*, 8, e57189.
- COX, J. S., SMITH, D. S., WARREN, L. A. & FERRIS, F. G. 1999. Characterizing Heterogeneous Bacterial Surface Functional Groups Using Discrete Affinity Spectra for Proton Binding. *Environmental Science & Technology*, 33, 4514-4521.
- COYLE, S., WU, Y., LAU, K.-T., DE ROSSI, D., WALLACE, G. & DIAMOND, D. 2007. Smart nanotextiles: a review of materials and applications. *MRS bulletin*, 32, 434-442.
- CUTHBERT, M. O., RILEY, M. S., HANDLEY-SIDHU, S., RENSHAW, J. C., TOBLER, D. J., PHOENIX, V. R. & MACKAY, R. 2012. Controls on the rate of ureolysis and the morphology of carbonate precipitated by *S. Pasteurii* biofilms and limits due to bacterial encapsulation. *Ecological Engineering*, 41, 32-40.
- DE BEER, D., STOODLEY, P. & LEWANDOWSKI, Z. 1997. Measurement of local diffusion coefficients in biofilms by microinjection and confocal microscopy. *Biotechnology and bioengineering*, 53, 151-158.
- DE MUYNCK, W., DE BELIE, N. & VERSTRAETE, W. 2010. Microbial carbonate precipitation in construction materials: A review. *Ecological Engineering*, 36, 118-136.
- DEFRA 2011. Characterising the Potential Risks posed by Engineered Nanoparticles. In: ENVIRONMENT, F. A. R. A. (ed.) A Second UK Government Research Report ed.
- DELLA PINA, C., FALLETTA, E., PRATI, L. & ROSSI, M. 2008. Selective oxidation using gold. *Chemical Society reviews*, 37, 2077-2095.
- DESMIDT, E., GHYSELBRECHT, K., MONBALLIU, A., RABAEY, K., VERSTRAETE, W. & MEESCHAERT, B. D. 2013. Factors influencing urease driven struvite precipitation. *Separation and Purification Technology*, 110, 150-157.
- DEVOUARD, B., POSFAI, M., HUA, X., BAZYLINSKI, D. A., FRANKEL, R. B. & BUSECK, P. R. 1998. Magnetite from magnetotactic bacteria: Size distributions and twinning. *American Mineralogist*, 83, 1387-1398.
- DHAWAN, A. & SHARMA, V. 2010. Toxicity assessment of nanomaterials: methods and challenges. *Analytical and Bioanalytical Chemistry*, 398, 589-605.
- DONLAN, R. M. 2002. Biofilms: microbial life on surfaces. *Emerging infectious diseases*, 8, 881-90.

- DOYLE, J., OLDRING, K., CHURCHLEY, J., PRICE, C. & PARSONS, S. 2003. Chemical Control of Struvite Precipitation. *Journal of Environmental Engineering*, 129, 419-426.
- DOYLE, J. D. & PARSONS, S. A. 2002. Struvite formation, control and recovery. *Water Research*, 36, 3925-3940.
- DOYLE, R. J., MATTHEWS, T. H. & STREIPS, U. N. 1980. Chemical basis for selectivity of metal ions by the *Bacillus subtilis* cell wall. *Journal of bacteriology*, 143, 471-480.
- DUNPHY GUZMAN, K. A., FINNEGAN, M. P. & BANFIELD, J. F. 2006. Influence of Surface Potential on Aggregation and Transport of Titania Nanoparticles. *Environmental Science & Technology*, 40, 7688-7693.
- DUPRAZ, S., PARMENTIER, M., MÉNEZ, B. & GUYOT, F. 2009. Experimental and numerical modeling of bacterially induced pH increase and calcite precipitation in saline aquifers. *Chemical Geology*, 265, 44-53.
- EBY, D. M., LUCKARIFT, H. R. & JOHNSON, G. R. 2009. Hybrid antimicrobial enzyme and silver nanoparticle coatings for medical instruments. *ACS applied materials & interfaces*, 1, 1553-1560.
- EEA 2002. Late lessons from early warnings: the precautionary principle 1896-2000. . In: AGENCY, E. E. (ed.).
- EL-DEAB, M. S. & OHSAKA, T. 2003. Electrocatalysis by nanoparticles: oxygen reduction on gold nanoparticles-electrodeposited platinum electrodes. *Journal of Electroanalytical Chemistry*, 553, 107-115.
- EL BADAWY, A. M., ALY HASSAN, A., SCHECKEL, K. G., SUIDAN, M. T. & TOLAYMAT, T. M. 2013. Key Factors Controlling the Transport of Silver Nanoparticles in Porous Media. *Environmental Science & Technology*, 47, 4039-4045.
- ENGINEERING, R. S. A. R. A. O. 2004. *Nanoscience and nanotechnologies:opportunities and uncertainties* [Online]. London. Available: <http://www.nanotec.org.uk/report/chapter5.pdf> [Accessed 09.08.2011 2011].
- ENGINEERING., R. S. A. R. A. O. 2004. *Nanoscience and nanotechnologies:opportunities and uncertainties* [Online]. London. Available: <http://www.nanotec.org.uk/report/chapter5.pdf> [Accessed 09.08.2011 2011].
- ERIKSSON, R., MERTA, J. & ROSENHOLM, J. B. 2007. The calcite/water interface: I. Surface charge in indifferent electrolyte media and the influence of low-molecular-weight polyelectrolyte. *Journal of Colloid and Interface Science*, 313, 184-193.
- ESQUIVEL, E. V. & MURR, L. E. 2004. A TEM analysis of nanoparticulates in a Polar ice core. *Materials Characterization*, 52, 15-25.
- FABREGA, J., TANTRA, R., AMER, A., STOLPE, B., TOMKINS, J., FRY, T., LEAD, J. R., TYLER, C. R. & GALLOWAY, T. S. 2011. Sequestration of zinc from zinc oxide nanoparticles and life cycle effects in the sediment dweller amphipod *Corophium volutator*. *Environmental Science & Technology*, 46, 1128-1135.
- FANG, J., SHAN, X.-Q., WEN, B., LIN, J.-M. & OWENS, G. 2009. Stability of titania nanoparticles in soil suspensions and transport in saturated homogeneous soil columns. *Environmental Pollution*, 157, 1101-1109.
- FEIN, J. B., BOILY, J.-F., YEE, N., GORMAN-LEWIS, D. & TURNER, B. F. 2005. Potentiometric titrations of *Bacillus subtilis* cells to low pH and a comparison of modeling approaches. *Geochimica et Cosmochimica Acta*, 69, 1123-1132.

- FEIN, J. B., DAUGHNEY, C. J., YEE, N. & DAVIS, T. A. 1997. A chemical equilibrium model for metal adsorption onto bacterial surfaces. *Geochimica et Cosmochimica Acta*, 61, 3319-3328.
- FERRIS, F. G., PHOENIX, V., FUJITA, Y. & SMITH, R. W. 2004. Kinetics of calcite precipitation induced by ureolytic bacteria at 10 to 20°C in artificial groundwater. *Geochimica et Cosmochimica Acta*, 68, 1701-1710.
- FOLETTTO, E. L., SANTOS, W. R. B. D., MAZUTTI, M. A., JAHN, S. L. & GÜNDEL, A. 2013. Production of struvite from beverage waste as phosphorus source. *Materials Research*, 16, 242-245.
- FOWLE, D. A. & FEIN, J. B. 2000. Experimental measurements of the reversibility of metal-bacteria adsorption reactions. *Chemical Geology*, 168, 27-36.
- FRANCHI, A. & O'MELIA, C. R. 2003. Effects of Natural Organic Matter and Solution Chemistry on the Deposition and Reentrainment of Colloids in Porous Media. *Environmental Science & Technology*, 37, 1122-1129.
- FREY, N. A., PENG, S., CHENG, K. & SUN, S. 2009. Magnetic nanoparticles: synthesis, functionalization, and applications in bioimaging and magnetic energy storage. *Chemical Society reviews*, 38, 2532-2542.
- FUJITA, Y., REDDEN, G. D., INGRAM, J. C., CORTEZ, M. M., FERRIS, F. G. & SMITH, R. W. 2004. Strontium incorporation into calcite generated by bacterial ureolysis. *Geochimica et Cosmochimica Acta*, 68, 3261-3270.
- FUJITA, Y., TAYLOR, J. L., GRESHAM, T. L. T., DELWICHE, M. E., COLWELL, F. S., MCLING, T. L., PETZKE, L. M. & SMITH, R. W. 2008. Stimulation Of Microbial Urea Hydrolysis In Groundwater To Enhance Calcite Precipitation. *Environmental Science & Technology*, 42, 3025-3032.
- GLASAUER, S., LANGLEY, S. & BEVERIDGE, T. J. 2001. Sorption of Fe (hydr)oxides to the surface of *Shewanella putrefaciens*: cell-bound fine-grained minerals are not always formed de novo. *Applied and environmental microbiology*, 67, 5544-50.
- GLASAUER, S., LANGLEY, S. & BEVERIDGE, T. J. 2002. Intracellular Iron Minerals in a Dissimilatory Iron-Reducing Bacterium. *Science*, 295, 117-119.
- GODINEZ, I. G., DARNAULT, C. J. G., KHODADOUST, A. P. & BOGDAN, D. 2013. Deposition and release kinetics of nano-TiO₂ in saturated porous media: Effects of solution ionic strength and surfactants. *Environmental Pollution*, 174, 106-113.
- GOGOS, A., KNAUER, K. & BUCHELI, T. D. 2012. Nanomaterials in plant protection and fertilization: current state, foreseen applications, and research priorities. *Journal of agricultural and food chemistry*, 60, 9781-9792.
- GOLMOHAMADI, M., CLARK, R. J., VEINOT, J. G. & WILKINSON, K. J. 2013. The role of charge on the diffusion of solutes and nanoparticles (silicon nanocrystals, nTiO₂, nAu) in a biofilm. *Environmental Chemistry*, 10, 34-41.
- GOPAL, M., KUMAR, R. & GOSWAMI, A. 2012. Nano-pesticides-a recent approach for pest control. *The Journal of Plant Protection Sciences*, 4, 1-7.
- GORMAN-LEWIS, D., FEIN, J. B., SODERHOLM, L., JENSEN, M. P. & CHIANG, M. H. 2005. Experimental study of neptunyl adsorption onto *Bacillus subtilis*. *Geochimica et Cosmochimica Acta*, 69, 4837-4844.
- GRAY, M. J., MALATI, M. A. & ROPHAEL, M. W. 1978. The point of zero charge of manganese dioxides. *Journal of Electroanalytical Chemistry and Interfacial Electrochemistry*, 89, 135-140.
- GUCZI, L., BECK, A. & PÁSZTI, Z. 2012. Gold catalysis: Effect of particle size on reactivity towards various substrates. *Catalysis Today*, 181, 26-32.

- HAMMES, F., SEKA, A., VAN HEGE, K., VAN DE WIELE, T., VANDERDEELEN, J., SICILIANO, S. D. & VERSTRAETE, W. 2003. Calcium removal from industrial wastewater by bio-catalytic CaCO₃ precipitation. *Journal of Chemical Technology & Biotechnology*, 78, 670-677.
- HANDY, R., VON DER KAMMER, F., LEAD, J., HASSELLÖV, M., OWEN, R. & CRANE, M. 2008a. The ecotoxicology and chemistry of manufactured nanoparticles. *Ecotoxicology*, 17, 287-314.
- HANDY, R. D., OWEN, R. & VALSAMI-JONES, E. 2008b. The ecotoxicology of nanoparticles and nanomaterials: current status, knowledge gaps, challenges, and future needs. *Ecotoxicology (London, England)*, 17, 315-325.
- HARDING, I. S., RASHID, N. & HING, K. A. 2005. Surface charge and the effect of excess calcium ions on the hydroxyapatite surface. *Biomaterials*, 26, 6818-6826.
- HAZEN, R. M. & SVERJENSKY, D. A. 2010. Mineral surfaces, geochemical complexities, and the origins of life. *Cold Spring Harbor perspectives in biology*, 2, a002162.
- HE, F. & ZHAO, D. 2005. Preparation and Characterization of a New Class of Starch-Stabilized Bimetallic Nanoparticles for Degradation of Chlorinated Hydrocarbons in Water. *Environmental Science & Technology*, 39, 3314-3320.
- HOHELLA JR, M. F. 2002. Nanoscience and technology: the next revolution in the Earth sciences. *Earth and Planetary Science Letters*, 203, 593-605.
- HOHELLA, M. F., LOWER, S. K., MAURICE, P. A., PENN, R. L., SAHAI, N., SPARKS, D. L. & TWINING, B. S. 2008. Nanominerals, Mineral Nanoparticles, and Earth Systems. *Science*, 319, 1631-1635.
- HONG, Y., HONDA, R. J., MYUNG, N. V. & WALKER, S. L. 2009. Transport of iron-based nanoparticles: role of magnetic properties. *Environmental Science & Technology*, 43, 8834-8839.
- HORWELL, C. J. & BAXTER, P. J. 2006. The respiratory health hazards of volcanic ash: a review for volcanic risk mitigation. *Bulletin of Volcanology*, 69, 1-24.
- HU, J.-D., ZEVI, Y., KOU, X.-M., XIAO, J., WANG, X.-J. & JIN, Y. 2010. Effect of dissolved organic matter on the stability of magnetite nanoparticles under different pH and ionic strength conditions. *Science of The Total Environment*, 408, 3477-3489.
- IJIMA, M. & KAMIYA, H. 2009. Surface modification for improving the stability of nanoparticles in liquid media. *Kona Powder Particle J*, 27, 119-129.
- ILLÉS, E. & TOMBÁ CZ, E. 2003. The role of variable surface charge and surface complexation in the adsorption of humic acid on magnetite. *Colloids and Surfaces A: Physicochemical and Engineering Aspects*, 230, 99-109.
- INSTRUMENTS, M. 2011. Zeta potential: An Introduction in 30 minutes. *Zetasizer Nano Serles Technical Note. MRK654-01*.
- JAFFER, Y., CLARK, T. A., PEARCE, P. & PARSONS, S. A. 2002. Potential phosphorus recovery by struvite formation. *Water Research*, 36, 1834-1842.
- JIANG, W., MASHAYEKHI, H. & XING, B. 2009. Bacterial toxicity comparison between nano-and micro-scaled oxide particles. *Environmental Pollution*, 157, 1619-1625.
- JOHNS, M. 1995. Developments in wastewater treatment in the meat processing industry: A review. *Bioresource Technology*, 54, 203-216.

- JU-NAM, Y. & LEAD, J. R. 2008. Manufactured nanoparticles: An overview of their chemistry, interactions and potential environmental implications. *Science of The Total Environment*, 400, 396-414.
- KANEL, S., NEPAL, D., MANNING, B. & CHOI, H. 2007. Transport of surface-modified iron nanoparticle in porous media and application to arsenic(III) remediation. *Journal of Nanoparticle Research*, 9, 725-735.
- KARN, B., KUIKEN, T. & OTTO, M. 2011. Nanotechnology and in situ remediation: a review of the benefits and potential risks. *Ciencia & Saude Coletiva*, 16, 165-178.
- KELLEY, D. S., KARSON, J. A., BLACKMAN, D. K., FRUÈH-GREEN, G. L., BUTTERFIELD, D. A., LILLEY, M. D., OLSON, E. J., SCHRENK, M. O., ROE, K. K. & LEBON, G. T. 2001. An off-axis hydrothermal vent field near the Mid-Atlantic Ridge at 30 N. *Nature*, 412, 145-149.
- KIM, J., PARK, Y., YOON, T. H., YOON, C. S. & CHOI, K. 2010a. Phototoxicity of CdSe/ZnSe quantum dots with surface coatings of 3-mercaptopropionic acid or tri-*n*-octylphosphine oxide/gum arabic in *Daphnia magna* under environmentally relevant UV-B light. *Aquatic toxicology*, 97, 116-124.
- KIM, Y.-Y., RIBEIRO, L., MAILLOT, F., WARD, O., EICHHORN, S. J. & MELDRUM, F. C. 2010b. Bio-Inspired Synthesis and Mechanical Properties of Calcite-Polymer Particle Composites. *Advanced Materials*, 22, 2082-2086.
- KISER, M. A., RYU, H., JANG, H., HRISTOVSKI, K. & WESTERHOFF, P. 2010. Biosorption of nanoparticles to heterotrophic wastewater biomass. *Water Research*, 44, 4105-4114.
- KISER, M. A., WESTERHOFF, P., BENN, T., WANG, Y., PÉREZ-RIVERA, J. & HRISTOVSKI, K. 2009. Titanium Nanomaterial Removal and Release from Wastewater Treatment Plants. *Environmental Science & Technology*, 43, 6757-6763.
- KONHAUSER, K. O. 2009. *Introduction to geomicrobiology*, John Wiley & Sons.
- KUMAR, P., ROBINS, A., VARDOLAKIS, S. & BRITTER, R. 2010. A review of the characteristics of nanoparticles in the urban atmosphere and the prospects for developing regulatory controls. *Atmospheric Environment*, 44, 5035-5052.
- KURAHATTI, R., SURENDRANATHAN, A., KORI, S., SINGH, N., KUMAR, A. R. & SRIVASTAVA, S. 2010. Defence applications of polymer nanocomposites. *Defence Science Journal*, 60, 551-563.
- KVITEK, L., PANACEK, A., SOUKUPOVA, J., KOLAR, M., VECEROVA, R., PRUCEK, R., HOLECOVA, M. & ZBORIL, R. 2008. Effect of Surfactants and Polymers on Stability and Antibacterial Activity of Silver Nanoparticles (NPs). *The Journal of Physical Chemistry C*, 112, 5825-5834.
- LASAGA, A. *Kinetic theory in the Earth Sciences*, 1998. Princeton University Press.
- LASAGNA-REEVES, C., GONZALEZ-ROMERO, D., BARRIA, M. A., OLMEDO, I., CLOS, A., SADAGOPA RAMANUJAM, V. M., URAYAMA, A., VERGARA, L., KOGAN, M. J. & SOTO, C. 2010. Bioaccumulation and toxicity of gold nanoparticles after repeated administration in mice. *Biochemical and Biophysical Research Communications*, 393, 649-655.
- LAZAROVA, V. & MANEM, J. 1995. Biofilm characterization and activity analysis in water and wastewater treatment. *Water Research*, 29, 2227-2245.
- LECOANET, H. F., BOTTERO, J.-Y. & WIESNER, M. R. 2004. Laboratory Assessment of the Mobility of Nanomaterials in Porous Media. *Environmental Science & Technology*, 38, 5164-5169.

- LECOANET, H. F. & WIESNER, M. R. 2004. Velocity Effects on Fullerene and Oxide Nanoparticle Deposition in Porous Media. *Environmental Science & Technology*, 38, 4377-4382.
- LEE, W. M., AN, Y. J., YOON, H. & KWEON, H. S. 2008. Toxicity and bioavailability of copper nanoparticles to the terrestrial plants mung bean (*Phaseolus radiatus*) and wheat (*Triticum aestivum*): Plant agar test for water-insoluble nanoparticles. *Environmental Toxicology and Chemistry*, 27, 1915-1921.
- LEON MORALES, C. F., STRATHMANN, M. & FLEMMING, H.-C. 2007. Influence of biofilms on the movement of colloids in porous media. Implications for colloid facilitated transport in subsurface environments. *Water Research*, 41, 2059-2068.
- LESLEY A. WARREN, PATRICIA A. MAURICE, NAGINA PARMAR & FERRIS, F. G. 2001. Microbially Mediated Calcium Carbonate Precipitation: Implications for Interpreting Calcite Precipitation and for Solid-Phase Capture of Inorganic Contaminants. *Geomicrobiology Journal*, 18, 93-115.
- LEVAR, C., HOTZE, E. M., LOWRY, G. V. & BROWN, G. E. 2012. Environmental Transformations of Silver Nanoparticles: Impact on Stability and Toxicity. *Environmental Science & Technology*, 46, 6900-6914.
- LI, X.-Q., ELLIOTT, D. W. & ZHANG, W.-X. 2006. Zero-Valent Iron Nanoparticles for Abatement of Environmental Pollutants: Materials and Engineering Aspects. *Critical Reviews in Solid State and Materials Sciences*, 31, 111-122.
- LI, Z., ALY HASSAN, A., SAHLE-DEMESSIE, E. & SORIAL, G. A. Transport of nanoparticles with dispersant through biofilm coated drinking water sand filters. *Water Research*.
- LI, Z., ALY HASSAN, A., SAHLE-DEMESSIE, E. & SORIAL, G. A. 2013. Transport of nanoparticles with dispersant through biofilm coated drinking water sand filters. *Water Research*, 47, 6457-6466.
- LIMBACH, L. K., BEREITER, R., MULLER, E., KREBS, R., GALLI, R. & STARK, W. J. 2008. Removal of Oxide Nanoparticles in a Model Wastewater Treatment Plant: Influence of Agglomeration and Surfactants on Clearing Efficiency. *Environmental Science & Technology*, 42, 5828-5833.
- LIU, Y. & TAY, J.-H. 2004. State of the art of biogranulation technology for wastewater treatment. *Biotechnology Advances*, 22, 533-563.
- LIU, Y., YANG, S.-F., TAY, J.-H., LIU, Q.-S., QIN, L. & LI, Y. 2004. Cell hydrophobicity is a triggering force of biogranulation. *Enzyme and Microbial Technology*, 34, 371-379.
- LOWRY, G. V., ESPINASSE, B. P., BADIREDDY, A. R., RICHARDSON, C. J., REINSCH, B. C., BRYANT, L. D., BONE, A. J., DEONARINE, A., CHAE, S. & THEREZIEN, M. 2012a. Long-term transformation and fate of manufactured Ag nanoparticles in a simulated large scale freshwater emergent wetland. *Environmental Science & Technology*, 46, 7027-7036.
- LOWRY, G. V., GREGORY, K. B., APTE, S. C. & LEAD, J. R. 2012b. Transformations of Nanomaterials in the Environment. *Environmental Science & Technology*, 46, 6893-6899.
- LU, C. H., QI, L. M., CONG, H. L., WANG, X. Y., YANG, J. H., YANG, L. L., ZHANG, D. Y., MA, J. M. & CAO, W. X. 2005. Synthesis of calcite single crystals with porous surface by templating of polymer latex particles. *Chemistry of Materials*, 17, 5218-5224.
- LUO, X., MORRIN, A., KILLARD, A. J. & SMYTH, M. R. 2006. Application of Nanoparticles in Electrochemical Sensors and Biosensors. *Electroanalysis*, 18, 319-326.

- MAHIAN, O., KIANIFAR, A., KALOGIROU, S. A., POP, I. & WONGWISES, S. 2013. A review of the applications of nanofluids in solar energy. *International Journal of Heat and Mass Transfer*, 57, 582-594.
- MAILLARD, F., SAVINOVA, E. R. & STIMMING, U. 2007. CO monolayer oxidation on Pt nanoparticles: Further insights into the particle size effects. *Journal of Electroanalytical Chemistry*, 599, 221-232.
- MARTIN, D., DODDS, K., NGWENYA, B. T., BUTLER, I. B. & ELPHICK, S. C. 2012. Inhibition of *Sporosarcina pasteurii* under Anoxic Conditions: Implications for Subsurface Carbonate Precipitation and Remediation via Ureolysis. *Environmental Science & Technology*, 46, 8351-8355.
- MARTINEZ, R. E. & FERRIS, F. G. 2005. Review of the surface chemical heterogeneity of bacteriogenic iron oxides: Proton and cadmium sorption. *American Journal of Science*, 305, 854-871.
- MARTINEZ, R. E., PEDERSEN, K. & FERRIS, F. G. 2004. Cadmium complexation by bacteriogenic iron oxides from a subterranean environment. *Journal of Colloid and Interface Science*, 275, 82-89.
- MAYNARD, A. D., WARHEIT, D. B. & PHILBERT, M. A. 2011. The New Toxicology of Sophisticated Materials: Nanotoxicology and Beyond. *Toxicological Sciences*, 120, S109-S129.
- MISRA, S. K., DYBOWSKA, A., BERHANU, D., CROTEAU, M. N., LUOMA, S. N., BOCCACCINI, A. R. & VALSAMI-JONES, E. 2011. Isotopically Modified Nanoparticles for Enhanced Detection in Bioaccumulation Studies. *Environmental Science & Technology*, 46, 1216-1222.
- MITCHELL, A. C., DIDERIKSEN, K., SPANGLER, L. H., CUNNINGHAM, A. B. & GERLACH, R. 2010. Microbially Enhanced Carbon Capture and Storage by Mineral-Trapping and Solubility-Trapping. *Environmental Science & Technology*, 44, 5270-5276.
- MITCHELL, A. C. & FERRIS, F. G. 2005. The coprecipitation of Sr into calcite precipitates induced by bacterial ureolysis in artificial groundwater: Temperature and kinetic dependence. *Geochimica Et Cosmochimica Acta*, 69, 4199-4210.
- MOORE, M. N. 2006. Do nanoparticles present ecotoxicological risks for the health of the aquatic environment? *Environment International*, 32, 967-976.
- MUELLER, N., BRAUN, J., BRUNS, J., ČERNÍK, M., RISSING, P., RICKERBY, D. & NOWACK, B. 2012. Application of nanoscale zero valent iron (NZVI) for groundwater remediation in Europe. *Environmental Science and Pollution Research*, 19, 550-558.
- MUELLER, N. C. & NOWACK, B. 2008. Exposure Modeling of Engineered Nanoparticles in the Environment. *Environmental Science & Technology*, 42, 4447-4453.
- MURPHY, J. & RILEY, J. P. 1958. A Single-Solution Method for the Determination of Soluble Phosphate in Sea Water. *Journal of the Marine Biological Association of the United Kingdom*, 37, 9-14.
- MUSEE, N. 2011. Nanowastes and the environment: Potential new waste management paradigm. *Environment International*, 37, 112-128.
- NEL, A., XIA, T., MÄDLER, L. & LI, N. 2006. Toxic Potential of Materials at the Nanolevel. *Science*, 311, 622-627.
- NELSON, N. O., MIKKELSEN, R. L. & HESTERBERG, D. L. 2003. Struvite precipitation in anaerobic swine lagoon liquid: effect of pH and Mg:P ratio and determination of rate constant. *Bioresource Technology*, 89, 229-236.

- NETWORK, N. K. T. 2010. *Nanotechnology: a UK Industry View* [Online]. Available: http://www.matuk.co.uk/docs/Nano_report.pdf [Accessed 09/08/2011 2011].
- NGWENYA, B. T., SUTHERLAND, I. W. & KENNEDY, L. 2003. Comparison of the acid-base behaviour and metal adsorption characteristics of a gram-negative bacterium with other strains. *Applied Geochemistry*, 18, 527-538.
- NICOLELLA, C., VAN LOOSDRECHT, M. C. M. & HEIJNEN, J. J. 2000. Wastewater treatment with particulate biofilm reactors. *Journal of Biotechnology*, 80, 1-33.
- NOWACK, B. & BUCHELI, T. D. 2007. Occurrence, behavior and effects of nanoparticles in the environment. *Environmental Pollution*, 150, 5-22.
- O'DOWD, C. D., SMITH, M. H., CONSTERDINE, I. E. & LOWE, J. A. 1997. Marine aerosol, sea-salt, and the marine sulphur cycle: a short review. *Atmospheric Environment*, 31, 73-80.
- O'TOOLE, G., KAPLAN, H. B. & KOLTER, R. 2000. Biofilm formation as microbial development. *Annual Reviews in Microbiology*, 54, 49-79.
- OHLINGER, K. N., YOUNG, T. M. & SCHROEDER, E. D. 1998. Predicting struvite formation in digestion. *Water Research*, 32, 3607-3614.
- OSBORNE, C. A., LULICH, J. P., POLZIN, D. J., ALLEN, T. A., KRUGER, J. M., BARTGES, J. W., KOEHLER, L. A., ULRICH, L. K., BIRD, K. A. & SWANSON, L. L. 1999. Medical dissolution and prevention of canine struvite urolithiasis. Twenty years of experience. *The Veterinary clinics of North America. Small animal practice*, 29, 73-111, xi.
- OVERNEY, R. M. 2009. Nanoscience on the tip. *University of Washington*.
- PALMER, J., FLINT, S. & BROOKS, J. 2007. Bacterial cell attachment, the beginning of a biofilm. *Journal of industrial microbiology & biotechnology*, 34, 577-588.
- PALMER JR, R. J. & WHITE, D. C. 1997. Developmental biology of biofilms: implications for treatment and control. *Trends in microbiology*, 5, 435-440.
- PARKHURST, D. L. & APPELO, C. A. J. 1999. User's guide to PHREEQC (Version 2) : a computer program for speciation, batch-reaction, one-dimensional transport, and inverse geochemical calculations. *U.S. Geological Survey Water-Resources Investigations Report*.
- PARKIN, I. P. & PALGRAVE, R. G. 2005. Self-cleaning coatings. *Journal of Materials Chemistry*, 15, 1689-1695.
- PASTOR, L., MANGIN, D., BARAT, R. & SECO, A. 2008. A pilot-scale study of struvite precipitation in a stirred tank reactor: Conditions influencing the process. *Bioresource Technology*, 99, 6285-6291.
- PAUTLER, M. & BRENNER, S. 2010. Nanomedicine: promises and challenges for the future of public health. *International journal of nanomedicine*, 5, 803.
- PEI, Z., LI, L., SUN, L., ZHANG, S., SHAN, X.-Q., YANG, S. & WEN, B. 2013. Adsorption characteristics of 1,2,4-trichlorobenzene, 2,4,6-trichlorophenol, 2-naphthol and naphthalene on graphene and graphene oxide. *Carbon*, 51, 156-163.
- PERALTA-VIDEA, J. R., ZHAO, L., LOPEZ-MORENO, M. L., DE LA ROSA, G., HONG, J. & GARDEA-TORRESDEY, J. L. 2011. Nanomaterials and the environment: A review for the biennium 2008-2010. *Journal of Hazardous Materials*, 186, 1-15.

- PETOSA, A. R., BRENNAN, S. J., RAJPUT, F. & TUFENKJI, N. 2012. Transport of two metal oxide nanoparticles in saturated granular porous media: Role of water chemistry and particle coating. *Water Research*, 46, 1273-1285.
- PETOSA, A. R., JAISI, D. P., QUEVEDO, I. R., ELIMELECH, M. & TUFENKJI, N. 2010. Aggregation and Deposition of Engineered Nanomaterials in Aquatic Environments: Role of Physicochemical Interactions. *Environmental Science & Technology*, 44, 6532-6549.
- PEULEN, T.-O. & WILKINSON, K. J. 2011. Diffusion of nanoparticles in a biofilm. *Environmental Science & Technology*, 45, 3367-3373.
- PHOENIX, V. R., MARTINEZ, R. E., KONHAUSER, K. O. & FERRIS, F. G. 2002. Characterization and Implications of the Cell Surface Reactivity of *Calothrix* sp. Strain KC97. *Appl. Environ. Microbiol.*, 68, 4827-4834.
- PILOTEK, S. & TABELLION, F. 2005. Nanoparticles in coatings. *Eur. Coat. J*, 4, 170-176.
- POWELL, M., GRIFFIN, M. A. & TAI, S. 2008. Bottom-Up Risk Regulation? How Nanotechnology Risk Knowledge Gaps Challenge Federal and State Environmental Agencies. *Environmental Management*, 42, 426-443.
- PRICE, P. B. 2000. A habitat for psychrophiles in deep Antarctic ice. *Proceedings of the National Academy of Sciences*, 97, 1247-1251.
- QUARMBY, J. & FORSTER, C. F. 1995. An examination of the structure of UASB granules. *Water Research*, 29, 2449-2454.
- RAI, M., YADAV, A. & GADE, A. 2009. Silver nanoparticles as a new generation of antimicrobials. *Biotechnology Advances*, 27, 76-83.
- RAO, C. N. R., KULKARNI, G. U., THOMAS, P. J. & EDWARDS, P. P. 2002. Size-Dependent Chemistry: Properties of Nanocrystals. *Chemistry - A European Journal*, 8, 28-35.
- REMPEL, A. W. & WORSTER, M. G. 1999. The interaction between a particle and an advancing solidification front. *Journal of Crystal Growth*, 205, 427-440.
- RIETMEIJER, F. J. & MACKINNON, I. D. 1997. Bismuth oxide nanoparticles in the stratosphere. *Journal of Geophysical Research: Planets (1991-2012)*, 102, 6621-6627.
- RIJNAARTS, H. H., NORDE, W., LYKLEMA, J. & ZEHNDER, A. J. 1999. DLVO and steric contributions to bacterial deposition in media of different ionic strengths. *Colloids and Surfaces B: Biointerfaces*, 14, 179-195.
- RODUNER, E. 2006. Size Matters: Why Nanomaterials Are Different. *ChemInform*, 37, no-no.
- RYU, H.-D., KIM, D. & LEE, S.-I. 2008. Application of struvite precipitation in treating ammonium nitrogen from semiconductor wastewater. *Journal of Hazardous Materials*, 156, 163-169.
- RYU, H.-D. & LEE, S.-I. 2010. Application of struvite precipitation as a pretreatment in treating swine wastewater. *Process Biochemistry*, 45, 563-572.
- SALEH, N., KIM, H.-J., PHENRAT, T., MATYJASZEWSKI, K., TILTON, R. D. & LOWRY, G. V. 2008. Ionic Strength and Composition Affect the Mobility of Surface-Modified Fe₀ Nanoparticles in Water-Saturated Sand Columns. *Environmental Science & Technology*, 42, 3349-3355.
- SCHRICK, B., HYDUTSKY, B. W., BLOUGH, J. L. & MALLOUK, T. E. 2004. Delivery vehicles for zerovalent metal nanoparticles in soil and groundwater. *Chemistry of Materials*, 16, 2187-2193.
- SCHULZ, H. N. & SCHULZ, H. D. 2005. Large Sulfur Bacteria and the Formation of Phosphorite. *Science*, 307, 416-418.

- SHI, L.-N., ZHANG, X. & CHEN, Z.-L. 2011. Removal of Chromium (VI) from wastewater using bentonite-supported nanoscale zero-valent iron. *Water Research*, 45, 886-892.
- SILVER-COLLOIDS. 2012. *The Influence of Zeta Potential* [Online]. Available: <http://www.silver-colloids.com/Tutorials/Intro/pcs18.html> [Accessed 2014].
- SIMONET, B. M. & VALCÁRCEL, M. 2009. Monitoring nanoparticles in the environment. *Analytical and Bioanalytical Chemistry*, 393, 17-21.
- SMALL, T. D., WARREN, L. A. & FERRIS, F. G. 2001. Influence of ionic strength on strontium sorption to bacteria, Fe(III) oxide, and composite bacteria-Fe(III) oxide surfaces. *Applied Geochemistry*, 16, 939-946.
- SMITH, C. J., SHAW, B. J. & HANDY, R. D. 2007. Toxicity of single walled carbon nanotubes to rainbow trout, (*Oncorhynchus mykiss*): Respiratory toxicity, organ pathologies, and other physiological effects. *Aquatic toxicology*, 82, 94-109.
- SPERANZA, A., LEOPOLD, K., MAIER, M., TADDEI, A. R. & SCOCCIANI, V. 2010. Pd-nanoparticles cause increased toxicity to kiwifruit pollen compared to soluble Pd (II). *Environmental Pollution*, 158, 873-882.
- STANKUS, D. P., LOHSE, S. E., HUTCHISON, J. E. & NASON, J. A. 2010. Interactions between natural organic matter and gold nanoparticles stabilized with different organic capping agents. *Environmental Science & Technology*, 45, 3238-3244.
- STANLEY, N. R. & LAZAZZERA, B. A. 2004. Environmental signals and regulatory pathways that influence biofilm formation. *Molecular microbiology*, 52, 917-924.
- STEWART, P. S. 2003. Diffusion in biofilms. *Journal of bacteriology*, 185, 1485-1491.
- STOCKS-FISCHER, S., GALINAT, J. K. & BANG, S. S. 1999. Microbiological precipitation of CaCO₃. *Soil Biology and Biochemistry*, 31, 1563-1571.
- STOODLEY, P. & LEWANDOWSKI, Z. 1994. Liquid flow in biofilm systems. *Applied and environmental microbiology*, 60, 2711-2716.
- STOODLEY, P., SAUER, K., DAVIES, D. & COSTERTON, J. W. 2002. Biofilms as complex differentiated communities. *Annual Reviews in Microbiology*, 56, 187-209.
- SUJITH, P. P. & BHARATHI, P. A. L. 2011. Manganese Oxidation by Bacteria: Biogeochemical Aspects
Molecular Biomineralization. In: MÜLLER, W. E. G. (ed.). Springer Berlin Heidelberg.
- TAY, J.-H., PAN, S., HE, Y. & TAY, S. T. L. 2004. Effect of organic loading rate on aerobic granulation. I: Reactor performance. *Journal of Environmental Engineering*, 130, 1094-1101.
- TENG, H. H., DOVE, P. M. & DE YOREO, J. J. 2000. Kinetics of calcite growth: surface processes and relationships to macroscopic rate laws. *Geochimica et Cosmochimica Acta*, 64, 2255-2266.
- TIRAFERRI, A. & SETHI, R. 2009. Enhanced transport of zerovalent iron nanoparticles in saturated porous media by guar gum. *Journal of Nanoparticle Research*, 11, 635-645.
- TOBLER, D. J., CUTHBERT, M. O., GRESWELL, R. B., RILEY, M. S., RENSHAW, J. C., HANDLEY-SIDHU, S. & PHOENIX, V. R. 2011. Comparison of rates of ureolysis between *Sporosarcina pasteurii* and an indigenous groundwater community under conditions required to precipitate large volumes of calcite. *Geochimica et Cosmochimica Acta*, 75, 3290-3301.

- TOBLER, D. J., MACLACHLAN, E. & PHOENIX, V. R. 2012. Microbially mediated plugging of porous media and the impact of differing injection strategies. *Ecological Engineering*, 42, 270-278.
- TROUILLER, B., RELIENE, R., WESTBROOK, A., SOLAIMANI, P. & SCHIESTL, R. H. 2009. Titanium Dioxide Nanoparticles Induce DNA Damage and Genetic Instability In vivo in Mice. *Cancer Research*.
- TUFENKJI, N. & ELIMELECH, M. 2003. Correlation Equation for Predicting Single-Collector Efficiency in Physicochemical Filtration in Saturated Porous Media. *Environmental Science & Technology*, 38, 529-536.
- ULUDAG-DEMIRER, S., DEMIRER, G. N. & CHEN, S. 2005. Ammonia removal from anaerobically digested dairy manure by struvite precipitation. *Process Biochemistry*, 40, 3667-3674.
- VAN CAPPELLEN, P., CHARLET, L., STUMM, W. & WERSIN, P. 1993. A surface complexation model of the carbonate mineral-aqueous solution interface. *Geochimica et Cosmochimica Acta*, 57, 3505-3518.
- VAN LOOSDRECHT, M. C., NORDE, W., LYKLEMA, J. & ZEHNDER, A. J. 1990. Hydrophobic and electrostatic parameters in bacterial adhesion. *Aquatic sciences*, 52, 103-114.
- VERCHOVSKY, A. B., FISENKO, A. V., SEMJONOVA, L. F., BRIDGES, J., LEE, M. R. & WRIGHT, I. P. 2006. Nanodiamonds from AGB stars: A new type of presolar grain in meteorites. *The Astrophysical Journal*, 651, 481.
- VIDOJKOVIC, S., RODRIGUEZ-SANTIAGO, V., FEDKIN, M. V., WESOLOWSKI, D. J. & LVOV, S. N. 2011. Electrophoretic mobility of magnetite particles in high temperature water. *Journal Name: Chemical Engineering Science; Journal Volume: 66; Journal Issue: 18, Medium: X; Size: 4029*.
- VIJAYARAGHAVAN, K. & YUN, Y.-S. 2008. Bacterial biosorbents and biosorption. *Biotechnology Advances*, 26, 266-291.
- VILLALOBOS, M., ESCOBAR-QUIROZ, I. N. & SALAZAR-CAMACHO, C. 2014. The influence of particle size and structure on the sorption and oxidation behavior of birnessite: I. Adsorption of As(V) and oxidation of As(III). *Geochimica et Cosmochimica Acta*, 125, 564-581.
- W., B. J. & K., N. D. 1992. Geochemical model to calculate speciation of major trace and redox elements in natural waters. *US Geological Survey, International groundwater modeling centre*.
- WANG, J., GERLACH, J. D., SAVAGE, N. & COBB, G. P. 2013. Necessity and approach to integrated nanomaterial legislation and governance. *Science of The Total Environment*, 442, 56-62.
- WARREN, L. A. & FERRIS, F. G. 1998. Continuum between sorption and precipitation of Fe (III) on microbial surfaces. *Environmental Science & Technology*, 32, 2331-2337.
- WARREN, L. A., MAURICE, P. A., PARMAR, N. & FERRIS, F. G. 2001. Microbially mediated calcium carbonate precipitation: implications for interpreting calcite precipitation and for solid-phase capture of inorganic contaminants. *Geomicrobiology Journal*, 18, 93-115.
- WEIR, A., WESTERHOFF, P., FABRICIUS, L., HRISTOVSKI, K. & VON GOETZ, N. 2012. Titanium Dioxide Nanoparticles in Food and Personal Care Products. *Environmental Science & Technology*, 46, 2242-2250.
- WHIFFIN, V. S., VAN PAASSEN, L. A. & HARKES, M. P. 2007. Microbial Carbonate Precipitation as a Soil Improvement Technique. *Geomicrobiology Journal*, 24, 417-423.
- WIESNER, M. R., LOWRY, G. V., ALVAREZ, P., DIONYSIOU, D. & BISWAS, P. 2006. Assessing the Risks of Manufactured Nanomaterials. *Environmental Science & Technology*, 40, 4336-4345.

- WILSON, B., DEWERS, T., RECHES, Z. E. & BRUNE, J. 2005. Particle size and energetics of gouge from earthquake rupture zones. *Nature*, 434, 749-752.
- WONG, M. S., ALVAREZ, P. J. J., FANG, Y.-L., AKÇIN, N., NUTT, M. O., MILLER, J. T. & HECK, K. N. 2009. Cleaner water using bimetallic nanoparticle catalysts. *Journal of Chemical Technology & Biotechnology*, 84, 158-166.
- YANG, C.-M., KALWEI, M., SCHÜTH, F. & CHAO, K.-J. 2003. Gold nanoparticles in SBA-15 showing catalytic activity in CO oxidation. *Applied Catalysis A: General*, 254, 289-296.
- YEE, J. Y. 2007. Ag-Au Core-Shell Nanoparticles.
- YEE, N. & FEIN, J. 2001. Cd adsorption onto bacterial surfaces: A universal adsorption edge? *Geochimica et Cosmochimica Acta*, 65, 2037-2042.
- YEE, N., FOWLE, D. A. & FERRIS, F. G. 2004. A Donnan potential model for metal sorption onto *Bacillus subtilis*. *Geochimica et Cosmochimica Acta*, 68, 3657-3664.
- ZEREINI, F., WISEMAN, C., ALT, F., MESSERSCHMIDT, J., MÜLLER, J. & URBAN, H. 2001. Platinum and rhodium concentrations in airborne particulate matter in Germany from 1988 to 1998. *Environmental Science & Technology*, 35, 1996-2000.
- ZHANG, L., HOU, L., WANG, L., KAN, A. T., CHEN, W. & TOMSON, M. B. 2012. Transport of Fullerene Nanoparticles (nC60) in Saturated Sand and Sandy Soil: Controlling Factors and Modeling. *Environmental Science & Technology*, 46, 7230-7238.
- ZHOU, S. & WU, Y. 2012. Improving the prediction of ammonium nitrogen removal through struvite precipitation. *Environmental Science and Pollution Research*, 19, 347-360.
- ZHU, G., LIN, Z.-H., JING, Q., BAI, P., PAN, C., YANG, Y., ZHOU, Y. & WANG, Z. L. 2013. Toward large-scale energy harvesting by a nanoparticle-enhanced triboelectric nanogenerator. *Nano Letters*, 13, 847-853.
- ZHU, X., CHANG, Y. & CHEN, Y. 2010. Toxicity and bioaccumulation of TiO₂ nanoparticle aggregates in *Daphnia magna*. *Chemosphere*, 78, 209-215.
- ZIAGOVA, M., DIMITRIADIS, G., ASLANIDOU, D., PAPAIOANNOU, X., LITOPOULOU TZANNETAKI, E. & LIAKOPOULOU-KYRIAKIDES, M. 2007. Comparative study of Cd(II) and Cr(VI) biosorption on *Staphylococcus xylosus* and *Pseudomonas* sp. in single and binary mixtures. *Bioresource Technology*, 98, 2859-2865.